Technische Universität München

Wissenschaftszentrum Weihenstephan für Ernährung, Landnutzung und Umwelt

Lehrstuhl für Lebensmittelverpackungstechnik

On line control of transparent inorganic layers deposited on polymeric substrate by phase modulated spectroscopic ellipsometry

Lucie Vašková geb. Bermannová

Vollständiger Ausdruck der von der Fakultät Wissenschaftszentrum Weihenstephan für Ernährung, Landnutzung und Umwelt der Technischen Universität München zur Erlangung des akademischen Grades eines

Doktor-Ingenieurs

genehmigten Dissertation.

Vorsitzender: Univ.-Prof. Dr.-Ing. Roland Meyer-Pittroff

Prüfer der Dissertation:
1. Univ.-Prof. Dr. rer. nat. Horst-Christian Langowski
2. Univ.-Prof. Dr. rer. nat., Dr. rer. nat. habil. Josef Friedrich
3. Univ.-Prof. Dr.-Ing. Jens-Peter Majschak, Technische Universität Dresden

Die Dissertation wurde am 02. 02. 2006 bei der Technischen Universität München eingereicht und durch die Fakultät Wissenschaftszentrum Weihenstephan für Ernährung, Landnutzung und Umwelt am 28. 03. 2006 angenommen.

Acknowledgment

The path to completing my thesis was accompanied by number of wonderful people to whom I would like to thank.

First of all I wish to express my gratitude to my thesis advisor Professor Horst-Christian Langowski for his constant support; without his help, this work would not be possible.

I specially thank Prof. Josef Friedrich and Prof. Jens-Peter Majschak for the time they devoted in reading and commenting on my thesis as part of my thesis committee.

I would like also thank Prof. Stergios Logothetidis and Dr. Maria Gioti from Aristotle University in Thessaloniki for their invaluable advice on spectroscopic ellipsometry and optical properties of the polymeric substrates.

Special thanks also go to Dr. Ramdane Benferhat, Dr. Razvigor Ossikovski and Mr. Frederic Lelan for their support, especially in use of the spectroscopic ellipsometer, which was designed in their company Jobin Yvon S.A.

I would also like to express my sincere thanks to Mr. Gerhard Steiniger, Mr. Jürgen Schröder from Applied Films GmbH & Co. KG and Mr. Wolfgang Lohwasser from Alcan Packaging Services AG for their advice and help in field of the vacuum deposition.

I am grateful to the members of the institute for their help and their comradeship; especially to Klaus Noller, Esra Kucukpinar, Kajetan Müller, Cornelia Stram, Karol Vaško, Marion Schmidt, Zuzana Scheuerer and Brigitte Seifert. I would like also to express thank Mr. Wolfgang Busch for his enthusiastic work and for his help during the lab e-beam coater modification for installation of the ellipsometer.

Finally, I would like to express my deepest gratitude for the moral support and love that I received from my husband Karol, my friends, my parents and my parents in law during the past years.

List of symbols

c	balanced concentration of sorbed small molecules in the polymer
S	solubility coefficient
p	pressure of the surroundings
S_0	pre-exponential factor of the solubility
T_g	glass transition temperature
ΔH_s	molar heat of solution
ΔH_{cond}	molar heat of condensation
ΔH_{mix}	molar heat of mixing
F_x	flux – amount of substance diffusing per unit area per unit time
D	diffusion coefficient
D_0	pre-exponential factor of the diffusion
R	gas constant ($R = 8{,}314\ J.K^{-1}.mol^{-1}$)
E_D	formal activating energy
P	permeation coefficient
Q	molecular permeability
E_k	average kinetic energy
m	mass of the evaporated particles
k	Boltzman constant ($k = 1{,}38{,}10^{-23}\ J.K^{-1}$)
T_v	temperature of the evaporating source in K
v^2	square averaged speed of the evaporated particles
E_x, E_y	electric field vector of linear polarised light in x or y
ω	angular frequency of the light
ν	phase velocity of the light
a_x, a_y	amplitudes of a linear polarised light E_x and E_y
$(\tau+\delta_x)$	the phases of a linear polarised light E_x
$(\tau+\delta_y)$	the phases of a linear polarised light E_y
δ	the phase difference
χ	shift of the ellipse of the elliptical polarised light from the x-axis
e	ratio of the length of the minor half axis of the ellipse b to the length of its major half axis a
$\tilde{r}_p, \tilde{r}_S$	Fresnel complex reflection coefficients
$\tilde{\varphi}_1, \tilde{\varphi}_2$	complex refraction angles of the light reflecting from the interfaces of the absorbing media 1and 2

$\tilde{n}_1, \tilde{n}_2$	complex refractive indexes of the absorbing media 1and 2
$\tilde{\rho}$	complex reflection ratio
$\tilde{\varepsilon}$	complex dielectric function
ε_1	real part of dielectric function
ε_2	imaginary part of dielectric function
n	real part of the complex refractive index
k	imaginary part of the complex refractive index – extinction index
ψ	amplitude ratio
Δ	relative phase change
$\tilde{\varepsilon}_0$	complex dielectric function of the ambient medium – vacuum
I	modulated signal measured by ellipsometer
A_0	modulation amplitude which is proportional to (V_m/λ)
V_m	excitation voltage applied to modulator
λ	wavelength of the light
ω'	modulation frequency
E_g	band gap of the material
Θ	Heaviside Theta function
$\varepsilon(\infty)$	dielectric function at infinite energy
A_i	amplitude factor
Γ_i	broadening factor
E_i	center energy of the oscillator
E_0	resonance frequency
A	transition strength
C	damping constant
$\bar{x}$	arithmetic mean
$\tilde{x}$	median
$\hat{x}$	mode
$s_{\bar{x}}$	square root of standard variance
W	Shapiro-Wilk parameter
U	Mann-Whitney parameter
r_p	Pearson correlation coefficient
r_s	Spearman rank correlation coefficient

List of abbreviations

OTR	oxygen transmission rate
WVTR	water vapour transmission rate
PET	polyethylene therephthalate
PP	polypropylene
BOPP	biaxially oriented polypropylene
oPP	oriented polypropylene
PE	polyethylene
LD-PE	low density polyethylene
HD-PE	high density polyethylene
PEN	polyethylene naphthalate
PVDC	Polyvinylidene Chloride
PA	polyamide
oPA	oriented polyamide
PS	polystyrene
PC	polycarbonate
SiO_x	silicon oxide
SiO	silicon monoxide
SiO_2	silicon dioxide
AlO_x	Aluminium oxide
PVD	Physical vapour deposition
SE	spectroscopic ellipsometry
TL	Tauc-Lorentz model

Contents

1. Introduction and problem definition ... 7
2. Basic principles ... 9
2.1 Permeation and barrier properties of packaging films ... 9
2.1.1 Sorption ... 10
2.1.2 Diffusion ... 11
2.1.3 Permeation in polymeric film ... 12
2.1.4 Permeation through inorganic barrier layers ... 13
2.1.5 Properties of packaging films ... 15
2.2. Physical vapour deposition in vacuum ... 17
2.2.1 Evaporation and layer growth ... 18
2.2.2 E-beam evaporation ... 20
2.2.3 Types of electron-beam evaporators ... 21
2.3 Inorganic transparent barrier coating on the polymers ... 22
2.3.1 Silicon oxide layers ... 22
2.3.2 Aluminium oxide layers ... 26
2.4 Properties of Polyethylene Terephtalate ... 29
2.4.1 Functional properties of Polyethylene Terephtalate ... 29
2.4.2 Optical properties of Polyethylene Terephtalate substrate ... 30
2.5 Basic principles of Ellipsometry ... 33
2.5.1. Interface non-absorbing medium – absorbing medium ... 37
2.5.2. Three-phase (vacuum (air) – thin film – substrate) system ... 38
2.5.3 Spectroscopic phase modulated ellipsometry ... 39
2.5.4 Tauc-Lorentz model ... 41
2.6 Statistical evaluation of the results ... 43
2.6.1 Descriptive statistics ... 43
2.6.2 Inferential statistics ... 45

3. Experimental and evaluation of experimental data ... 49
3.1 Design and speciality of the lab e-beam coater at Fraunhofer IVV ... 49
3.2 In-situ FUV spectroscopic phase modulated ellipsometer ... 52
3.2.1 Modiffication of the lab e-beam coater

for installation of the ellipsometer 52
3.2.2 Installation of the ellipsometer into the lab e-beam coater
and spectra stability measurements 56
3.2.3 Description of in-situ FUV spectroscopic phase-modulated
Ellipsometer.. 58
3.3 Sample preparation.. 62
3.3.1 Preparation of silicon oxide samples 62
3.3.2 Preparation of aluminium oxide samples 63
3.3.3 Deposition parameters 63
3.4 Polyethylene terephtalate films 66
3.5 Analysis of the properties and surfaces of the deposited layers 69
3.5.1 Scanning electron microscopy.. 69
3.5.2 X-ray photoelectron spectroscopy 73
3.5.3 Permeation measurements... 74

4. Results.. 77
4.1 Basic and functional properties of deposited layers 77
4.1.1 Chemical composition... 77
4.1.2 Layer thickness... 80
4.1.3 Barrier properties.. 81
4.1.4 Surface analysis 83
4.1.5 Relation between barrier properties, layer thickness
and the elementary ratio x 86
4.2 Optical properties in comparison to chemical composition
of the produced samples 89
4.2.1 Chemical composition of the layers and layer quality 94
4.3 On-line monitoring of the layer thickness 101
4.3.1 Statistical evaluation of the results:
layer thickness measured by SEM and SE.. 106

5 Conclusions 113
6 Summary 115
7 Literature 118

1 Introduction and problem definition

The task of packaging is to protect the packaged goods against the impact of the surrounding environment and to prevent the loss of the constituents from the packaged food. In the first case the penetration of oxygen and water vapour causes mostly impact, because of their important effect on the quality reduction of the packed food. Oxygen that is present in concentration of 21 % in natural atmosphere, affects the foodstuff in many ways: oxygen changes the colour and taste of the food product, lowers its nutritional value and enables the growth of spoilage micro-organisms in the foodstuff. Water vapour access assists the growth of spoilage microorganisms; on the other hand water losses through the packaging cause lower volume and weight as well as taste changes of packed beverages.

The conventional packaging materials that protect the products from these influences are paper, metal and glass, which have been used in the packaging industry over centuries. Metal and glass have excellent barrier properties; however they are heavy and expensive. At present polymeric materials are mostly used in the packaging industry. Polymeric materials are flexible, lighter, and for the production of the packaging less material can be used. Polymer materials are often also transparent and cost-effective. The common disadvantage of polymeric materials is their lower barrier properties against gases and vapours. Therefore they are often improved in their barrier properties by using inorganic barrier layers. Coatings of polymeric substrates with inorganic materials improve the barrier against gases and vapours such as oxygen, moisture or different organic compounds and thus protect the goods against the environmental impact. The most frequently used material for creating coatings is aluminium (Al), which makes opaque films. Less frequently, but in rising market shares, transparent silicon oxide and aluminium oxide are to be found.

The history of the coating technology already began in the 19th century. In 1852 W. R. Grove sputtered from the tip of a wire held close to a highly polished silver surface at pressure of about 0,5 Torr (67 Pa). He made no studies on the properties of the deposited films since he was more interested in effects of voltage reversal in the discharge. In 1854 M. Faraday also reported film deposition by sputtering in a glow

discharge tube. Thus sputter deposition was the first vacuum coating technology to be available, but not widely used until the upcoming semiconductor device fabrication. Applications of sputter deposition increased rapidly after the invention of the various high-rate magnetron-sputtering sources in the early 1970s. Thermal evaporation was an obvious vapour source long before it was studied. Its development was inhibited by high radiant heat loads and the lack of vacuum materials and techniques that could withstand the heat. Thermal evaporation began to be developed after the work of John Strong on the aluminisation of astronomical mirrors in the mid-1930s and the technology advanced further with the development of e-beam evaporation. This allowed refractory materials like silicon oxide and aluminium oxide to be deposited. At present the technique of e-beam evaporation is widely used in manufacturing of the transparent barrier films for packaging. [1]

The process of barrier coating using transparent inorganic layers such as silicon oxide or aluminium oxide must be monitored or better controlled during the coating process, in order to guarantee the functionality of the layers. Testing of samples from the on going production process can be done either in form of off-line random sampling or in form of on-line light transmission measurement. However, full on-line monitoring or control of transparent silicon oxide or aluminum oxide coatings on polymeric substrates is not available at present.

The aim of the work presented here was therefore the development and testing of novel equipment for full on-line monitoring of transparent barrier layers during the deposition on polymeric films. Research work was concentrated on the adaptation of the measurement equipment to a laboratory scale vacuum web coating machine and on testing of the accuracy and reliability of the measurements using this novel control equipment during deposition at lab e-beam coater.

2 Basic principles

2.1 Permeation and barrier properties of packaging films

Packaging materials serve various requirement of functionality, including also the protection of the product over the required storage life time. Especially an effective barrier against the permeation of gases and vapours is required.

In the fig. 1 the permeation of small molecules through the packaging material is shown. The permeation is the penetration of molecules from a medium with higher concentration towards a medium with lower concentration of the penetrating molecules. The process of the molecular transport can be divided into the following four physical steps [2]:

- Adsorption of small molecules on the surface of the packaging material
- Solution in the packaging material
- Diffusion through the packaging material against the direction of the concentration gradient
- Desorption on the other side of the packaging material

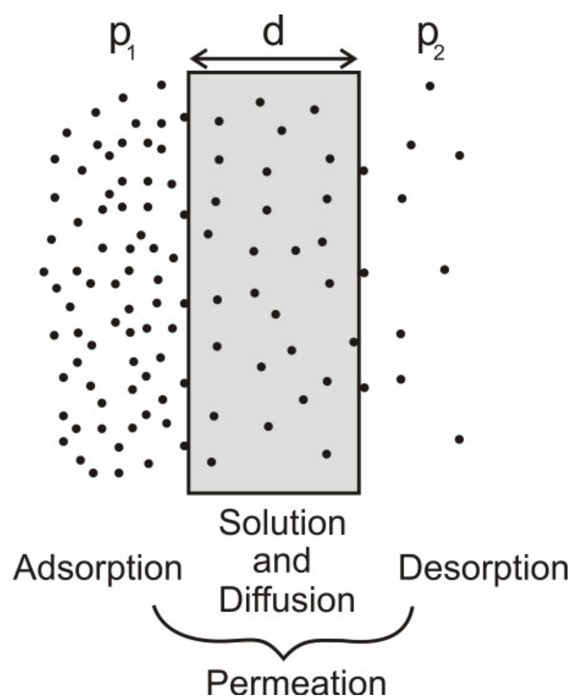

Fig. 1: Scheme of the permeation through the polymer [2]

Practically the direction of the permeation from the surroundings into the environment protected by packaging material is considered [2, 3].

2.1.1 Sorption

The sorption comprises the two physical processes: the adsorption of the small molecule on the material surface and its solution into the packaging material. The simplest case of the solution is the ideal solution behaviour, where sorbed penetrant is randomly dispersed within the polymer such that Henry's law is obeyed:

$$c = Sp \tag{1}$$

where c is the balanced concentration of sorbed small molecules in the polymer, S – solubility coefficient and p is the pressure in the surroundings. This behaviour can be assumed when the permeated molecules do not interact with the polymer and the temperature of the polymer is higher than T_g (glass transition temperature) of that polymer. Those conditions are fulfilled in most cases of gas/polymer [2; 4].

The solubility dependence on the temperature can be represented by an Arrhenius – type relation, but in relatively small ranges of temperature (T), only [5]:

$$S = S_0 e^{\frac{-\Delta H_s}{RT}} \tag{2}$$

Where S_0 is the pre-exponential factor, ΔH_s is the molar heat of solution and can be expressed as sum of the molar heat of condensation, $\Delta H_{cond.}$ And partial molar heat of mixing, ΔH_{mix}:

$$\Delta H_s = \Delta H_{cond} + \Delta H_{mix} \tag{3}$$

In the case of a gas/polymer system, the heat of condensation is very small above T_g, hence the solution heat is defined by the heat of mixing. It means that the

solubility does not change significantly with temperature, because also ΔH_{mix} is very small for the most of the gases. For the vapours (e.g. SO_2, NH_3), which condense on the polymer surface the heat of solution is negative, because of the high ΔH_{cond}. It means that solubility decrease with increasing temperature [6].

2.1.2 Diffusion

The diffusion can be described as the transport of the small molecules through the polymer matrix. Diffusion through a polymer occurs by small molecules passing through voids and other gaps between the polymer molecules. The diffusion will therefore depend to a large extent on the size of the small molecules and the size of gaps. The size of the gaps in the polymer will depend to a large extent on the physical state of polymer. The diffusion is controlled by Fick's laws. First Fick's law is the fundamental law of diffusion. It states that the flux in the x-direction (F_x) is proportional to the concentration gradient ($\partial c/\partial x$) [7, 8, 9]:

$$F_x = -D(\partial c/\partial x) \qquad (4)$$

Flux is the amount of substance diffusing per unit area per unit time and D is the diffusion coefficient. The first law can only be directly applied to diffusion in the steady state, it means that the concentration does not depend on time.

Fick's second law of diffusion describes the non steady state – the concentration gradient is changing with time [2]:

$$\frac{\partial F_x}{\partial x} = -D \cdot \left(\frac{\partial^2 c}{\partial x^2} \right) \qquad (5)$$

When diffusion occurs in a system in which the penetrant interact with the polymer, the total flow is not only due to pure diffusion fluxes but is complicated by a concurrent mass flow of the components [6]

The temperature dependence of the diffusion coefficient follows the Arhenius formula:

$$D = D_0 \cdot e^{-\frac{E_D}{R \cdot T}} \quad (6)$$

where D_0 is the pre-exponential factor, T the temperature, R the gas constant (R = 8,314 $J.K^{-1}.mol^{-1}$) and E_D is the formal activation energy. The formal activation energy is the energy, which is needed for the creating of the gaps in the polymer and for the shift of the molecule from one free gap to another one. The activating energy is always positive, so the diffusion coefficient increases always with increasing temperature [5, 11].

2.1.3 Permeation in polymeric film

The permeation mechanism of gases, water vapour and flavours through polymers depends on two aspects: how many molecules can dissolve in the polymer, e.g. the solubility coefficient S of the permeating substance and how fast molecules can move inside the polymer, i.e. the diffusion coefficient D. The permeation P is given by [3, 10, 11, 12, 14].

$$P = DS \quad (7)$$

Experimentally, the permeability (Q) is determined:

$$Q = \frac{P}{d} \quad (8)$$

where d is the measured film thickness [10, 12]. Usually in practice the permeation (oxygen transmission rate – OTR) of gases is given in [$cm^3/(m^2$ day bar)] and the permeation of condensing substances such as water vapour (water vapour transmission rate – WVTR) in [$g/(m^2$ day)] with respect to humidity gradient. The relations of practically used units to the SI units are given in the table 1:

Table 1: Units for the permeation, diffusion and solubility coefficient.

	Permeation coefficient (P)	**Diffusion-coeffizient, D**	**Solubility coefficient S**
SI units	$\frac{mol \cdot m}{m^2 \cdot s \cdot Pa}$	$\frac{cm^2}{s}$	$\frac{mol}{cm^3 \cdot Pa}$
Gases (O_2)	$\frac{cm^3(STP) \cdot 100\mu m}{cm^2 \cdot s \cdot bar}$	$\frac{cm^2}{s}$	$\frac{cm^3(STP)}{cm^3 \cdot Pa}$
Vapours (H_2O)	$\frac{g \cdot cm}{cm^2 \cdot s \cdot bar}$	$\frac{cm^2}{s}$	$\frac{g}{cm^3 \cdot Pa}$

STP (Standard Temperature and Pressure) - 273,15 K, 101325 Pa

In practice the measured OTR and WVTR are related to the measurement conditions, (which can be different from the STP): temperature, pressure and relative humidity (humidity gradient).

2.1.4 Permeation through inorganic barrier layers

The permeation through vacuum coated inorganic barrier layers, like aluminium oxide AlO_x or silicon oxide, SiO_x, predominantly occurs via the macroscopic defects of the inorganic layers (see figure 2c). [11, 12, 13, 14, 15] The defects in the inorganic layer are created by inhomogeneities in the evaporation process and by particles or contaminations existing on the polymer surface, like dust and antiblock particles. The anti-block particles are the particles, which are incorporated into the polymer surface to avoid the sticking of the polymer film during winding in the machine. It is possible to reduce the amount of defects on the inorganic layer by reducing the amount of antiblock particles (special polymer films for vacuum deposition) and by cleaning the surface from the dust particles before deposition of the inorganic layer. But it is practically impossible to produce an inorganic layer on a polymer film without any defects [12].

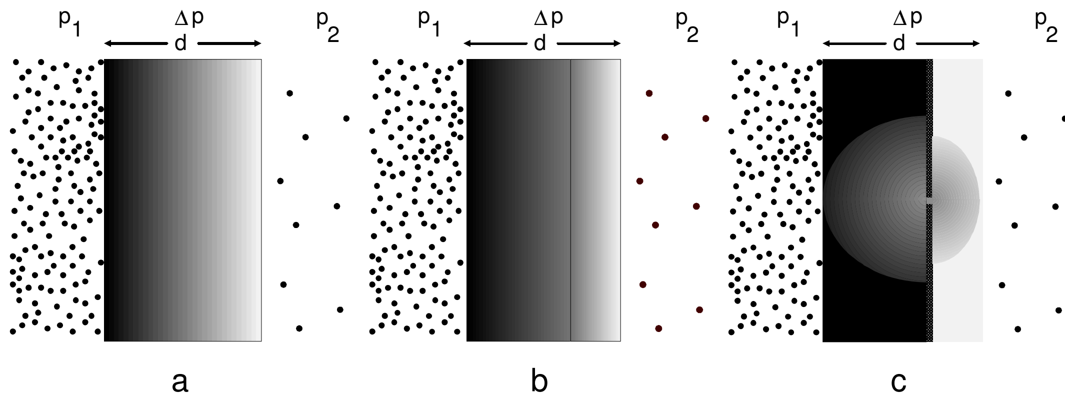

Fig. 2: Permeation mechanism (schematic) through a homogeneous polymer (a), laminate containing two homogeneous polymers (b), and through a three layer laminate containing an inorganic barrier layer (shaded: concentration gradient of permeating subsance) [12]

The barrier properties of the inorganic transparent layers change as a function of its thickness. When the layer thickness is too small, such that it does not cover completely the substrate surface the gases or vapours can permeate through the packaging material and its barrier properties become poor. The optimal range of layer thickness is between the layer thickness, when the layer is closed and covers completely the substrate surface and the thickness when the layer is already too thick and becomes to be brittle (see also chapters 2.4.1 and 2.4.2). [11, 13 – 19].

The second parameter, which strongly influences the barrier properties of the inorganic layers, is their chemical composition together with the layer structure. Especially the amount of oxygen in the layer can be critical for barrier properties of silicon oxide layers, because the higher amount of oxygen can cause some free gaps in the layer structure so that the created layer is not dense enough to terminate the gas and vapour permeation [16, 17, 18]. (*See chapter 2.2.1)*

In the case of polymer films without inorganic coating, the permeability for the substances is proportional to inverse of the polymer thickness. If an inorganic coating is deposited on the polymer surface, the situation changes because of defect-controlled permeation mechanism. If the polymer thickness reaches a certain value,

further increasing of the thickness does not influence the transmittance of the permeating substances through the polymer/inorganic layer system. This thickness is called critical substrate thickness. The critical thickness depends on the diameter of the defect, but in most cases does not exceed 1 µm. [3, 20, 21]

2.1.5 Properties of packaging films

The packaging films used in the food packaging industry protect the packed goods against oxygen and water vapour from the surrounding atmosphere into the package, which would cause the decreasing of the food quality and finally the damage of the food product. The barrier packaging films prolongs significantly the shelf life of the packaged foodstuff. Some of the requirements of the packaging for the different foodstuffs are given in the table 2.

Table 2: Some of the foodstuff requirements from the packaging material [22]

Foodstuff	Shelf life of packaged product [months]	Packaging surface/filling quantity [$dm^2.kg^{-1}$]	Max. acceptable O_2 absorption [ppm]	Max. water volume variation in package [%]	Barrier values for O_2 [$cm^3/(m^2$ day.bar]	Barrier values for H_2O [g/(m^2 day]
Beer	9	6	1 – 4	-2	0,2 – 0,8	- 2,4
Sterile milk	4	6	1 – 5	-2	0,4 – 2	- 5,6
Snacks	2 – 6	20	5 – 15	3	1,2 – 3 (2 months) 0,4 – 1,0 (6 months)	1,6 – 5
Baby food	6 – 12	12	1 – 5	1 – 2	0,12 – 0,6 (6 months) 0,06 – 0,3 (12 months)	1,0 – 2,0 (6 months) 0,4 – 0,8 (12 months)
Instant coffee	6 – 18	18	5 – 15	3	0,4 – 1,2 (6 months) 0,14 – 0,4 (18 months)	0,2 – 2,0

In the food packaging industry polymeric films such as polyethylene therephthalate (PET), polypropylene (PP), polyethylene (PE), polyethylene naphthalate (PEN), Polyvinylidene Chloride (PVDC), polyamide (PA) and polystyrene (PS) films are commonly used. These films have different permeation characteristics for oxygen and water vapour. It can be said that unpolar polyolefins have excellent barrier against water vapour in contrast, the polyethylene therephtalate, which shows higher polarity in comparison to polyolefins has very good barrier properties against oxygen, while its water vapour permeation is higher in comparison to polyolefins (see fig. 4) [21, 22, 23].

For additional improvement of the barrier properties the polymeric films are coated with inorganic layers, either with aluminium (Al) or in the case of further requirements for transparency, with aluminium oxide (AlO_x) or silicon oxide (SiO_x) transparent layers. The typical improvement of the barrier properties against oxygen as well as water vapour is demonstrated in fig. 5.

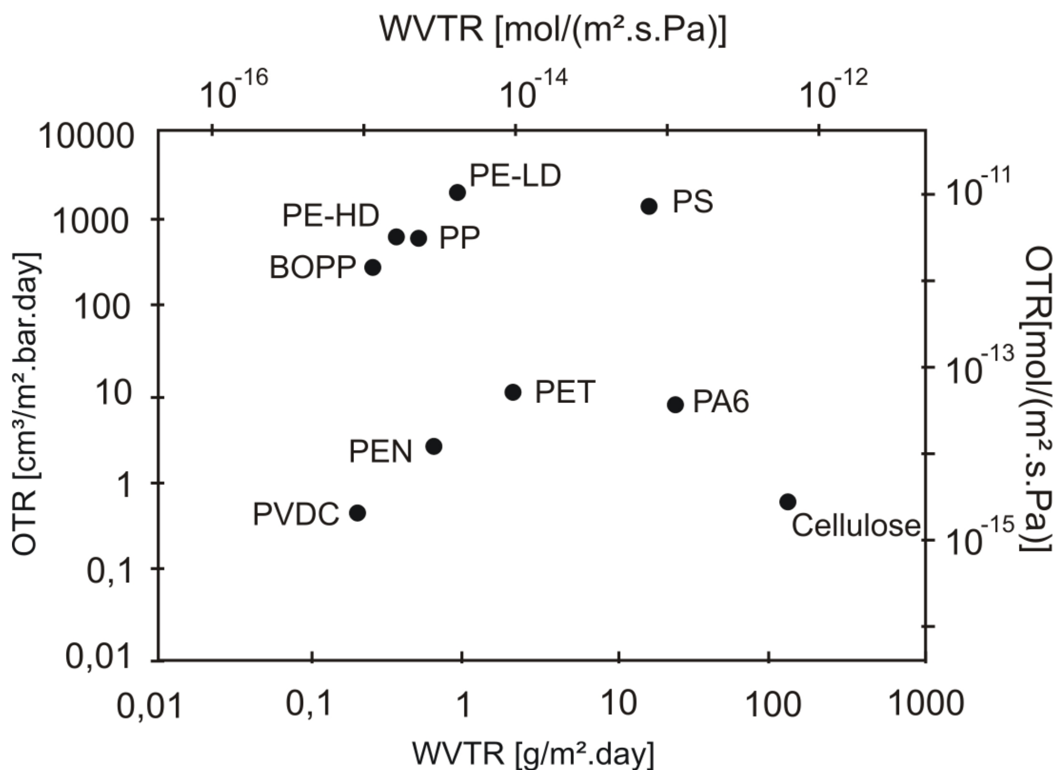

Fig. 4: Barrier properties of polymeric films standardised on 100 µm , OTR was measured at 23℃ and 50 % relative humidity and WVTR at 23℃ and 85 % → 0% rel. humidity [22, 23]

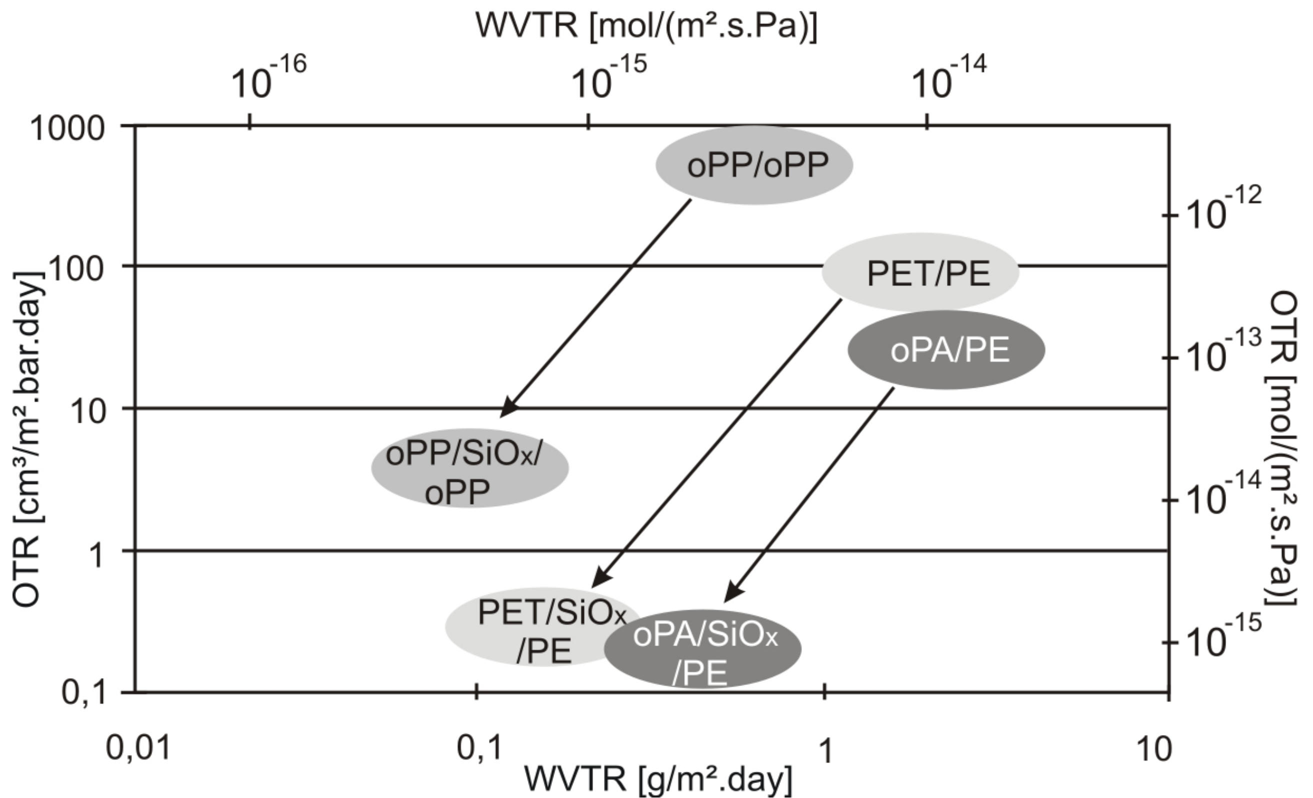

Fig. 5: Barrier improvements achieved in practice by an SiO_x coating process on different types of substrate films (OTR at 25°C 50 % r.h., WVTR at 25°C 85 → 0%) [24]

2.2 Physical vapour deposition in vacuum

Physical vapour deposition (PVD) is fundamentally a vaporisation coating technique, involving transfer of material from a solid initial state and its condensation on a substrate surface. By controlling the evaporation rate and the time, very thin films of the coating material can be deposited with layer thicknesses from 1 nm up to 1 µm. Practically all metals, many of their oxides and alloys and a number of other elements and compounds are suitable for deposition as thin layers on substrates by means of a physical vapour deposition process. The list of substrates includes, but is not limited to: PE, PET, BOPP, PC, paper, metal foils, and textile webs.

In the packaging industry, substrates such as PET and BOPP can be coated with aluminium, transparent aluminium oxide or silicon oxides by boat evaporation and electron beam evaporation. [25]

2.2.1 Evaporation and layer growth

In the evaporation process the source material is heated and vaporised either from the liquid state (most metals, alloys and some oxides) or sublimed from solid state (some metals, oxides). The speed range of the deposition is strongly limited in practice: during very slow deposition with low evaporation temperatures the evaporated steam reacts with the residual gas creating a layer, which may contain many impurities. This can be eliminated by carrying out the deposition process under very high vacuum. Too high deposition rates lead to some negative effects: the pressure over the depositing material is high, evaporated particles collide and scattering of evaporated particles in all directions occurs. For this reason the effectiveness of deposition decreases. It is desirable to regulate the process exactly to obtain a constant condensation rate leading to a qualitative layer within stable properties. In practice the deposition pressure is lower than 0,1 Pa (10^{-3} mBar).[26]

The evaporated particles and residual gas molecules react when they reach the polymer surface together. Therefore the created layer is contaminated with the molecules of residual gas or final products of their chemical reactions [26]. In industrial batch coaters for large sized substrates, it is H_2O which represents the dominating component of the residual gas. During venting, water vapour is absorbed in large quantities inside the plant by randomly grown deposits and desorbed during the pump down and coating process from the parts inside the chamber as well as from the deposited substrate itselfs. In consequence, the final pressure attained in batch-type plants at reasonable pump-down rates is about 10^{-2} – 10^{-3} Pa only. Here about 50 % or more of the residual gas is H_2O [27].

The energy of the evaporated particles depends only on the temperature of the evaporating source if no collisions between the evaporated particles and residual gas molecules take place. The residual gas molecules in the deposition chamber collide with the evaporated particles and transmit their energy. Therefore the energy of the evaporated particles decreases during the transport phase and also the deposition rate decreases [26, 28].

The particles evaporated during the deposition process have the average kinetic energy E_k [26]:

$$E_k = \frac{mv^2}{2} = \frac{3}{2} kT_V \qquad (9)$$

where m is mass of the evaporated particles

k is $1{,}38{,}10^{-23}$ J.K^{-1}

T_v is temperature of the evaporating source in K

v^2 is square averaged speed of the evaporated particles

The vaporised particles have certain mobility when they reach the substrate. So the particles can diffuse on the substrate surface until they fix themselves to a final position (see the fig. 6). The layer growth process depends on the interactions between atoms of the substrate and atoms of the deposited layer. In the case that the interaction between atoms of the substrate and the deposit (adhesion) is much higher than the interaction energy of the deposited atoms (cohesion); a layer grows and a next layer will grow after the previous layer is completed layer by layer growth. Island growth appears when the interaction energy of the deposited atoms (cohesion) is larger than the adhesion strength between the deposited atoms and the substrate atoms [26, 29].

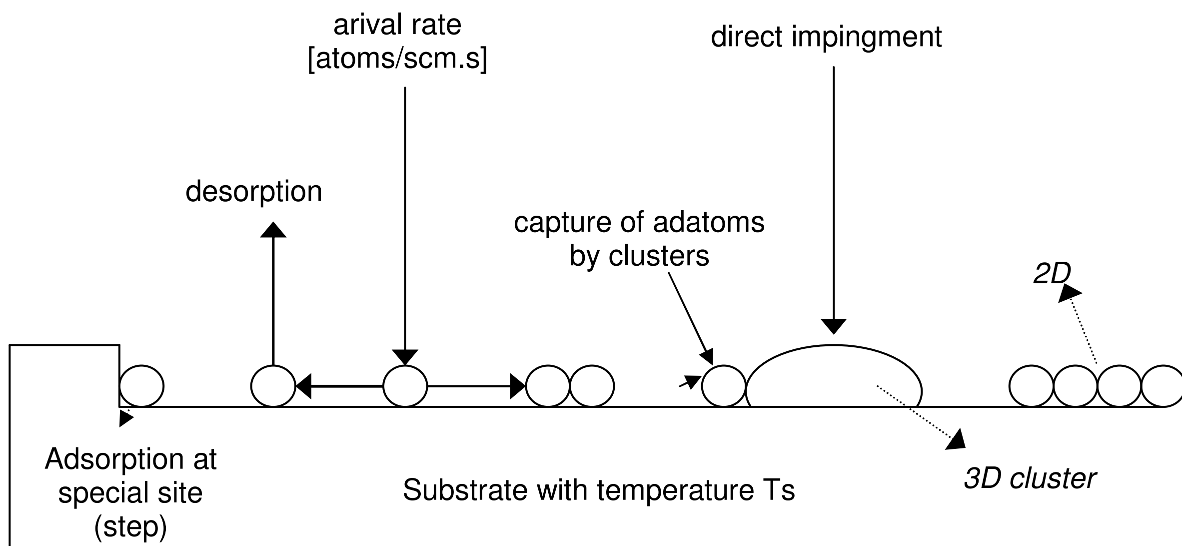

Fig. 6 : Schematic drawing of basic processes on the substrate surface [29]

Sometimes some of the impinged particles do not condense. The ratio of condensed atoms to the total number of the impinged atoms is called sticking coefficient. The sticking coefficient above the critical temperature is zero and under the critical temperature condensation coefficient increases up to one in wide temperatures interval. This interval is different according to the combination of the evaporation material and substrate. The materials with the higher boiling point condense better than the material with a lower one. Empirically the condensation coefficient of the material with boiling point higher than 1500 ℃ is nearly one at room temperature.[26, 28]

2.2.2 E-beam evaporation

Electron beam evaporation is based on the heating of an evaporation material by the transformation of the kinetic energy of accelerated electrons into thermal energy so that the evaporation temperature of material is reached. The electron beam is generated by a filament (cathode) which is connected to a negative high voltage. The electron beam is accelerated towards the anode and is focused by a so-called Wehnelt electrode, which is at cathode potential. A magnetic field can be used to deflect an electron beam. The deflection of the electrons takes place at right angles to the direction of the field and it is performed either by a permanent magnet or by an electromagnet.

Besides the heating the electron beam causes additional effects, namely ionisation and excitation of gas atoms. On their path in the vacuum chamber the electrons of the electron beam strike residual gas atoms of the vaporised material. The electrons are knocked out of the outer electron orbits and the atoms are converted into charged positive ions. At pressure values above 10^{-2} Pa (10^{-4} mbar) the ionisation excitation effect of the electron beam can be seen on the electron beam evaporator. Luminiscent gas atoms excited by the electron bombardment are visible along the path of the electron beam [26, 30].

2.2.3 Types of Electron-beam evaporators

There are two different types of electron beam evaporators, sometimes referred to as electron beam guns, namely “Pierce system” and “Transverse guns”.

- Pierce system

It consists of a housing with the magnetic deflection and focusing foils and the electron beam generator consisting of a cathode, Wehnelt element and an aperture anode. The pole pieces for the magnetic field are located in the chamber. Pierce systems are designed for electron beam power from 5 kW to 200 kW. Their field of use comprises high power vapour coating units, such as roll coating units, in which high deposition rates are demanded (industrial large scale technique) [30].

- *Transverse system*

In these evaporators the electron beam generator, the deflecting coils and magnets and the fixed or rotary crucibles are combined in one structural unit. They are preferably used in power range from 2 kW to 20 kW. The accelerating voltage usually lies between 4 kV and 12 kV. This system is used in laboratory units, in vapour coating units for optical layers or for depositing functional layers on electronic elements. The beam must be focused as narrowly as possible to obtain high power densities which are sufficient to evaporate. At the impingement point the cross-sectional area of the electron beam on the material in the crucible should not exceed 0,5 cm^2. The e-beam guns of this type are usually used for production of optical coatings for optical devices [26, 28, 30]. Schematic representation of a typical electron beam evaporation source is shown in figure 7.

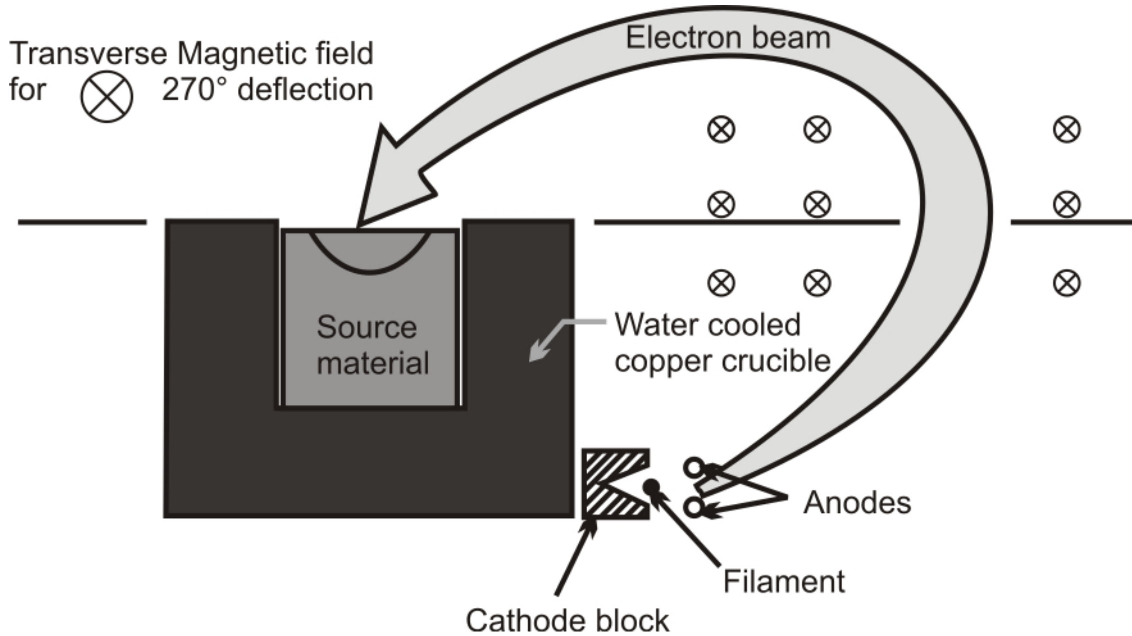

Fig.7: Schematic representation of a typical electron beam evaporation source [28]

2.3 Inorganic transparent barrier coating on the polymers.

The first commercial transparent coating that appeared on the market was a silicon oxide SiO_x ($1 < x < 2$) deposited on polyethylene terephtalate (PET) films. Subsequently, aluminium oxides as well as oxides of tin and magnesium or mixtures of such compounds have been tested for their barrier properties. However the most widely available coatings on the market until now are silicon or aluminium oxide compounds [31, 33].

2.3.1 Silicon oxide layers

Silicon monoxide (SiO) and silicon dioxide (SiO_2) evaporating materials are well adapted for thermal evaporation such as e-beam evaporation. The physical properties of different source materials and evaporation conditions are given in table 2.

Table 2: Properties of silicon and silicon oxide source materials [34]

Source material	Bulk density [g/cm³]	Melting point [°C]	Temperature in °C at different vapour pressure		Vapour species
			1 Pa	**10 Pa**	
Si	2,3	1410	1630	1830	Si
SiO	2,1	1705	1080	1180	SiO
SiO_2	2,2	1713	2000	2200	SiO, O_2

Silicon oxide (SiO_x) layers have excellent barrier properties when x is up to 1,8 (see fig. 8). [31, 32, 34, 35]. There is the hypothesis that the silicon dioxide atomic network contains spaces in its structure that the gas molecules can diffuse through [31]. In contrast, when $x < 2$, dangling bonds on silicon sites deform the network, connecting and tightening the structure and so reduce the gas diffusion [31]. However the layers near to $x = 1$ have yellowish tone and the using of these kind of yellowish layers in food packaging is not favourable. Consequently, the commercial layers are produced with an elementary ratio x of about 1,8, so that the barrier properties and full transparency in VIS range can be provided.

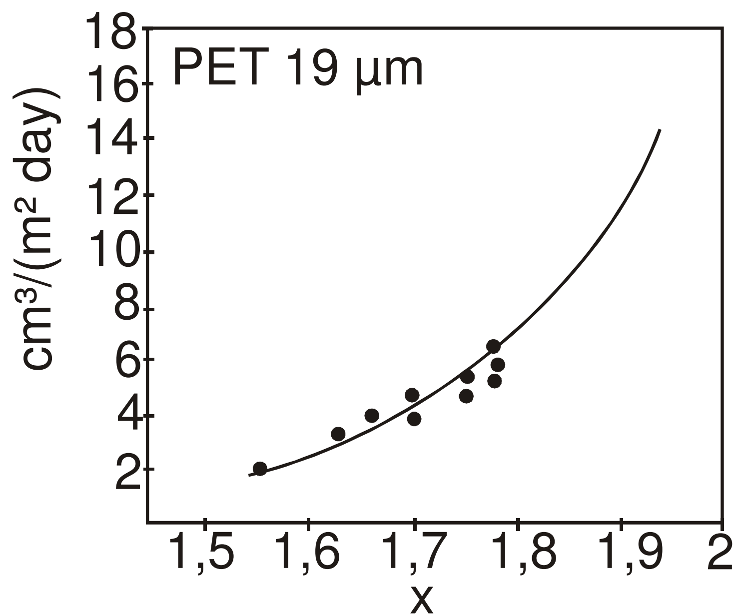

Fig. 8: Oxygen transmission rates (measured at 23°C and 75% r. h.) vs. x of SiO_x coated PET [37]

Also the layer thickness strongly influences the barrier properties. The fig. 9 shows that a thin layer, which does not cover completely the substrate roughness, can not guarantee the sufficient barrier properties. A very thick layer is on the other hand easily breakable. Cracking and peeling are generally observed for layer thickness greater than 150 nm [31, 35].

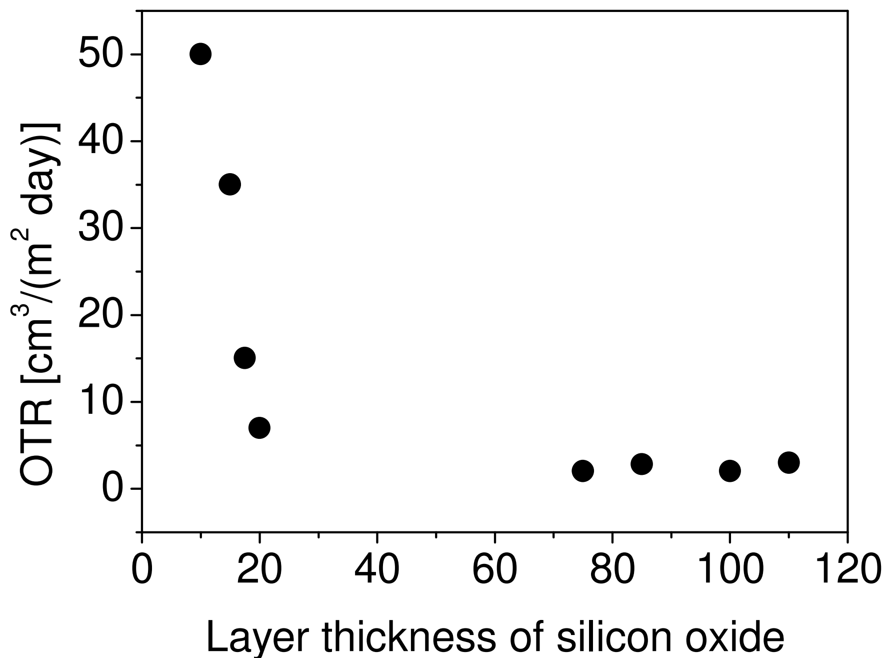

Fig. 9: Oxygen transmition rates (measured at 23℃ and 75% r. h.) vs. layer thickness of SiO_x coated PET [35]

The optical properties of the SiO_x materials such as refractive index, dielectric function or band gap, vary smoothly and continuously between the silicon and silicon dioxide characteristics. Optical data of silicon monoxide and silicon oxide SiO_x (x ~ 1,5) are shown in fig. 11 and 12 along with data for amorphous silicon and silicon dioxide (fig. 10 and 13 respectively). In the case of the silicon oxide (with an x value above 1,5) the region of strong absorption can be seen above ~ 9 eV (~138 nm). The spectrum of the SiO_x indicates the same features as silicon dioxide though the absorption peaks of SiO_x are less sharp and shifted towards lower energies. The curve of the silicon monoxide is different and more similar to the spectrum of the amorphous silicon. The maximum of absorption takes place in the energy region below ~ 6 eV (~206 nm) and the peak is lower and much broader. [36 – 38],

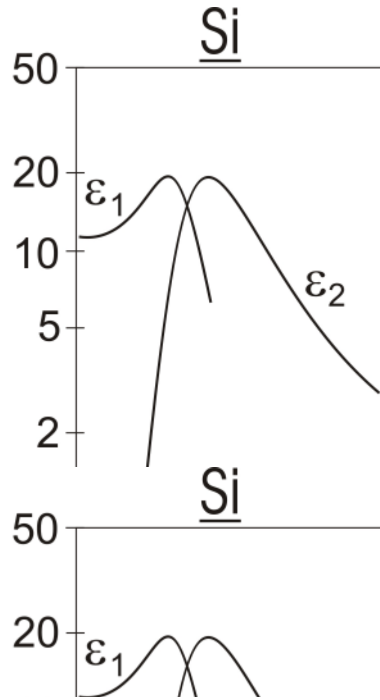

Fig 10. : Dielectric function ($\tilde{\varepsilon} = \varepsilon_1 + \varepsilon_2 i$) of amorphous Si [36]

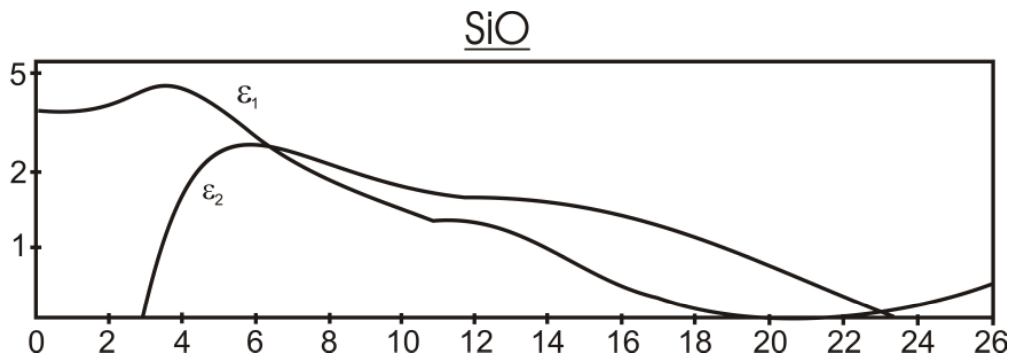

Fig 11. : Dielectric function ($\tilde{\varepsilon} = \varepsilon_1 + \varepsilon_2 i$) of silicon monoxide SiO [36]

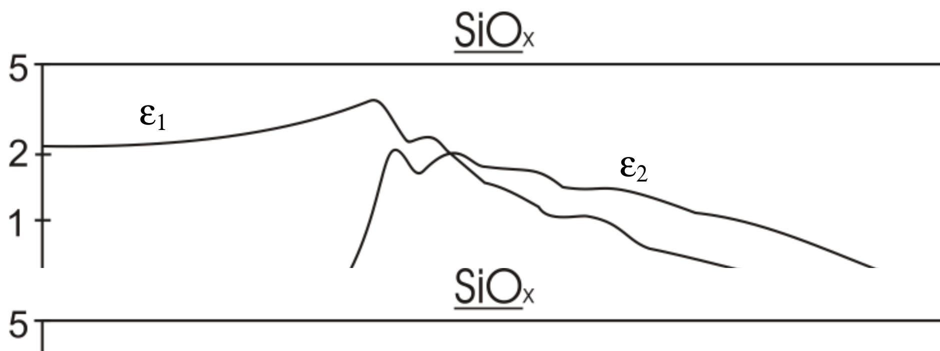

Fig 12. : Dielectric function ($\tilde{\varepsilon} = \varepsilon_1 + \varepsilon_2 i$) of silicon oxide SiO_x (x>1,5) [36]

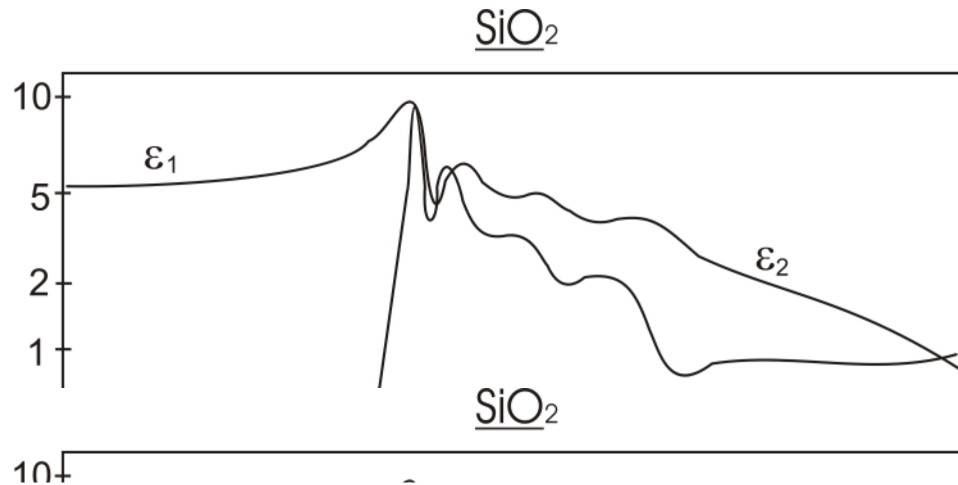

Fig 13. : Dielectric function ($\tilde{\varepsilon} = \varepsilon_1 + \varepsilon_2 i$) of silicon dioxide SiO_2 [36]

In some cases the amorphous material holds some regularity in its atom distribution and the material may be considered like "optically ordered" despite that the material is still amorphous on the basis of other experiments. [36]

2.3.2 Aluminium oxide layers

Production of aluminium oxide coatings has been carried out by a wide variety of methods. Especially for food packaging applications reactive evaporation from metallic aluminium is used because of the high deposition rate. The aluminium is heated and evaporated from a resistance-heated boat or from an e-beam heated crucible. Oxygen is added to the vapour by suitably arranged inlet nozzles. The mixture of Al vapour and oxygen is activated in a plasma zone so that an aluminium oxide layer is deposited on the polymeric film substrate through a reactive process. With the electron beam it is also possible to evaporate aluminium oxide instead of pure aluminium. However this way is not preferable in the industry because of the higher costs and also due to the fact that the oxide films thermally deposited directly from aluminium oxide targets have not significantly better quality. [39]

Table 3: Properties of aluminium and aluminium oxide source materials [31]

Source material	Bulk density [g/cm³]	Melting point at p = 10^5 Pa [°C]	Temperature in °C at vapour pressure in Pa		Vapour species
			1	10	
Al	2,7	660	1140	1270	Al
Al_2O_3	4,0	2046	2050	2200	Al, O, AlO, Al_2O, O_2

As in the case of the silicon oxide layers, good barrier properties of the aluminium oxide films depend on the stoichiometry, layer structure and layer thickness of the deposited coating. The barrier properties of the aluminium oxide layers depend on the layer thickness, so that the very thin layer do not establish sufficient barrier against vapours and gases. The barrier properties of the layer can be observed in the case of the layers thicknesses higher than 15 nm and they give a good barrier properties at a layer thickness of about 15 – 80 nm (see fig. 14) [40 – 42]. Above about 80 nm, the barrier effect reduces due to sensitivity of the metal oxide layers to mechanical stress [40, 42]

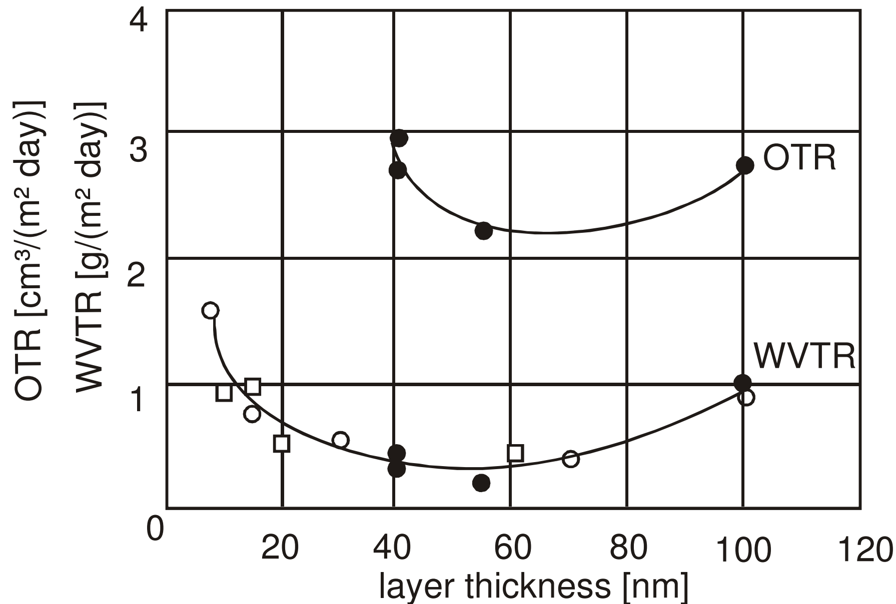

fig. 14: Oxygen (OTR) and water vapour (WVTR) transmission rates as a function of AlO_x barrier layer thickness (□ Al_2O_3 evaporation (12 µm PET), ○ reactive Al evaporation (12 µm PET), ● reactive Al evaporation (36 µm PET)) [42]

Crystalline aluminium oxide is transparent from 145 nm to 5,0 µm. Optical anisotropy is small from the extremely ultraviolet to the infrared wavelengths and becomes larger in the microvawe region. Aluminium oxide has a direct band gap of 8,8 eV (~140 nm) and absorption peaks are placed at 9 and 13 eV (~138 nm and 95 nm). [43]

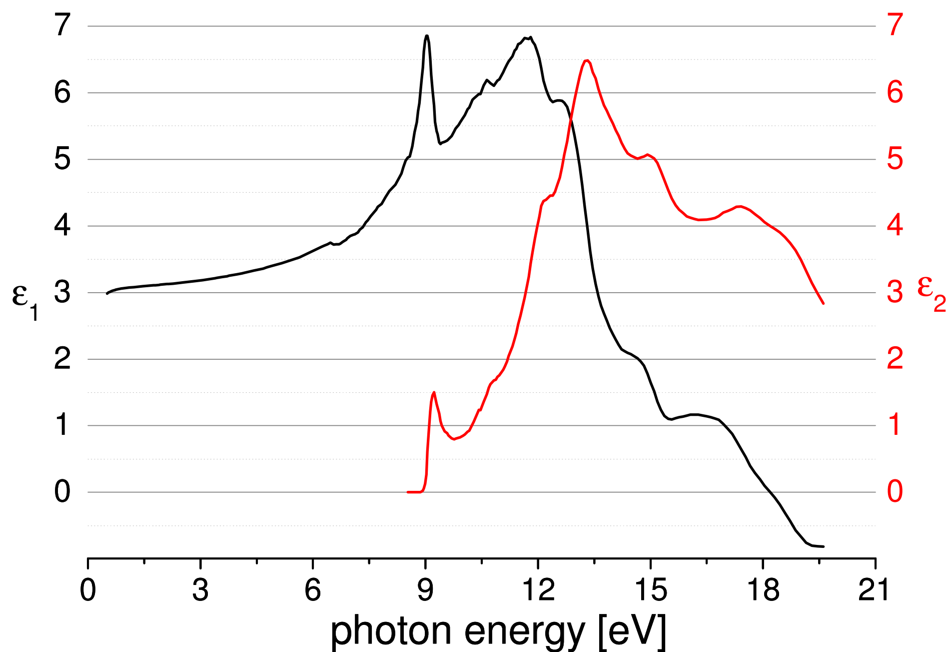

Fig. 15 Optical properties of aluminium oxide Al_2O_3 [43]

The crystallinity of aluminium oxide deposited films influences refractive index and extinction coefficient. The refractive index of the crystalline layer is larger than that of amorphous alumina and varies approximately from 1,6 to 1,9 at λ = 600 nm (~ 2,1 eV). [44, 45].

The values of refractive index are also strong influenced by the porosity of the deposited layer. While the refractive index of bulk Al_2O_3 material is 1,766 at λ = 633 nm (~ 2 eV), an aluminium oxide layer with a layer density of about 94 % has a refractive index slightly lower: n = 1,72. The refractive index of the aluminium oxide layers with very low density value (of 40 – 50 %) decreases dramatically to 1,3 – 1,4.[46]

2.4. Properties of Polyethylene Terephtalate

2.4.1 Functional properties of Polyethylene Terephtalate

Polyethylene therephtalate is the material most appropriate for high-vacuum roll coating. It gives no problems to equipment and process and is used for higher value products, e.g. for barrier packaging. Polyethylene terephtalate was first developed by a British company, Calico Printers, in 1941 for use in synthetic fibres. The second principal application of PET was film. DuPont first introduced Mylar® polyester film in the early 1950s. The amazing growth of PET in packaging began in the early 1970s with the technical development of stretch blow moulded PET bottles [47 – 49].

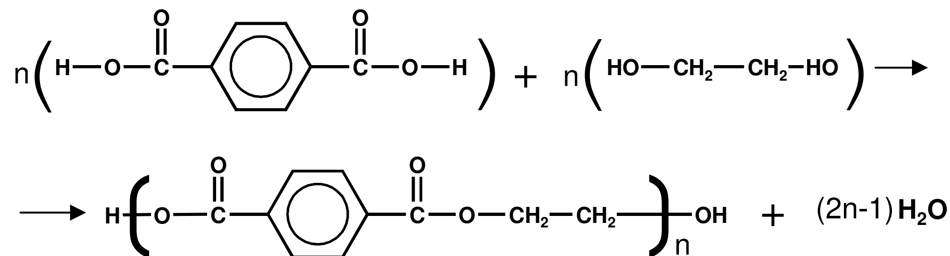

Fig. 16: Polycondensation of the terephthalic acid and 1,2 ethylendiol resulting to the polyethylene terephtalate [47]

Poly(ethylene terephathalate) films are produced by quenching extruded film to the amorphous state and then stretching the sheet in each direction at 80 – 100°C. In a two stages process into machine direction induce 10 – 14 % crystallinity and this is raised to 20 – 25 % by transverse orientation. In order to stabilise the biaxially oriented film, it is annealed under strain at 180 – 210 °C. This treatments lead to an enhancement of the crystallinity of the PET film of up to 40 – 42 % and the tendency to shrink because of a heating is reduced [50]. The typical properties of the commercial produced Polyethylene terephatalate film is given in table 4.

Table 4: Typical properties of commercially produced Polyethylene terephtalate film (Hostaphan® RD 12 µm) [47, 50, 51]:

t_g [°C] (glass transition temperature)	67	
t_m [°C] (melting temperature)	265	
Density [g/cm^3]	1,4	
Shrinkage (150 °C, 15 min.) [%]	Machine direction	1,4
	Transverse direction	0,1
Tensile strength (Test speed 100 %/min.;23 °C, 50 % r.h.) [N/mm^2]	Machine direction	250
	Transverse direction	270
Oxygen transmission rate (23°C 50% r.h.) [cm^3/(m^2 bar day)]	110	
Water vapour transmission rate (23°C 85 → 0% r.h.) [g/(m^2 day)]	16	

PET substrate provides good adhesion to deposited inorganic materials in account of the sufficiently high surface energy due to ester function groups. A surface modification like a plasma or corona pre-treatment is not required for increasing of the surface energy during deposition process. Untreated PET develops Si–C and Si–O–C bonds at aromatic ring sites as well as at carboxylic groups with SiO_x [31]. In industrial production, in spite of high surface energy, a pre-treatment is performed for an additional surface improvement.

2.4.2 Optical properties of Polyethylene terephtalate substrate

The ideal substrate for ellipsometric measurement would be opaque through the full measured spectral range or infinitely thick so that there is no interference of light reflected on the lower substrate interface. The second ideal property is the isotropy of the substrate material. Polyethylene-terephtalate films do not fulfil these requirements. Just as most of the polymeric films, PET exhibits an optical anisotropy through the orientation of the crystalline parts in bulk material and it is transparent in UV-VIS spectrum range [52 – 54].

The different properties in each direction of orientation complicate the ellipsometric measurement. The real and imaginary part of the complex refractive index of PET in

the VIS – UV energy range measured by spectroscopic ellipsometry (SE) in various orientations with respect to the plane of incidence are shown in fig. 15 and fig. 16. Therefore the spectroscopic ellipsometry measurement of the substrate before deposition was performed in the same orientation as deposited layers on substrate in the course of the deposition process. The spectra were measured in configuration: M = 0° and A = 45°, angle of incidence 70° [52] (see also chapter 2.3.3)

Fig. 15 and fig. 16 show the interference occuring up to 300 nm (~4 eV) coming from the multiple light reflection on film bottom interface of the transparent substrat. High optical transparency is the second problem of the ellipsometric analysis of a polymeric substrate as well as the layers deposited thereon. Absorption of PET films starts below 3 eV (400 nm) [52, 53]. For SiOx layers the absorption becomes significant below 4 eV (300 nm) depending on its stoichiometry and AlOx layer absorption start below 200 nm [43]. Accordingly the ellipsometric spectra were analysed over the absorption from 3,5 – 6,31 eV.

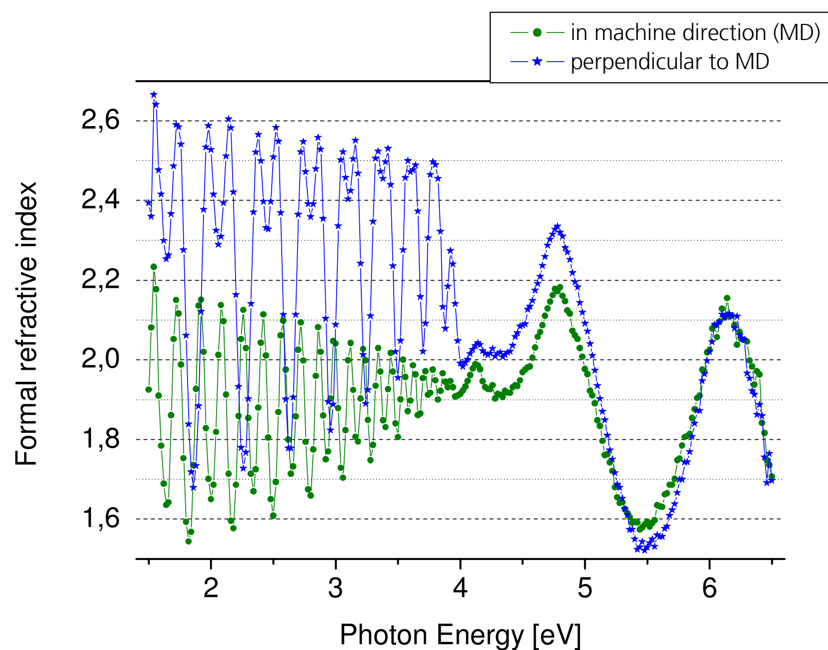

Fig. 15: Measured values of the formal refractive index n of the blank PET by spectroscopic ellipsometer at different orientation of the PET film relative to machine direction. [52].The formal refractive index includes layer and substrate and thus, interference effects from the substrate.

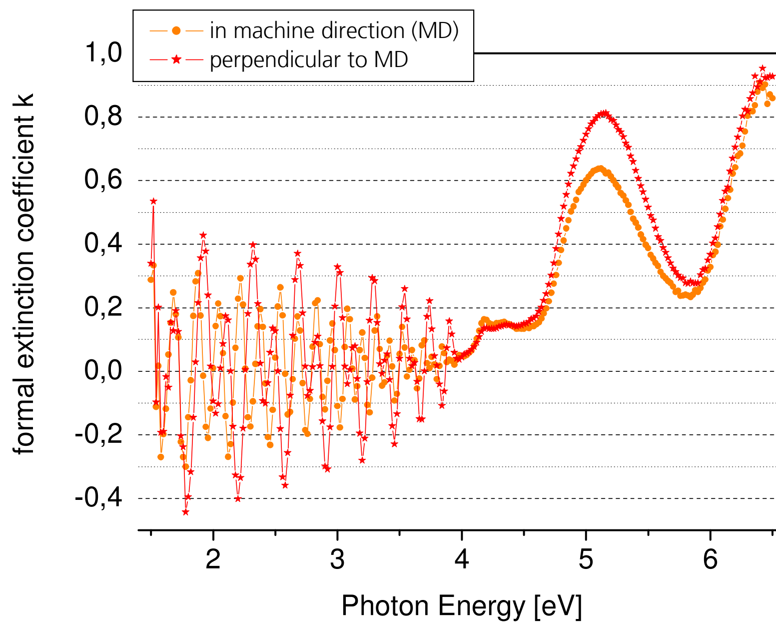

Fig. 16: Measured values of extinction coefficient k of the blank PET by spectroscopic ellipsometer at different orientation of the PET film relative to machine direction. [52]. The formal extinction coefficient includes layer and substrate and thus, interference effects from the substrate.

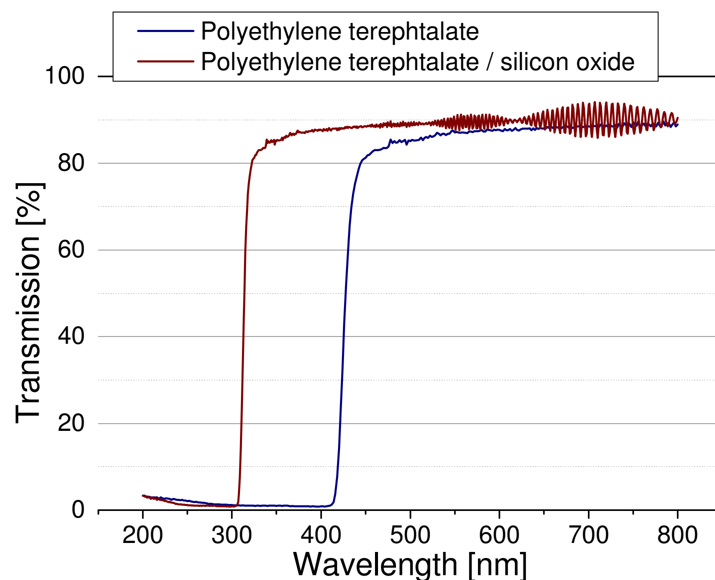

Fig. 17: Transmission spectra of the polyethylenterephtalate film (12 µm) without and with an SiOx layer (layer thickness 100 nm, stoichiometry (O:Si) = 1,8) on PET substrate [55].

2.5 Basic principles of Ellipsometry

Fundamental in the ellipsometric method is the study of the polarisation state of the light before as well as after reflection from a sample surface. The optical system interacts with light wave and changes its state of polarisation. In general, ellipsometry can be defined as a measurement of the state of polarisation of a light wave [56, 57].

The investigated samples are planar, in the liquid or solid state; they are optically isotropic or anisotropic and can be either in bulk or thin-film form. Ellipsometry is a usable technique for the determination of the optical properties of materials, especially in wavelength regions where the materials are strongly absorbing. However ellipsometry has some limitations, which are mostly caused by its sensitivity to effects such as surface contamination or surface roughness. These should be considered as potential sources of error in determination of the optical properties by this technique. In spectroscopic applications, both the real and imaginary parts of the complex refractive index (or dielectric function) can be determined as a function of wavelength [56, 57].

The ellipsometer measures changes in polarisation so it should be called polarimeter. However at the time when the ellipsometer was developed the term polarimeter was already in use as the name of an instrument for measuring the specific rotation of optically active materials. Since the general polarisation state of polarised light is elliptical, the term ellipsometer was chosen [56].

The radiation used for the ellipsometric measurement is a monochromatic electromagnetic radiation with a wavelength in the range of near UV, VIS and near IR. The coefficient of reflection follows the Fresnel laws of reflection, what means that the observed media are taken as continuous. The electric field vector of the electromagnetic radiation can be described as follows [58]:

$$E_x = a_x \cos(\tau+\delta_x) \quad (11)$$

$$E_y = a_y \cos(\tau+\delta_y) \quad (12)$$

$$\tau = \omega\,(t - z/\nu) \quad (13)$$

where ω and ν are the angular frequency and the phase velocity of the electromagnetic wave, respectively, whereas a_x and a_y are the amplitudes of a linear polarised light E_x and E_y. $(\tau+\delta_x)$ and $(\tau+\delta_y)$ are the phases and $\delta = \delta_x - \delta_y$ is the phase difference. These parameters indicate the type of polarisation (see fig. 18). Elliptical polarised light is defined by $\delta \neq k\pi$; k = 0, ±1, ±2…, circular polarised light by $\delta = \frac{\pi}{2}(2k+1)$; k = 0, ±1, ±2… $a_1 = a_2$ and linear polarised light is described by $\delta = k\pi$, k = 0, ±1, ±2… [57]

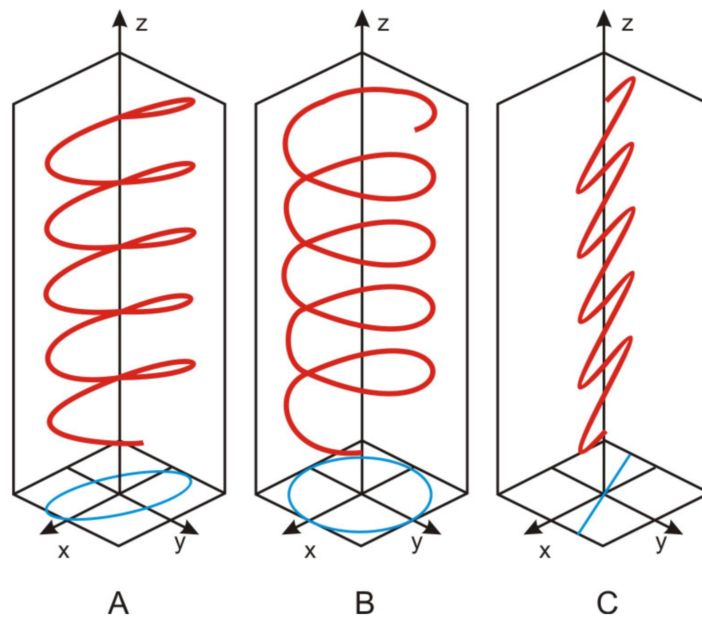

Fig. 18: Elliptical (A), circular (B) and linear(C) polarisation of the light

After mathematical operations, where the parameter τ is eliminated from formulas (11) and (12), the electric field vector of the wave can be also expressed by:

$$\left(\frac{E_x}{a_x}\right)^2 - \frac{2E_xE_y}{a_xa_y}\cos\delta + \left(\frac{E_y}{a_y}\right)^2 = \sin^2\delta \qquad (14)$$

where the ellipse axe *a* and *b* are shifted from the axis x, y and an angle ψ and the ellipse is inscribed into a rectangle with the side lengths of $2a_x$ and $2a_y$ (see fig. 19) [58]

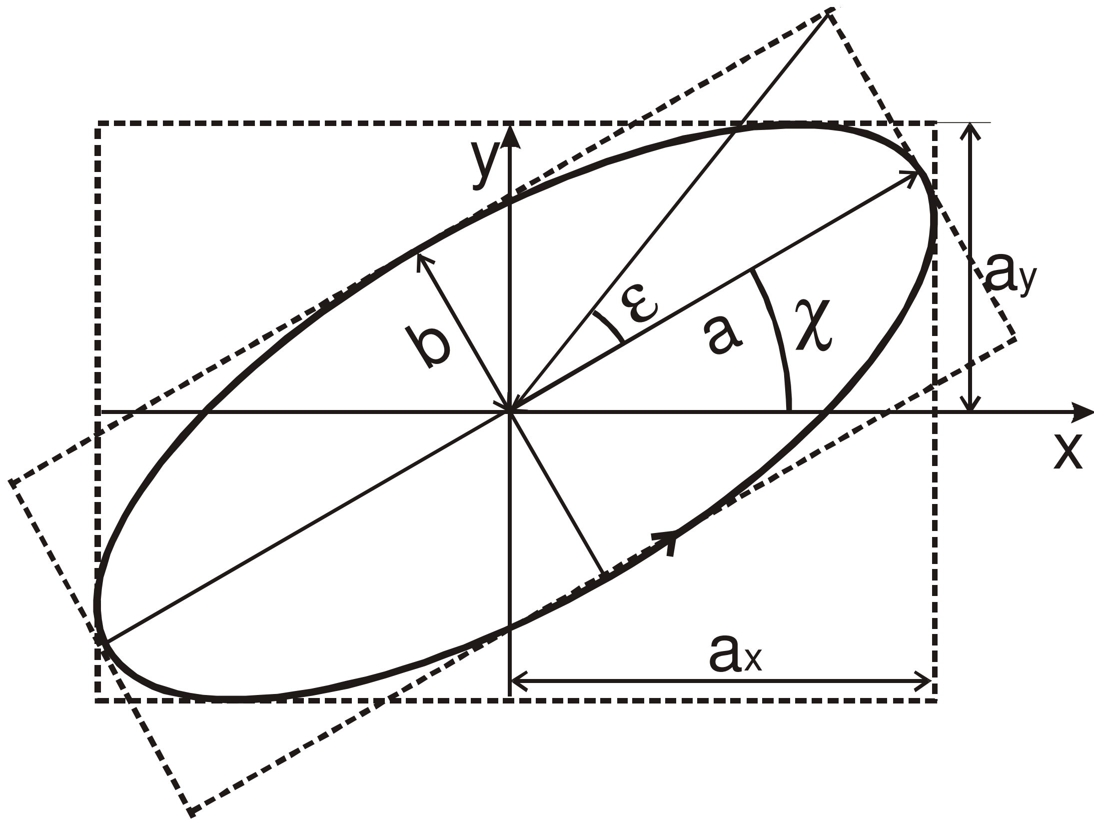

Fig. 19: Ellipse of the elliptical polarised light [58, 59].

The azimuth χ is the angle between the major axis of the ellipse and the positive direction of x-axis and determines the shift of the ellipse from the x-axis. The azimuths vary within the range $-\frac{1}{2}\pi \leq \chi < \frac{1}{2}\pi$. The ellipticity e is the ratio of the length of the minor half axis of the ellipse b to the length of its major half axis a; e = b/a. The ellipticity angle e^* (such that e = tan e^*) $-\frac{1}{4}\pi \leq e^* \leq \frac{1}{4}\pi$. The absolute phase δ determines the angle between the initial position of the electric vector at t = 0 and the major axis of the ellipse. The values of the absolute phase δ vary from -π to +π. [56, 57]

Every planar monochromatic electromagnetic wave can be splitted in two linear polarised components, where the polarisation plane of the first component is perpendicular to the polarisation plane of the second one (component p – the plane of polarisation is parallel to plane of incidence, component s – the plane of polarisation is perpendicular to the plane of incidence). The reflected polarised light is defined as [56, 58]

$$E_p = E_{0p}\tilde{r}_p \quad (15)$$

$$E_S = E_{0S}\tilde{r}_S \quad (16)$$

where $\tilde{r}_p$ and $\tilde{r}_S$ are the Fresnel complex amplitude reflection coefficients. These reflection coefficients describe the behaviour of the light after reflection. At the interface of the two absorbing media and for a general angle of incidence they are given by the expressions [56]:

$$\tilde{r}_p = \frac{\tan(\tilde{\varphi}_1 - \tilde{\varphi}_2)}{\tan(\tilde{\varphi}_1 + \tilde{\varphi}_2)} = \frac{\tilde{n}_2 \cos\tilde{\varphi}_1 - \tilde{n}_1 \cos\tilde{\varphi}_2}{\tilde{n}_2 \cos\tilde{\varphi}_1 + \tilde{n}_1 \cos\tilde{\varphi}_2} \quad (17)$$

$$\tilde{r}_s = \frac{\sin(\tilde{\varphi}_1 - \tilde{\varphi}_2)}{\sin(\tilde{\varphi}_1 + \tilde{\varphi}_2)} = \frac{\tilde{n}_1 \cos\tilde{\varphi}_1 - \tilde{n}_2 \cos\tilde{\varphi}_2}{\tilde{n}_1 \cos\tilde{\varphi}_1 + \tilde{n}_2 \cos\tilde{\varphi}_2} \quad (18)$$

where $\tilde{\varphi}_1$ and $\tilde{\varphi}_2$ are complex refraction angles and $\tilde{n}_1$ and $\tilde{n}_2$ are the complex refractive indexes of the absorbing media 1and 2 ($\tilde{n} = n_i + ik_i$)

$$\tilde{\rho} = \frac{\tilde{r}_p}{\tilde{r}_S} = \left|\frac{r_p}{r_S}\right|.e^{i(\delta_p - \delta_S)} = \tan\psi.e^{\Delta i} \quad (19)$$

$\tilde{\rho}$ is named as complex reflection ratio and from this quantity the other optical constants (e.g. complex dielectric function $\tilde{\varepsilon}$) of the material can be extracted. [59]

The complex dielectric function $\tilde{\varepsilon} = \varepsilon_1 + \varepsilon_2 i$ is the quantity, which can be directly related to the material properties, and is connected to the refractive index through the following equation [59]:

$$\tilde{\varepsilon} = \varepsilon_1 + \varepsilon_2 i = \tilde{n}^2 = (n + ki)^2 \quad (20)$$

$$\downarrow$$

$$\varepsilon_1 = n^2 - k^2 \quad (21)$$

$$\varepsilon_2 = 2nk \quad (22)$$

Two quantities, ψ (which measures the amplitude ratio) and Δ (which measures the relative phase change) are directly related to the characteristics of the ellipse [56, 57] :

$$\cos 2\psi = \cos 2\varepsilon \cos 2\chi \tag{23}$$

$$\tan \Delta = \tan 2\varepsilon / \sin 2\chi \tag{24}$$

2.5.1 Interface non-absorbing medium – absorbing medium

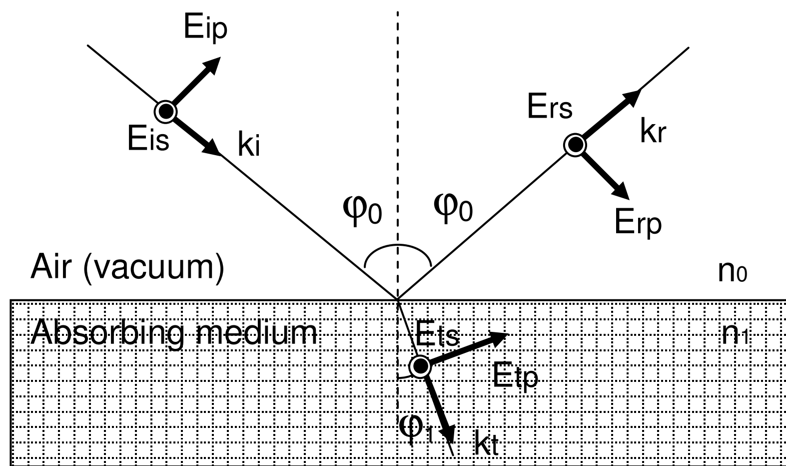

Fig. 20: Light propagation in the system: vacuum (air) –substrate [59]

The fig. 20 shows the light propagation before (E_i) and after reflection (E_r) of the light on the substrate and transmission of the light (E_t) into the substrate. The light is reflected at the planar interface between a substrate phase of the given material and an ambient phase of known optical properties. The typical system is the substrate placed in air or vacuum. The complex refractive index $\tilde{n}_0 = n_0$ and from the equations (17), (18) and (19) comes to [56]:

$$\tilde{\rho} = \frac{\tilde{r}_p}{\tilde{r}_S} = \left|\frac{r_p}{r_S}\right| . e^{i(\delta_p - \delta_S)} = \tan\psi . e^{\Delta i} = -\frac{\cos(\varphi_0 + \tilde{\varphi}_1)}{\cos(\varphi_0 - \tilde{\varphi}_1)} . \tag{25}$$

In this case of an interface of vacuum (air) – absorbing medium or interface of vacuum (air) – non-absorbing medium, the ellipsometric angles Δ and ψ are in the interval: 0°< Δ < 180° and 0°< ψ < 45°.

The complex dielectric function of a bulk material with smooth surfaces can be directly calculated from complex reflection ratio $\tilde{\rho}$:

$$\tilde{\varepsilon} = \tilde{\varepsilon}_0 \sin^2 \varphi \left\{ 1 + \left(\frac{1-\tilde{\rho}}{1+\tilde{\rho}} \right)^2 tg^2 \varphi \right\} \tag{26}$$

where φ is the angle of incidence of the beam, and $\tilde{\varepsilon}_0$ is the complex dielectric function of the ambient medium – vacuum (air) [59].

2.5.2 Three-phase (vacuum (air) – thin film – substrate) system

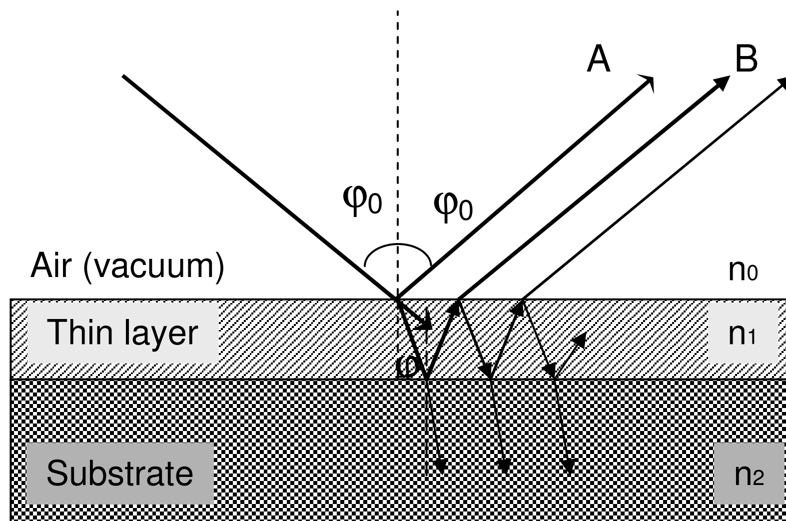

Fig. 21: Light propagation in system: vacuum (air) – thin film – substrate [59]

When the penetration depth of monochromatic radiation is larger than the medium thickness, which corresponds to the case of a thin layer (medium 1) grown on a substrate (medium 2), then the light is back-reflected at the layer – substrate interface, it is transmitted again through the layer and finally goes out to vacuum (medium 0). This situation can be described by the expressions:

$$\tan\psi . e^{i\Delta} = \left(\frac{r_{p(01)} + r_{p(12)} . e^{-2i\delta}}{1 + r_{p(01)} r_{p(12)} e^{-2i\delta}}\right)\left(\frac{1 + r_{S(01)} r_{S(12)} e^{-2i\delta}}{r_{S(01)} + r_{S(12)} . e^{-2i\delta}}\right) \tag{27}$$

where $r_{p\ (01)}$, $r_{p\ (12)}$, $r_{s\ (01)}$, $r_{s\ (12)}$ are the Fresnel coefficients of the reflection for the components p and s on the interfaces medium 0 → medium 1 and medium 1 → medium 2, and δ is the phase change of the light in the film. Namely [59]:

$$\delta = \frac{2\pi}{\lambda} d_1 \left(\tilde{n}_1 - n_0^2 \sin^2 \varphi_0\right)^{1/2} \tag{28}$$

where d_1 is the thickness of the thin film, λ is the wavelength of the monochromatic light, φ_0 is angle of the incidence, n_0 is the refractive index of the air (vacuum) and $\tilde{n}_1$ is complex refractive index of the thin film.

The ellipsometric angles Δ and ψ (measured with monochromatic light) depend on seven parameters as it results from previous expressions: $\Delta = f_1(n_0, n_1, k_1, n_2, k_2, \varphi_0, d_1)$ and $\psi = f_2(n_0, n_1, k_1, n_2, k_2, \varphi_0, d_1)$ [56], but only two characteristics of the sample can be assessed from the (two) ellipsometric angles. If a transparent film on a known substrate is considered, the refraction index and the film thickness of the transparent non-absorbing layer can be calculated. For a thin optically absorbing layer with unknown complex refraction index and thickness on a known substrate, there are three unknown parameters and these cannot be determined from a single measurement. This is sometimes called the fundamental problem of ellipsometry. [56]

2.5.3 Spectroscopic phase modulated ellipsometry

Different measurement techniques exist for the determination of the ellipsometric parameters. All of them use the same optical components: a source, a polarizer, an analyzer and a detector. To these basic elements other components like modulators or compensators can be added. The typical configuration of the spectroscopic ellipsometer is shown in fig. 22:

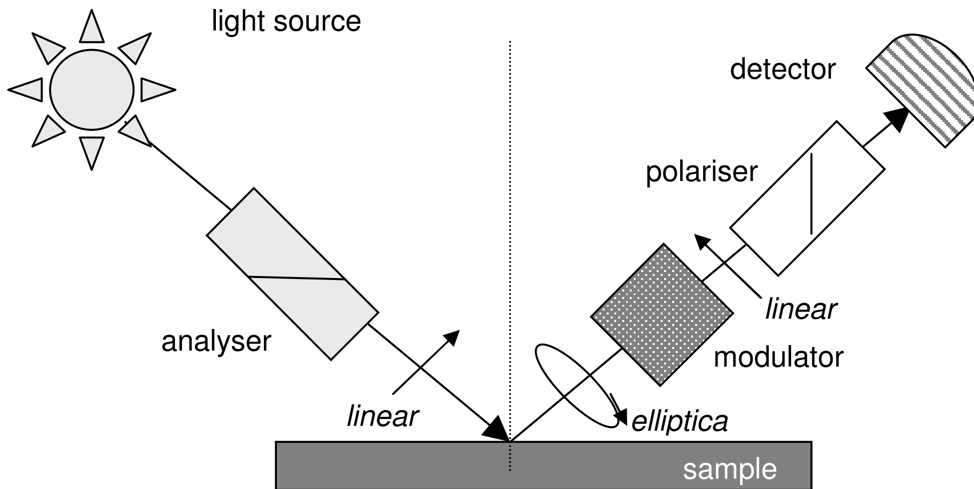

Fig. 22: Spectroscopic phase modulated ellipsometer [59]

In the phase modulation technique, the reflected light is modulated by a photo-elastic modulator. A strained piece of amorphous silica is used to modulate the state of polarisation of the light. The silica becomes birefringent when strained, with the amount of birefringence (the phase retardation of a light beam passing through the optical element) being proportional to the strain. The strain is applied by piezoelectric transducers at the resonance frequency of 50 kHz. The resulting detector signal has a large unmodulated component, with two superimposed modulated signals at 50 and 100 kHz (and higher harmonics). The ellipsometric parameters can be directly deduced from these modulated signal I [59]:

$$I\ (\lambda,t) = [I_0 + I_s \sin\delta(t) + I_c \cos\delta(t)\ldots] \quad (29)$$

$$\delta(t) = A_0.\sin\omega' t \quad (30)$$

where A_0 is the modulation amplitude which is proportional to (V_m/λ), V_m is the excitation voltage applied to modulator, λ the wavelength of the light and ω' the modulation frequency.

The detected signal is Fourier analysed to determine the parameters I_s and I_c, which generate the parameters of interest namely ψ and Δ.

For the configuration of the measurement, where the orientation of the modulator M = 0° the polariser orientation is P = 45° and analyser orientation is A = 45° with respect to the plane of incidence [59]:

$$I_0 = 1 \tag{31}$$

$$I_s = \sin 2\psi \sin \Delta \tag{32}$$

$$I_c = \sin 2\psi \cos \Delta \tag{33}$$

This technique could be fully employed in the last years, when the computer control permit to develop fast spectroscopic phase modulated ellipsometer that can scan an entire range of wavelength simultaneously. [59]

Spectroscopic ellipsometry is a model dependent technique and for determination the demanded physical quantities (dielectric functions, refractive indices, material compositions, film thickness etc.) a mathematical model is required. The real data of the effective quantity such as effective dielectric function, that carries information of the substrate, measured thin layers and layer thickness are compared in the fitting process to adjust the theoretically built sample (previously built) to the experimental data (real measure)**.** The data fitting is performed using a fitting algorithm (e.g. Levenberg-Marquardt, Simplex) [57].

2.5.4 Tauc-Lorentz model

The Tauc-Lorentz model is a mathematical model commonly used to calculate the optical properties of amorphous semiconductors. It uses the Tauc expression for the imaginary part of the dielectric function near the band edge [60]:

$$\varepsilon_2(E) = A\frac{(E-E_g)^2}{E^2}\Theta(E-E_g) \tag{34}$$

where E_g is the band gap of the material and Θ is the Heaviside Theta function, where $\Theta(E<0) = 0$ and $\Theta(E\geq0) = 1$. This expression is applied to fit optical transmission data near the band gap, where the real part of the dielectric function is

constant. By multiplying the Tauc expression with the complex dielectric function for a Lorentz oscillator the Tauc-Lorentz expression for the imaginary part of the complex dielectric function is obtained.

The Lorentz oscillator approximation is given by.[61 – 63]:

$$\varepsilon(E) = \varepsilon(\infty) + \sum_{i=1}^{N} \frac{A_i}{E_i^2 - E^2 - i\Gamma_i E} \tag{35}$$

where ε (E) is the complex dielectric function as a function of photon energy, $\varepsilon(\infty)$ is the real part of the dielectric function as the energy goes to infinity, A_i is the amplitude, Γ_i is the broadening and E_i is the center energy of the i-th oscillator, respectively.

Tauc-Lorentz expression parameterises interband absorption above the band edge [64]:

$$\varepsilon_2(E) = \frac{AE_0C(E - E_g)^2}{E\left[(E^2 - E_0^2)^2 + C^2E^2\right]} \qquad E>E_g \tag{36}$$

.

$$\varepsilon_2\ (E) = 0 \qquad E \leq E_g \tag{37}$$

The imaginary part of the dielectric function is computed as a function of four parameters: The gap energy (E_g), the resonance frequency (E_0), the transition strength (A) and a damping constant (C), which in this context, has the meaning of a broadening constant. The Tauc-Lorentz (TL) expression is empirical and only valid for interband transitions. The dielectric response from infrared transition, Urbach tail effects and core transitions are not included. Since the Tauc-Lorentz model gives an expression for the imaginary part of the dielectric function only the real part is obtained by Kramers-Kronig transformation [65]:

$$\varepsilon_1(\omega) = \varepsilon_\infty + \frac{2}{\pi} P \int_{E_g}^{\infty} \frac{\xi \varepsilon_2(\xi)}{\xi^2 - \omega^2} d\xi \quad (38)$$

The resonance frequency E_0 (Penn gap), which is the absorption maximum, correlates with the band gap and therefore with the stoichiometric ratio of the transparent semiconducting layers such as silicon oxide layers (SiO_x) [38] (s*ee also chapter 2.4)*

2.6 Statistical methods used for data analysis

Statistics can be divided into two major areas: *Descriptive statistics* devote the summarisation and description of data (population or sample). It comprises the statistical methods, which deal with the collection, tabulation and summarization of data. *Inferential statistic* uses sample data to make an inference about a population.

2.6.1 Descriptive statistics

Descriptive statistics describes patterns and general trends in a data set. In some sense, descriptive statistics is one of the best ways for understanding the experimental results. The data are used to find reliable differences or relationships, and to estimate population values from these reliable findings. Typically the data are reduced down to one or two descriptive summaries. For average the arithmetic mean, median or mode is used. The variability and relationships in data set are described by some of the parameters such as the standard deviation (sample variance), the range or correlation and by visualisation of the data through various graphical procedures like histograms, frequency distributions, and scatterplots.

2.6.1-1 The Mean, the Median and the Mode

Mean $\bar{x}$ - The arithmetic mean is what is commonly called the average; the mean is the sum of the data values divided by the number of data variables (n):

$$\bar{x} = \frac{\sum x_i}{n} \quad (39)$$

The mean is greatly influenced by all variables of the data set and therefore more sensitive to outliers (single observations far away from the rest of the data). However the arithmetic mean is favourably used because of its true physical meaning. In this

calculation there is the assumption of a normal distribution or that the data do not deviate too much from normality. [66 – 68]

Median $\tilde{x}$ - the median is a number that separates the higher half of a data set from the lower half, it means that half of the data values are smaller than the median value and half of the data are larger. That is, if x_1, x_2, ... ,x_n is a random sample sorted from the smallest to the largest value, then the median is defined as the value of the middle point in the data sequence. When the abundance of data is even, the median is calculated like the arithmetic mean of the two middle values in this ordered data sequence.

Median is preferred to be used in the case of:

- Rank-data
- Small abundance of the sample variables
- Asymmetric distribution
- Suspicion for the outliers

[66 – 68]

Mode $\hat{x}$ - the mode is the value occurring most frequently in a series of observations or statistical data. The mode is not necessarily unique, unlike the arithmetic mean and is often also used in qualitative observations, when it is not possible to numerically express the mean or the median. [66 – 68]

2.6.1-2 Variability and distribution in data set

Standard variance and standard deviation of mean – Standard variance is a parameter that describe how tightly all the various variables of sample are distributed around the mean. It is computed as the average squared deviation of each number from its mean [66 – 68]:

$$s_{\bar{x}}{}^{2} = \sum_{i=1}^{n} \frac{(x_i - \bar{x})^2}{n-1} \tag{40}$$

The sample standard deviation $s_{\bar{x}}$ is the square root of standard variance.

Standard deviation of median $s_{\tilde{x}}$ is expressed by:

$$s_{\tilde{x}} = \frac{(a-b)}{3,4641} \tag{41}$$

where *a, b* are the variables in data set. *a* is the variable at $\left(\frac{n}{2}+\frac{\sqrt{3n}}{2}\right)$ position and b at $\left(\frac{n}{2}-\frac{\sqrt{3n}}{2}\right)$ position in the ordered data set from the smallest variable to largest [67].

Range – is the difference between x_1 – the smallest variable and x_2 – the largest variable [66 – 68]:

$$R = x_2 - x_1 \tag{42}$$

2.6.2 Inferential statistics

Inferential statistics is used to draw inferences about a population from a sample. Typically the testing of the “null hypothesis” is used. The null hypothesis assumes nothing*:* no relationship, no difference, no effects. If the hypothesis whether there are differences between samples means is tested, the null hypothesis is: “there is no difference between the means of samples”. The alternative hypothesis contrary assumes something*:* some relationship, some difference, some effect. It can either be directional (mean of the first sample is larger than mean of the other one) or non-directional (the sample’s means are different). The hypothesis testing is performed always by concerning a defined probability level “α”. In the case that the null hypothesis is rejected at an α level of 0,05, there is a less than 5% chance that the results came from a population, in which the null hypothesis is actually true and so it is more than 95% certain that the means of samples are different [66 – 68]. The statistical operations used in the both statistical areas – inferential statistics and also descriptive statistics, are often dependent on the type of the sample (population) distribution. Therefore the first step of statistical data evaluation should be the testing for normality.

2.6.2-1 Normal distribution and tests for normality

Many kinds of data are approximated well by the normal distribution; therefore many statistical tests also assume that the data are normally distributed. However most of these tests work well even if the distribution is only approximately normal and in many cases as long as it does not deviate considerably from normality. [67]

The Shapiro-Wilk (W) Test for Normality

The test was developed by Shapiro and Wilk in 1965. Most authors agree that this is the most reliable test for non-normality for small to medium sized samples. It can be used for samples as large as 2,000 or as small as 3. The null hypothesis of the test is: "the sample is taken from a normal distribution". The *W* statistic is calculated as follows:

$$W = \frac{\left(\sum_{i=1}^{n} a_i x_{(i)}\right)^2}{\sum_{i=1}^{n} \left(x_i - \bar{x}\right)^2} \qquad (43)$$

where the $x_{(i)}$ are the ordered sample values ($x_{(1)}$ is the smallest) and the a_i are constants generated from the means, variances and covariances of the order statistics of a sample with a size *n* from a normal distribution [69, 70] The W value is tabled and the output is the p-value. If the chosen alpha level (probability level) is 0.05 and the p-value tabled according to calculated W found to be less than 0.05, then the null hypothesis that the data are normally distributed is rejected. If the p-value is greater than 0.05, then the null hypothesis is not been rejected. [67]

2.6.2-2 Testing of the differences between two samples

For a testing of the differences between two samples, parametric as well as non-parametric tests could be accomplished. Non-parametric tests do not require the normal distribution of the sample and also calculations in non-parametric tests are much simpler in comparison to parametric tests. However the power of non-parametric tests is lower than parametric ones [67, 68].

T-test compares the actual difference between the means in relation to the data variation (expressed as the standard deviation of the difference between the means). "Student" (real name: W. S. Gossett [1876-1937]) developed statistical methods to solve the problems stemming from his employment in a brewery. Student's *t*-test deals with the problems associated with the inference based on "small" samples: the calculated mean ($\bar{x}$) and standard deviation (s) may by a chance deviate from the "real" mean and standard deviation (i.e., what you'd measure if you had many more data items: a "large" sample). The parameter t of Student's test is expressed by:

$$t = \frac{signal}{noise} = \frac{difference \quad between \quad group \quad means}{vairiability \quad of \quad groups} = \frac{|\bar{x}_1 - \bar{x}_2|}{\sqrt{\frac{s_1^2}{n_1} + \frac{s_2^2}{n_2}}} \tag{44}$$

After calculation of the t-parameter, this is compared with the critical parameter t_k from the Student's distribution according to the calculated degrees of freedom. When the calculated *t* value is greater than t_k (alpha conventionally equal to 0.05), then the null hypothesis: "the two groups do not differ" is rejected and the alternative hypothesis that the groups are different is accepted. For application of the t-test for testing of the differences between means of two samples, the normality and independency of the sample variables have to be fulfilled. [66 – 68]

Mann-Whitney U test This test is a non-parametric alternative to the independent group t-test, when the assumption of normality is not met. Like many non-parametric tests, also Mann-Whitney test uses the ranks of the data to calculate the statistic instead of the variables themselves. The hypotheses for the comparison of two independent groups are: H_0: The two samples come from identical populations; H_A: The two samples come from different populations. The parameters U_1 and U_2 are expressed by:

$$U_1 = mn + \frac{m(m+1)}{2} - R_1 \tag{45}$$

$$U_2 = mn + \frac{n(n+1)}{2} - R_2 \tag{46}$$

$$U_1 + U_2 = mn \tag{47}$$

Where m, n are number of variables in sample 1 and 2, and R_1 and R_2 are sum of rank values in sample 1 and 2. The searched parameter U is the smaller one of U_1 and U_2 and is compared with the critical U value from table of critical values for the Mann-Whitney two sample statistics. When $U \leq U_k$ then the null hypothesis is rejected [67].

2.6.2-3 Correlation between the data sets

The Pearson correlation coefficient measures the strength of the linear relationship between two variables. It is assumed that the both variables sets (X, Y) are approximately normal distributed. The pearson coefficient r is within the values interval from -1 to 1, where -1 is a perfect negative (inverse) correlation, r = 1 a perfect positive correlation and 0 shows no correlation between the two data sets. The Pearson correlation coefficient is calculated as [66, 68]:

$$r_p = \frac{\sum XY - \frac{\sum X \sum Y}{n}}{\sqrt{\left(\sum X^2 - \frac{\left(\sum X\right)^2}{n}\right)\left(\sum Y^2 - \frac{\left(\sum Y\right)^2}{n}\right)}} \tag{49}$$

The Spearman rank correlation coefficient gives the strength of the associations between two variables (X, Y). It is a measure of monotone association that is used when the data are not normally distributed and so the calculation of Pearson correlation coefficient could be misleading. The Spearman may also be a better method to determine the strength of the relationship between the two variables when the relationship is non-linear. The Spearman rank correlation coefficient is defined by:

$$r_s = 1 - \frac{6\sum D^2}{n\left(n^2 - 1\right)} \tag{50}$$

where D is the difference in the statistical rank of corresponding variables.

The correlation is tested according to the null hypothesis: “There is no correlation between two samples”. The null hypothesis is rejected, when r_s is smaller than tabulated critical parameter. [67]

3 Experimental and evaluation of experimental data

3.1. Design and speciality of the lab scale e-beam coater at Fraunhofer IVV

The lab scale e-beam coater A260 E/B1 from Leybold AG (Applied films and Leybold optics GmbH today) was built as laboratory coating machine with the possibility of vacuum deposition of metal, semiconductors or metal oxide layers on one side of the web by roll to roll processes. The vacuum chamber of the coater is 550 mm high and 350 mm wide. Winding system and deposition room is divided by metal plates.

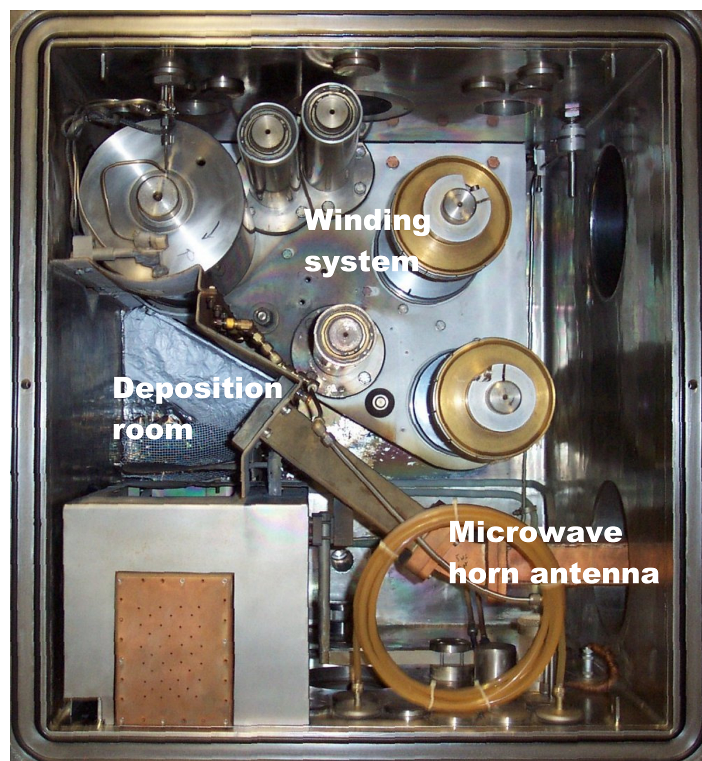

Fig. 24: Interior of the lab scale e-beam roll to roll coater used for the experiments

Microwave generator

The machine is equipped with a microwave generator for the applications of plasma pre-treatment and reactive evaporation such as the deposition of aluminium oxide from metalic aluminium in oxygen atmosphere activated by microwave plasma. The maximal disposable power of the microwave generator is 2,7 kW. For plasma pre-treatment a variety of gases can be used e.g. O_2, N_2, NH_3 or CO_2. The gas inlet is controlled by mass flow controllers MKS PR 3000.

Deposition system

The deposition system is based upon an electron beam evaporator ESV 14Q especially designed for the evaporation of metals and metal oxides for deposition of optical elements. The evaporator is equipped with a water-cooled rotary mount and crucible plates which can be exchanged separately.

Technical data of e-beam gun – ESV 14Q [71] :

Beam power output at 10 kV acceleration power .... 14 kW
Cathode voltage .... 7,5 V
Cathode current (max.)... 40 A
Main deflection with permanent magnet...................... 270°
Operating vacuum .... $<8.10^{-4}$ eV

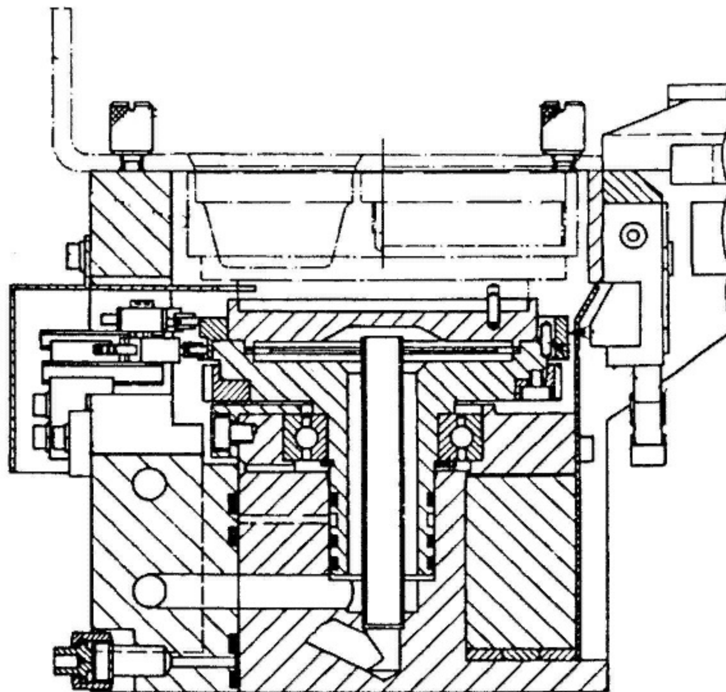

Fig. 25: E-beam gun with 270° deflection (type ESV 14/Q, Company Leybold) [72]

The crucible rotate continuously for uniform deposition of material, however the source material for deposition is again and again heated and evaporated. Therefore in the case of the evaporation of the mixture material such as mixture of silicon and silicon oxide in blocks, a crater like structure is created (see fig. 26) and accordingly the evaporation path for material is different in every point on the rotating target. That effect can bring the unstable deposition conditions in the deposition chamber. During

the coating process the deposition rate, which is the amount of the evaporated material in time, is monitored by Inficon deposition controller based on the oscillating quartz crystals.

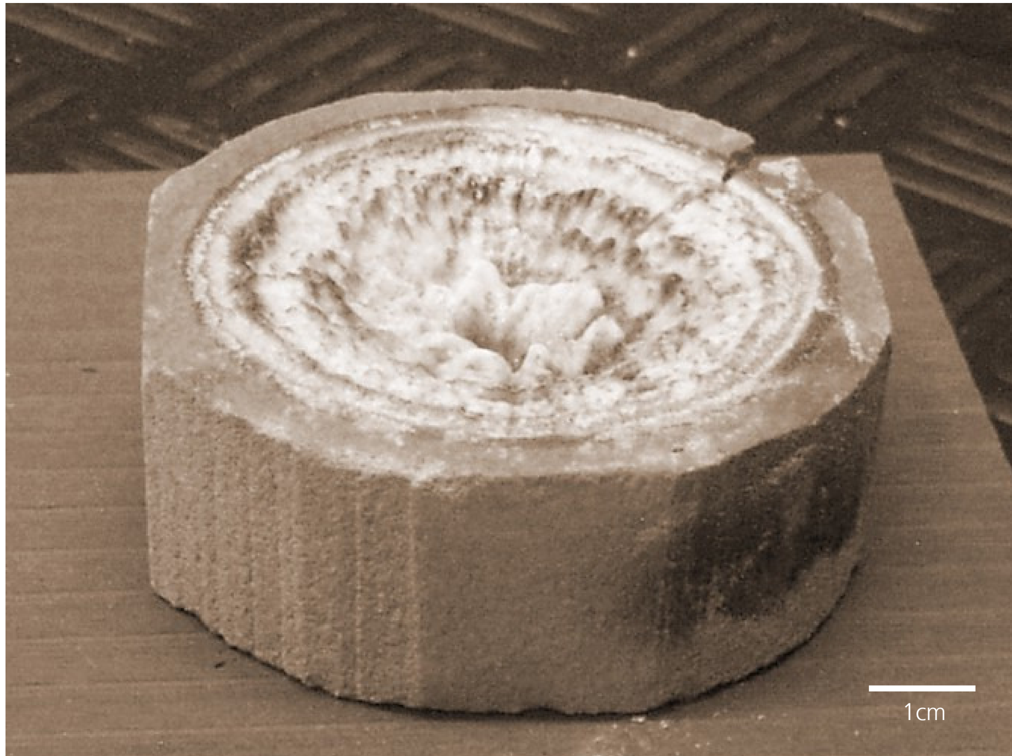

Fig. 26: A crater in the target of silicon oxide block material

Vacuum system

The vacuum system consists of the water cooled rootspump FM 12S and turbomolecular pump – Turbovac 1000 with pumping speed ~1000 l/s (N_2). The ultimate pressure of the turbomolecular pump is $<1.10^{-6}$ mbar ($>1.10^{-4}$ Pa) in 40 hours of pumping. The typical pressure during deposition process is 1.10^{-4} mbar (1.10^{-2} Pa). Three pressure measuring devices are installed in the system: two Termovac TM 210 S with the pressure measurement limit from 10^{3} mbar (10 Pa) down to 10^{-3} mbar (10^{-1} Pa) and Ionivac IM 210, which is available for the pressures in range from 1.10^{-3} mbar (10^{-1} Pa) down to 1.10^{-9} mbar (10^{-7} Pa). They are used for measurement of the pressure in the deposition chamber and they also support the automatic operation of the whole vacuum system.

Winding system

The winding system is adapted for the roll to roll transport of flexible materials such as polymer materials at speed up to 7 m/min. The system comprises six rollers with different diameters (see fig.27). First and second winder roller as well as coating roller are motor driven. Additional rollers are powerless. The web speed is controlled by the rotational speed of the coating roller and both winding directions are possible. The coating roller is water cooled up to -15 °C. The outer roller diameter of the windings rollers is typically 150 mm. Their web width is 280 mm and the length of deposited film can reach 1000 m.

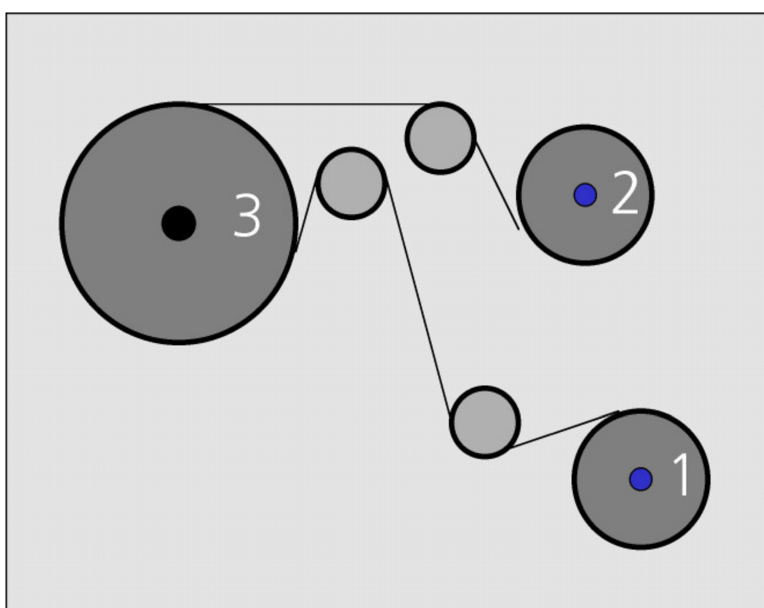

Fig. 27: Winding system of the lab scale e-beam roll to roll coater at Fraunhofer IVV
1, 2 – winding rollers and 3 – coating roller

3.2 In-situ FUV spectroscopic phase modulated ellipsometer

3.2.1 Modification of the lab e-beam coater for installation of the ellipsometer

For the installation of the ellipsometer into the lab e-beam the modification of the coater was needed. At firs the suitable place for the installation of the ellipsometer was discussed. The essential requirements for ellipsometer installation were: there has to be enough places for the all parts of the ellipsometer and the deposited layer has to be available for the measurement so that the measurement is performed preferably on the roller in order to prevent the vibrations during winding. The suitable

place was found on top of the coater, however it was necessary to perform the deposition process by reverse winding. This means that the substrate would not run in usual direction, but from the winding roller 2 to winding roller 1. The fig. 28 shows the schematic drawing of the coater interior and the position, where the ellipsometric measurements take place. In this case the place of analysis is located on the smooth roller under the existing central flange which was then modified for the installation of the ellipsometer (see fig 29 and 30).

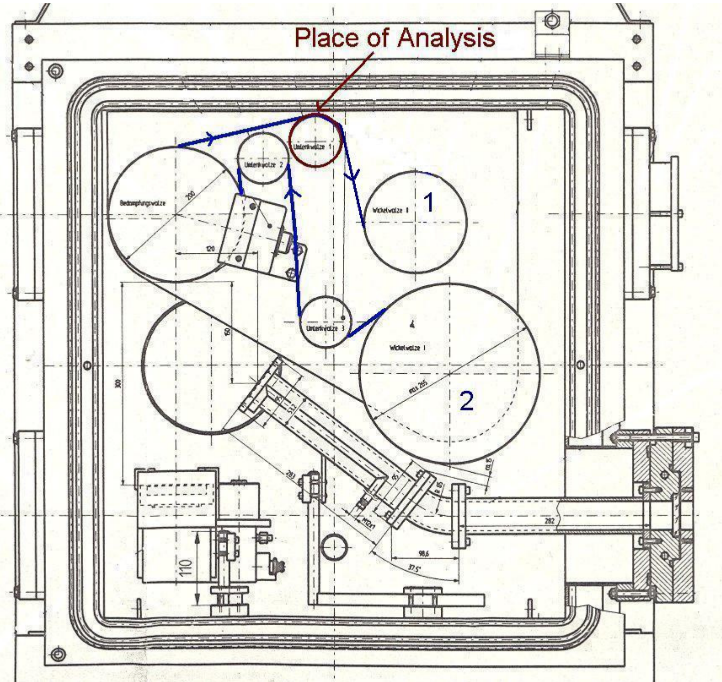

Fig. 28: the scheme of the coater interior with showing position of the ellipsometric analysis

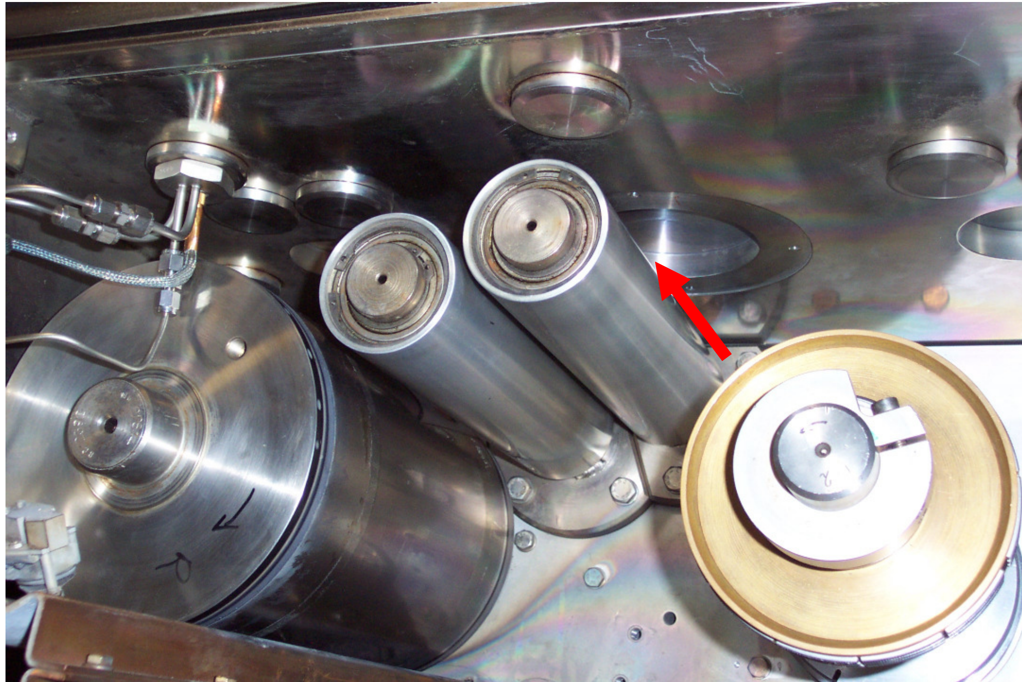

Fig. 29: Bottom view of the flange

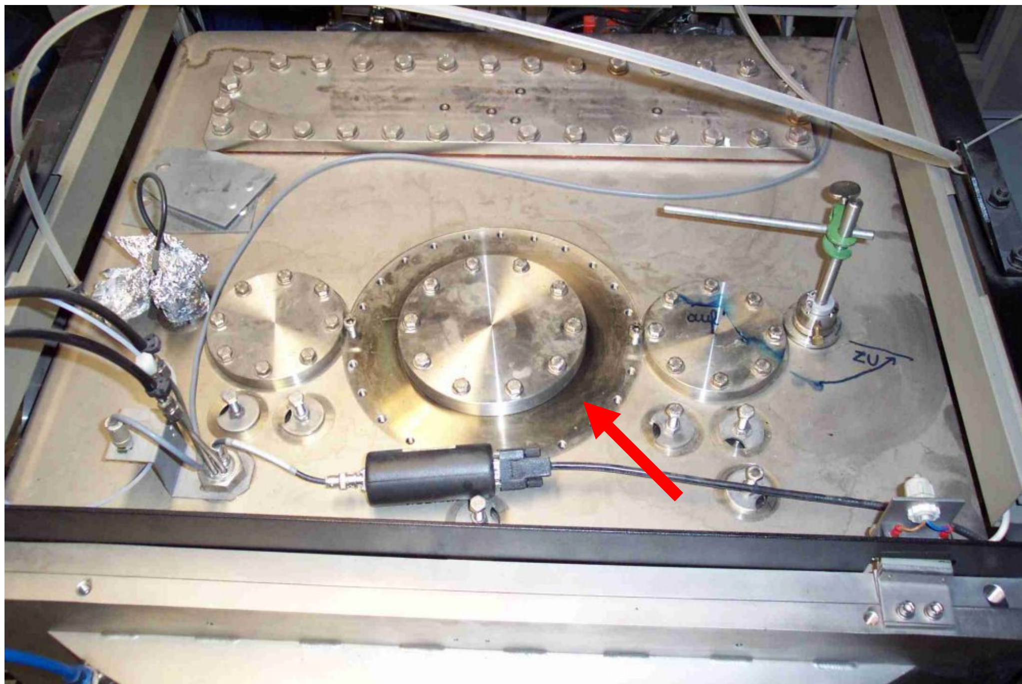

Fig. 30: Top view of the flange

There were two possibilities how to lead the light beam: either parallel or perpendicular to the roller axis. The both cases are shown in the figures 31 and 32. Finally it was decided that the least influences of the vibration will be when the beam will be reflected parallel to the roller axe. A new flange with two tubes was made for

the fixing of the ellipsometer components: analyser and modulator (see picture 33, 34). The angle between the tubes was 120° and the plane of light incidence was parallel to the axis of the smooth roller for better measurement stability. The tubes were closed with the standard flanges KF 40 for the fixing of the ellipsometer components.

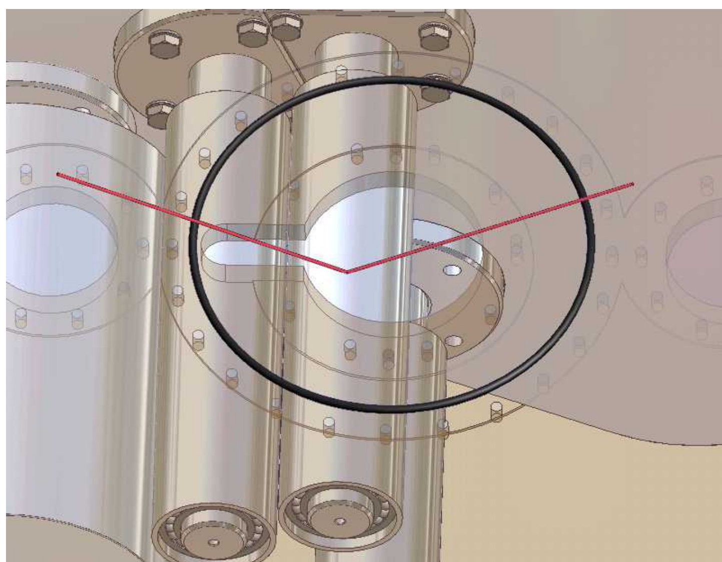

Fig. 31: Schematic view of the beam, which is led perpendicular to the roller axe.

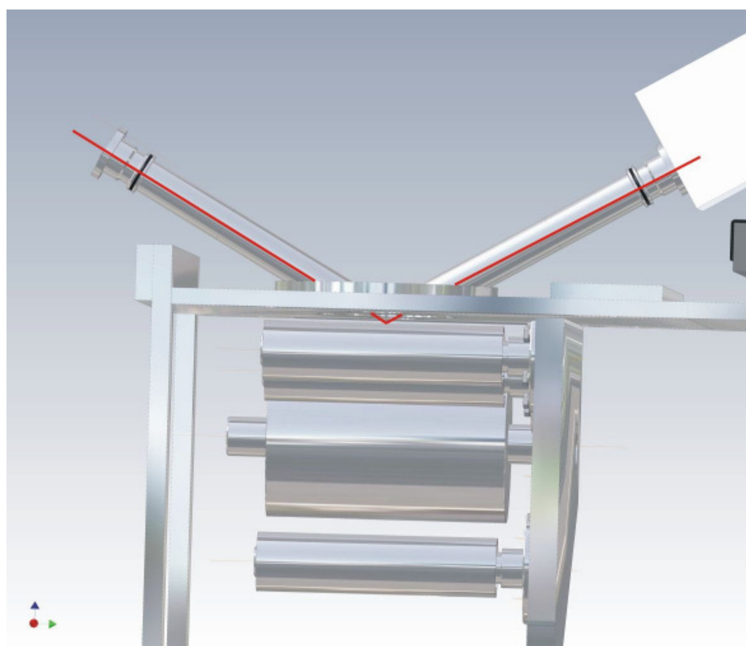

Fig. 32 Schematic drawing of the modified flange, in which the tubes will lead the beam parallel to the roller axe (side view).

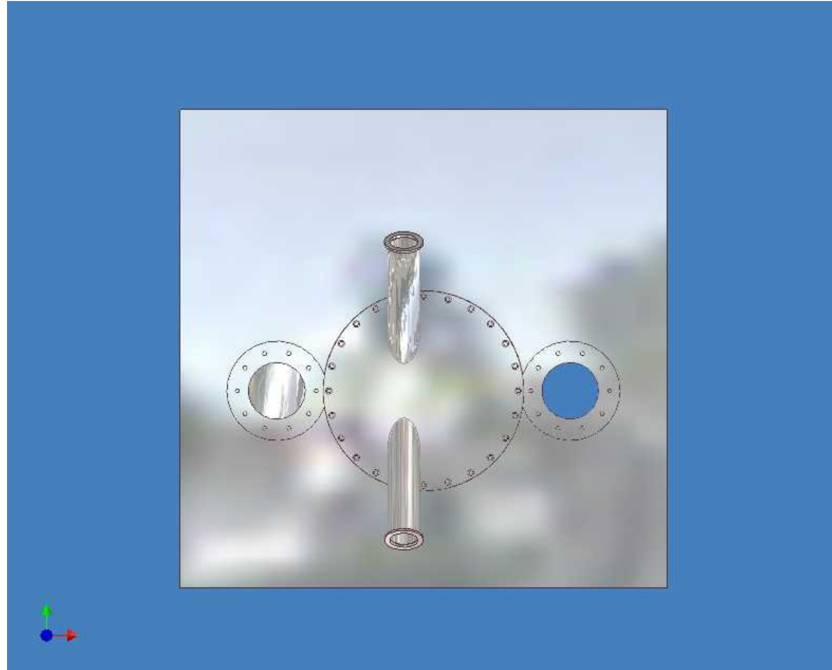

Fig. 33 Schematic drawing of the modified flange, in which the tubes will lead the beam parallel to the roller axe (top view)

3.2.2 Installation of the ellipsometer into the lab e-beam coater and spectra stability measurements

The in-situ FUV spectroscopic phase modulated ellipsometer fully installed into the lab-scale e-beam coater at Fraunhofer is shown in figure 34.

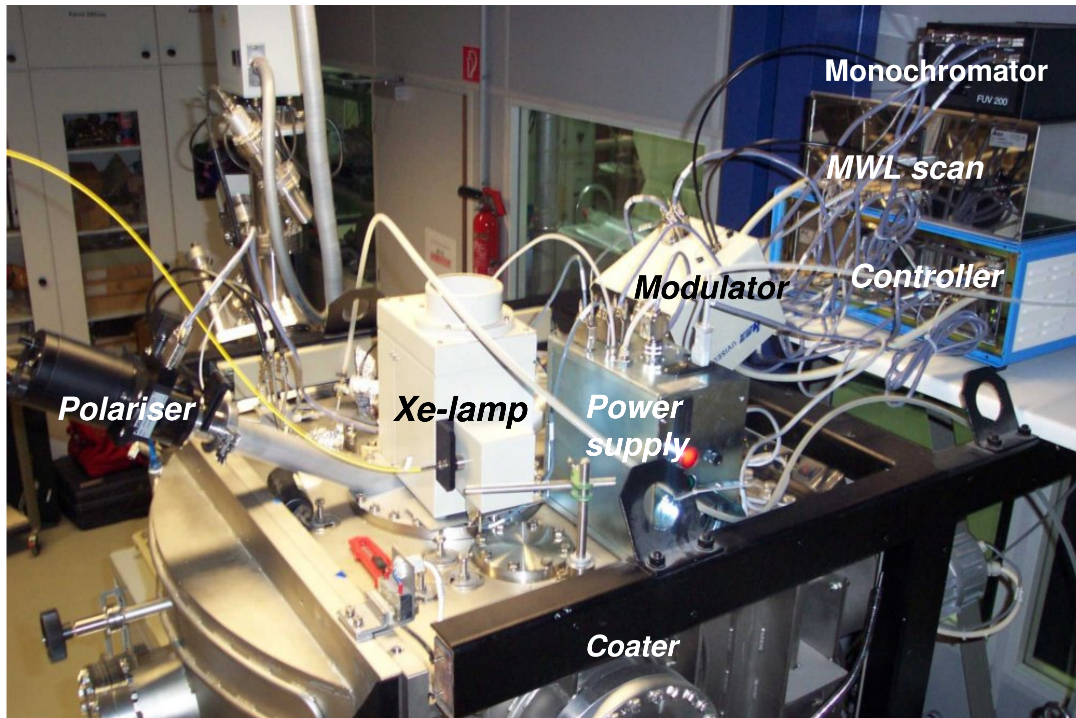

Fig. 34: In-situ FUV-VIS spectroscopic phase modulated ellipsometer installed onto the lab scale e-beam coater

The testing of the measurement stability and response rapidity was performed after installation of the ellipsometer. The signal was measured during winding in vacuum and in air, during pumping down as well as during venting of the deposition chamber. The ellipsometer delivered the stable signal in all 32 analysed energy channels under vacuum as well as under atmosphere. The interruptions of the signal were observed during pumping down likewise during venting the deposition chamber, probably due to vibration of the chamber components. This phenomenon was not critical for online control during deposition, which evidently take place under vacuum.
For the measurement the blank substrate Hostaphan® RD 23 µm was used. The taken spectra of the substrate during winding at different web speeds (up to 5 m/min) were stable and distinguished negligibly how it can be seen in the fig. 35.

The elliposometer give frequently the information about the sample, what should not be obtainable by standard sampling. The time needed for the acquisition (taking spectra) was about 4 seconds in the fixed modus and 16 seconds in automatic modus (*see chapter 3.2.3*).

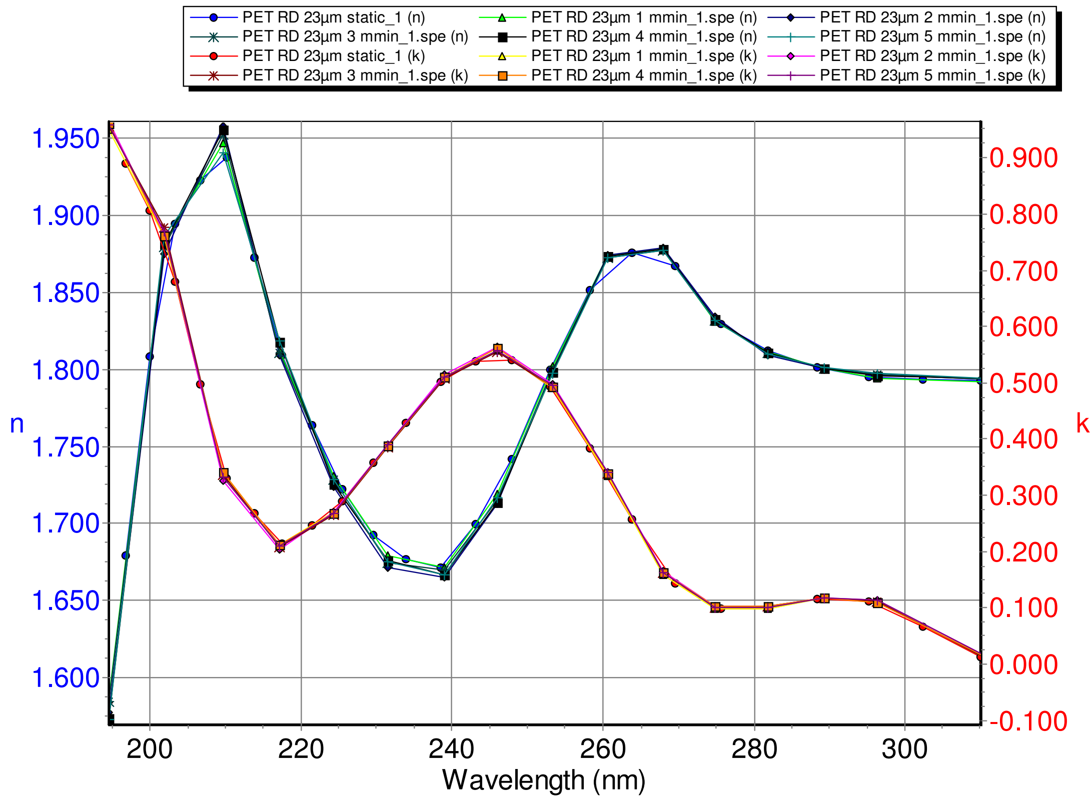

Fig. 35: Ellipsometric spectra of the substrate Hostaphan® RD 23 µm during winding at web speeds: 1, 2, 3, 4 and 5 m/min

3.2.3 Description of in-situ FUV spectroscopic phase-modulated ellipsometer

- Hardware

In-situ FUV spectroscopic phase modulated ellipsometer consist of excitation and detection heads for UV-VIS application, high-resolution monochromator, 32 - channel detection system especially developed for in-situ application during deposition process and controller. The excitation head comprises a fully stabilized 150 W Xenon arc source with spectral range from 190 to 2100 nm, an automatic micro-shutter for background subtraction, a mirror based optical coupling to the sample and a magnesium based polarizer mounted in an automatic positioner. In the detection head of the ellipsometer a thermally stabilised photo-elastic modulator with modulation frequency of 50 kHz is mounted in an automatic positioner with position accuracy of 0,05°. Besides the modulator the MgF_2 based polarizer is mounted in a fixed position with a position accuracy of less than 0.05° and extinction coefficient of less than 10^{-5}. For signal detection it was possible to choose from two types of equipments: monochromator and multiwavelength system. Because of the long time-

requirement for the data acquisition, the monochromator was not used. The multi-wavelength system with 32 high sensitivity photo-multipliers (PMT) allowed fast parallel data acquisition at 32 defined multiple wavelengths, which selected the ellipsometer spectral range (see table 5).

table 5: Photon energy of the used photo-channels in the multi-wavelength system

Photon energy channel	photon energy [eV]	wavelength [nm]
1	1,508	821,88
2	1,655	748,88
3	1,801	688,17
4	1,962	631,70
5	2,067	599,61
6	2,213	560,05
7	2,359	525,39
8	2,537	488,53
9	2,71	457,34
10	2,871	431,70
11	3,008	412,03
12	3,158	392,46
13	3,326	372,64
14	3,522	351,90
15	3,665	338,17
16	3,822	324,28
17	3,992	310,47
18	4,185	296,15
19	4,287	289,11
20	4,399	281,75
21	4,513	274,63
22	4,627	267,86
23	4,756	260,60
24	4,896	253,15
25	5,04	245,91
26	5,188	238,90
27	5,355	231,45
28	5,528	224,20
29	5,707	217,17
30	5,914	209,57
31	6,143	201,76
32	6,372	194,51

- Software

For the in-situ FUV spectroscopic phase modulated ellipsometer an operating software was supplied by the company Jobin Yvon Horiba. The measurement procedure consists of following steps:

1. Setting of the acquisition parameters by the operator and measurement of a reference substrate
2. Definition of the model (substrate/layer) and setting of the Tauc-Lorentz initial parameters
3. Integration of the model into an automatic procedure and start on-line measurement

Before the measurement the acquisition parameters such as integration time, spectral range; signal minimum and maximum in the case of the automatic modulated high voltage of the PMTs were set for the optimisation of the ellipsometer function. In performed experiments the fixed high voltage of the PMTs was used, because of the faster measurement. The values of the high voltage were set in virtue of the automatic measurement, so that the signal range was from 20 to 80 mV. The integration time, the time for measurement of a spectrum point, was 200 ms. It was the shortest time, which was possible to use according to the signal background.

The first measurement was always off-line measurement of the blank substrate (reference substrate) to get the real values of the complex refractive index $\tilde{n}$ = n + ki in whole spectrum of the light wavelengths. The measured spectrum was then applied into the building of the model. The model consists of a substrate and a simple layer, which is defined by Tauc-Lorentz fomula. This simplified model was used because of the need of fast acquisition and modulation during a real deposition process.

The properties of the deposited layer were calculated by Tauc-Lorentz [64] experimental formula wherein the initial values as well as the limitation have to be defined before fitting procedure proceed. Typical initial values for a simple layers are given in table 6.

Table 6: Initial values of Tauc-Lorentz model used for the layers of the different chemical composition. There, C is used as a formal broadening constant arising from inhomogeneities of the film material.

Layer like	E_g [eV]	ε^{∞}	A	E_0 [eV]	C [eV]
SiO	2,5	1	50	6	7
SiO_x	3	1	70	8	9
SiO_2	3	1	90	11	11
AlO_x	6,5	1	90	9	10

After defining the initial values for the Tauc-Lorentz model, the estimated layer thickness as well as its acceptable maximum and minimum values were set. The spectral range, in which the measured spectrum have been modelled, was defined from 3,5 to 6 eV.

The fitting procedure was started in automatic mode, in which the spectra were frequently taken during deposition and immediately fitted according to pre-defined model. All results coming from the fitting procedure of the measured spectra were saved in a special file, so that it was also possible to inspect a whole measurement and the fitting procedure, when deposition (and on-line measurement) was completed.

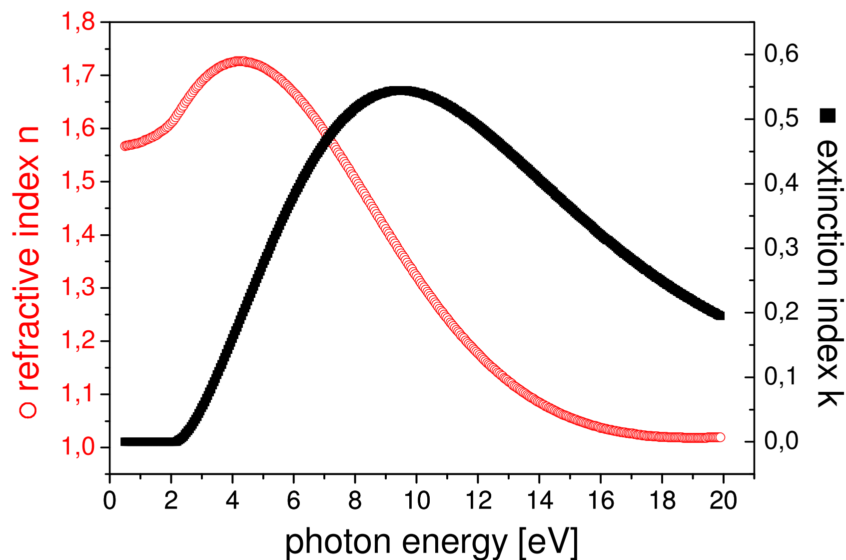

Fig. 35: Typical spectrum of silicon oxide material calculated from Tauc-Lorentz formula after the fitting procedure: E_g = 2,2, $\varepsilon_{inf.}$ = 1, A = 50, E_0 = 9, C = 11

3.3 Sample preparation

3.3.1 Preparation of silicon oxide samples

The silicon oxide samples, which were prepared with different stoichiometry and a different layer thicknesses by the lab e-beam coater at Fraunhofer institute and online analysed by ellipsometry are presented in table 7.

Table 7: Prepared samples according to used source material for deposition.

<table>
<tr><th>Sample</th><th>substrate</th><th>material</th></tr>
<tr><td>PET 12 SiO 160103</td><td>®Hostaphan RNK 12 µm</td><td>SiO</td></tr>
<tr><td>PET 23 SiO 290103</td><td>®Hostaphan RD 23 µm</td><td>SiO</td></tr>
<tr><td>PET 12 SiO_x 210103</td><td>®Hostaphan RNK 12 µm</td><td rowspan="6">Si + SiO_2</td></tr>
<tr><td>PET 23 SiO_x 220103</td><td rowspan="5">®Hostaphan RD 23 µm</td></tr>
<tr><td>PET 23 SiO_x 250203</td></tr>
<tr><td>PET 23 SiO_x 040303</td></tr>
<tr><td>PET 23 SiO_x 220104</td></tr>
<tr><td>PET 23 SiO_x 210104</td></tr>
<tr><td>PET 23 SiO_2 020204</td><td>®Hostaphan RD 23 µm</td><td>SiO_2</td></tr>
</table>

Silicon oxide layers were deposited on biaxially oriented coextruded polyethylene-terephtalate (PET) film with the functional surface, having very smooth surface (Mitsubishi Polyester films) – ®Hostaphan RD 23 µm as well as on standard polyethylene terephtalate film ®Hostaphan RNK 12 µm.

For the preparation of the samples three different source materials were used:

- silicon monoxide (SiO)
- silicon dioxide (SiO_2)
- silicon oxide mixture

The industrial material of Si + SiO_2 mixture was prepared by pressing of the both material into the block with a macroscopic composition, which results that elementary ratio (O:Si) x greater than 1,8 in the deposited layer. This material is specially prepared for the industrial production of the company Alcan packaging services.

Table 8: Source material used for deposition:

material	supplier	Granule size [mm]	Purity [%]
SiO	Umicore	3 – 6	99,9
SiO_x	Alcan	Block material	-
SiO_2	Umicore	1 – 4	99,9

3.3.2 Preparation of aluminium oxide samples

For preparation of the aluminium oxide samples the aluminium oxide (Al_2O_3) granulate with a purity of 99,99 % and granule size of 2,5 – 6,0 mm was taken as the source material. An aluminium oxide layer was deposited on the functional surface of the biaxialy oriented polyethylene terephtalate substrate Hostaphan® RD 23 µm.

Table 9: Prepared samples according to the used source material for deposition.

Sample	**substrate**	**material**
PET 23 AlO_x 240103	®Hostaphan RD 23 µm	Al_2O_3
PET 23 AlO_x 060503	®Hostaphan RD 23 µm	Al_2O_3
PET 23 AlO_x 170603	®Hostaphan RD 23 µm	Al_2O_3

3.3.3 Deposition parameters

The deposition experiments were performed in the lab scale e-beam coater described above at a pressure of approximately 1.10^{-4} mbar (1.10^{-2} Pa). The deposition rate was monitored using oscillatory quartz (the layer with a thickness of about 100 nm is deposited when the deposition rate is 33 nm/s and web speed is 0,05 m/s). Used PET substrates were 280 mm and 200 mm wide. For the narrower film two correcting shields were built in the housing of the deposition room to avoid coating of the drum. The samples were produced either in stationary process or the deposition parameters namely web speed or e-beam power were changed stepwise.

At first the pre-heating phase was performed by heating up the target material while the shutter placed over the deposition material was kept closed. The pre-heating phase lasts at least for 5 min, which are needed for cleaning the material surface from adsorbed impurities and for melting of the granulates to obtain a compact crust. The pre-heating power of the e-beam is lower than the deposition power. Typically

the pre-heating power used for silicon dioxide SiO_2 was 0,4 kW whereas during deposition it was 1 – 1,2 kW. For the pre-heating and deposition of aluminium oxide Al_2O_3 layers the power of 0,75 kW and 1,9 – 2,2 kW were applied, respectively. The evaporation of silicon monoxide and silicon oxide SiO_x requires less energy. The pre-heating was performed at beam power output of 0,22 kW and the deposition at 0,6 kW (at high voltage 10 kV). Detailed the coating conditions during deposition are given in tables 10 and 11.

Table 10: Coating conditions during deposition of silicon oxide layers

sample	**web speed [m/s]**	**e- beam power during preheating [kW]**	**e-beam power output [kW]**	**deposition rate [nm/s]**
PET 23 SiO 290103-2	0,033	0,2	0,45	10 – 15
PET 23 SiO 290103-3	0,05			15 – 20
PET 23 SiO 290103-1	0,017			10 – 15
PET 23 SiO 290103-3	0,05			25 – 30
PET 23 SiO 290103-4	0,067			30 – 40
PET 23 SiO 290103-4	0,067			50 – 60
PET 23 SiO 290103-5	0,083			50 – 60
PET 12 SiO 160103-5	0,083	0,22	0,6	30 – 40
PET 12 SiO 160103-2	0,033			40 – 50
PET 12 SiO_x 210103-4	0,067	0,2	0,7	15 – 20
PET 12 SiO_x 210103-3	0,05			15 – 20
PET 12 SiO_x 210103-2	0,033			15 – 20
PET 12 SiO_x 210103-1	0,017			15 – 20
PET 23 SiO_x 220103-5	0,083	0,25	0,6	30 – 40
PET 23 SiO_x 220103-4	0,067			30 – 40
PET 23 SiO_x 220103-3	0,05			30 – 40
PET 23 SiO_x 220103-2	0,033			30 – 40
PET 23 SiO_x 220103-1	0,017			20 – 30
PET 23 SiO_x 210104-2	0,033	0,2	0,6	15 – 20
PET 23 SiO_x 210104-3	0,05			30 – 40
PET 23 SiO_x 210104-5	0,083			40 – 50
PET 23 SiO_x 040303	0,05	0,25	0,6	30 – 40
PET 23 SiO_x 250203	0,05	0,25	0,6	30 – 40
PET 23 SiO_x 220104	0,05	0,20	0,6	30 – 40
PET 23 SiO_2 020204-5	0,083	0,40	0,8	30 – 40
PET 23 SiO_2 020204-3	0,05		0,8	30 – 40
PET 23 SiO_2 020204-3	0,05		1,2	40 – 50
PET 23 SiO_2 020204-2	0,033		1,2	40 – 50

Table 11: Coating conditions during deposition of aluminium oxide layers

sample	web speed [m/s]	e- beam power during preheating [kW]	e-beam power output [kW]	deposition rate [nm/s]
PET 23 AlO_x 240103-1	0,017	0,75	2,2	10 – 13
PET 23 AlO_x 240103-2	0,033		2,2	10 – 13
PET 23 AlO_x 240103-3	0,05		2,2	10 – 13
PET 23 AlO_x 240103-4	0,067		2,2	10 – 13
PET 23 AlO_x 240103-5	0,083	0,75	2,2	10 – 13
PET 23 AlO_x 060503	0,017	1	2,2	10 – 13
PET 23 AlO_x 170603	0,01	0,7	1,4	8 – 20
			2,1	
			1,8	
			2,2	
			1,5	

The samples PET 23 SiO_x 220104, PET 23 SiO_x 250203 and PET 23 SiO_x 040303, PET 23 AlO_x 060503 were prepared by deposition process, in which the web speed as well as the e-beam power had been kept constant. Therefore also the thickness of the deposited layer and their nature is expected to be constant too.

The sample PET 23 SiO_x 220104 was deposited in a special manner: in the beginning of the deposition the shutter over the deposition material was closed, so no layer was deposited, afterwards it was suddenly opened and again closed after a while. The reaction (speed and flexibility) of the ellipsometer was tested.

The layer thickness variation of the silicon oxide and aluminium oxide samples: PET 23 AlO_x 240103, PET 12 SiO 160103, PET 12 SiO_x 210103, PET 23 SiO_x 220103, PET 23 SiO 290103, PET 23 SiO_x 210104 and PET 23 SiO_2 020204 were performed by changing of the web speed stepwise while e-beam power was kept constant.

For the sample of PET 23 AlO_x 170603 the variation of the deposited layer thickness was achieved atypically by changing of the e-beam power within the range of 1,4 to 2,2 kW so that the power of e-beam increases step by step. It was estimated that the layer thickness followed the changing of the emission flow, which change continuously according to the heating of the source material.

3.4 Polyethylene terephtalate films

For preparation of the samples, two types of the polyethylene terephtalate films were used: Hostaphan® RD 23 µm and Hostaphan® RNK 12 µm. The structure of these both films are shown in figures 36 and 38.

Hostaphan® RD 23 µm is a biaxially oriented coextruded film especially designed for deposition processes. This film has a different topography on both surfaces, while one side has a standard structure with antiblock particles and rough surface; its functional surface side has extremely regular surface structure with very low roughness (see figure 37).

Hostaphan® RNK 12 µm is a highly transparent, biaxially oriented, coextruded film with both side having a standard topography. The mechanical, thermal and barrier properties as well as surface characterisation of the films, which were used for deposition, are given in table 12. It can be seen that the both surface have very good mechanical and thermal stability. The roughness (root mean square) of the functional surface of Hostaphan® RD 23 µm is three times lower than of the standard surface of Hostaphan® RNK 12 µm.

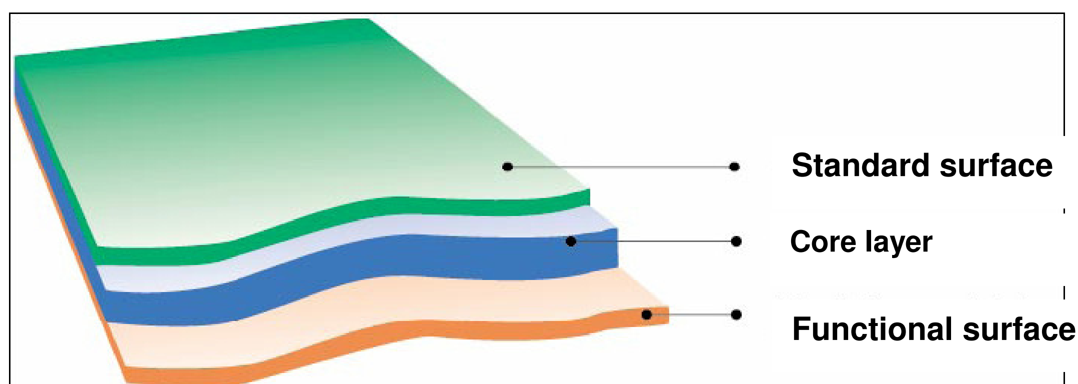

Fig. 36: Layer structure of Hostaphan® RD 23 µm [53]

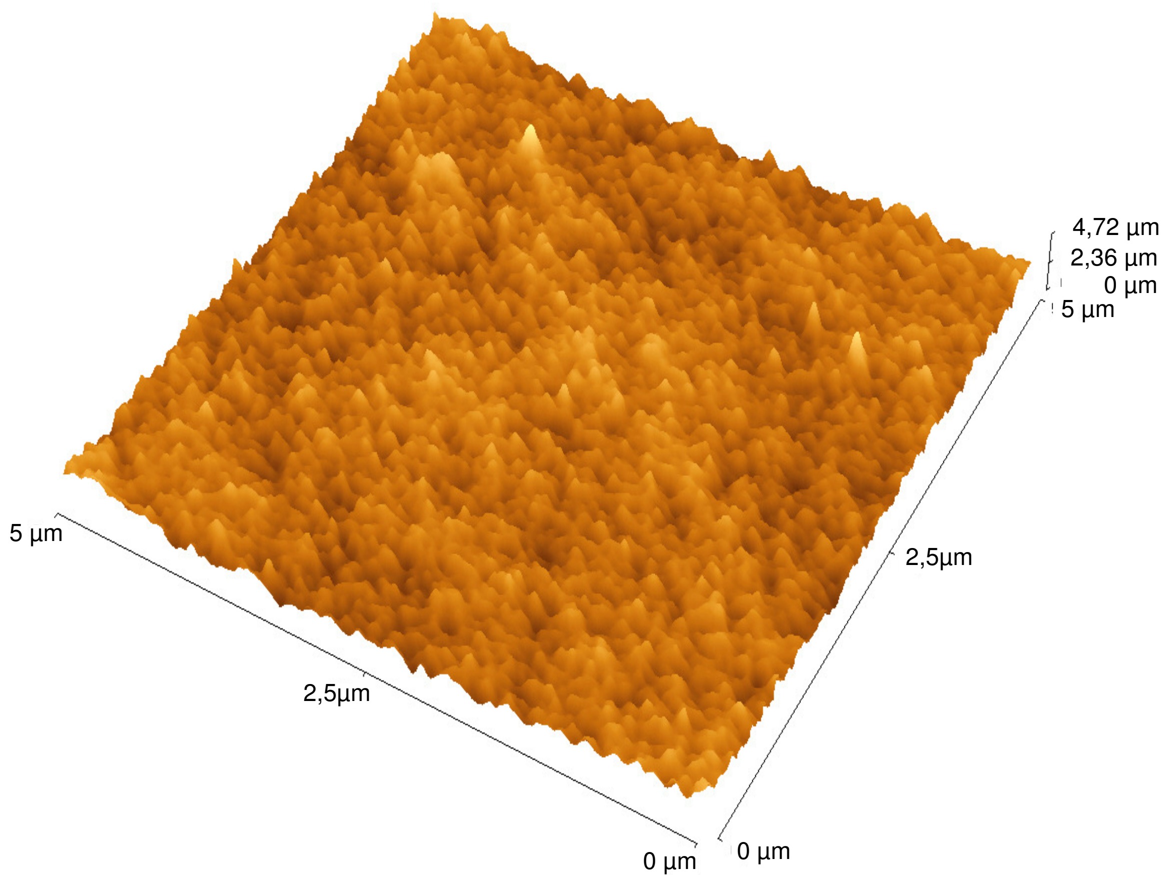

Fig. 37: Functional surface of the Hostaphan® RD 23 µm measured by atomic force microscopy (AFM)

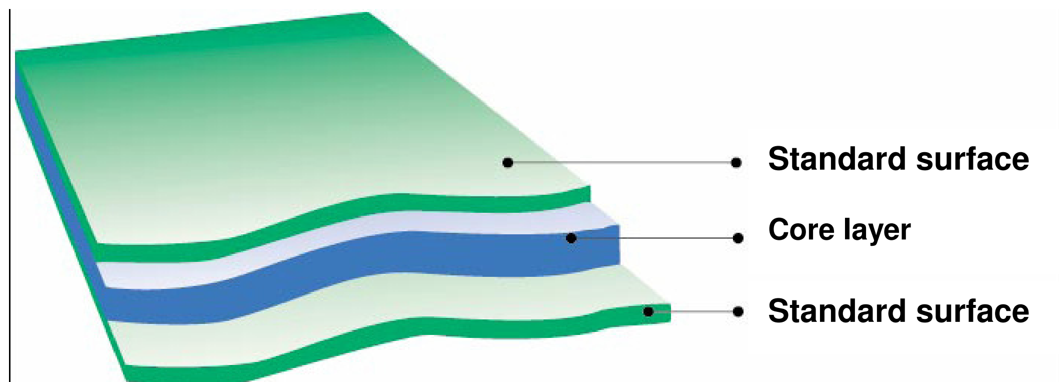

Fig. 38: Layer structure of Hostaphan® RNK 12 µm [73]

Table 12: Typical properties of used films [53, 73]:

Property	Units	Test conditions	Orientation	Hostaphan® RD 23 µm	Hostaphan® RNK 12 µm
Mechanical					
Tensile strength	N/mm²	Test speed 100 %/min.; 23 °C, 50 % r.h.	Machine direction	250	250
			Transverse direction	270	260
Elongation at break	%	Test speed 100 %/min.; 23 °C, 50 % r.h.	Machine direction	120	120
			Transverse direction	105	105
Tensile stress required to cause 5% elongation	N/mm²	Test speed 100 %/min.; 23 °C, 50 % r.h.	Machine direction	110	110
			Transverse direction	100	100
Thermal					
Shrinkage	%	150 °C 15 min.	Machine direction	1,3	1,4
			Transverse direction	0,1	0,2
Surface					
Coefficient of friction	-	DIN 53375	Standard surface	0,4	0,4
			Functional surface	0,4	-
Mean roughness	nm	AFM 1µm²	Standard surface	3	3
			Functional surface	1	-
Barrier properties (transmission rate)					
Oxygen	cm³/(m² day bar)	23 °C, 50% r.h	-	210	110
Water vapour	g/(m² day)	23 °C, 85% r.h	-	30	16
Nitrogen	cm³/(m² day bar)	23 °C, 0% r.h	-	67	35
Carbon dioxidw	cm³/(m² day bar)	23 °C, 0% r.h	-	960	500

Fig. 39 Antiblock particle on the substrate of Hostaphan ® 23 µm RD

3.5 Analysis of the properties and surfaces of the deposited layers

3.5.1 Scanning electron microscopy

A Hitachi S 4000 scanning electron microscope (see fig. 40) operating at an accelerating voltage of 20 keV and an emission flow of 10 µA was used for the measurement of the geometric thickness of the deposited film. The pieces of the samples were cut from the position, where online ellipsometric measurement was previously performed. Each sample piece was mechanically stressed so that the inorganic layer was broken and layer thickness could be measured at the layer edges. After that the sample pieces were sputtered by gold to be conductive. The gold sputtering was performed on the sputtering equipment Hummer JR under Argon (14 kPa) in the high voltage 5 kV and for 4 minutes. The layer thicknesses of inorganic and Au layer were measured on the taken pictures using the integrated software.

Fig. 40: Scanning electron microscope Hitachi S 4000

The participation of the gold layer to the measured layer thickness was tested. In the fig. 41 the measured layer thickness in comparison to the time of the gold sputtering is shown. It can be seen that there is a linear dependence between the time of the sputtering and measured layer thickness with the slope of the regression line being 2,6 nm/min. Therefore the deposited layers were sputtered for 4 min and the layer of gold was calculated to be about 10 nm. Sputtering time less than 4 min is not recommended, because then the view of the layer is blurred.

The layers with the different layer thicknesses namely 200 nm, 100 nm and 50 nm are shown in the figures 42, 43, 44. There is clearly to see the edge of the broken layer, where the thickness measurement take place.

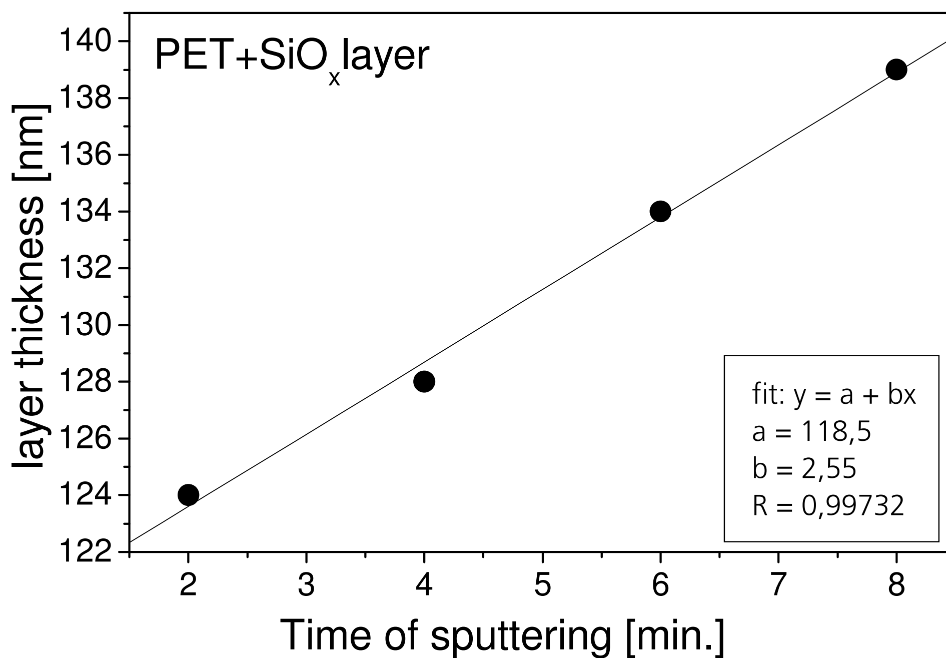

Fig. 41: The (inorganic layer + gold) thickness in comparison to the time of the sputtering of the gold measured for on industrial sample of PET / SiO_x

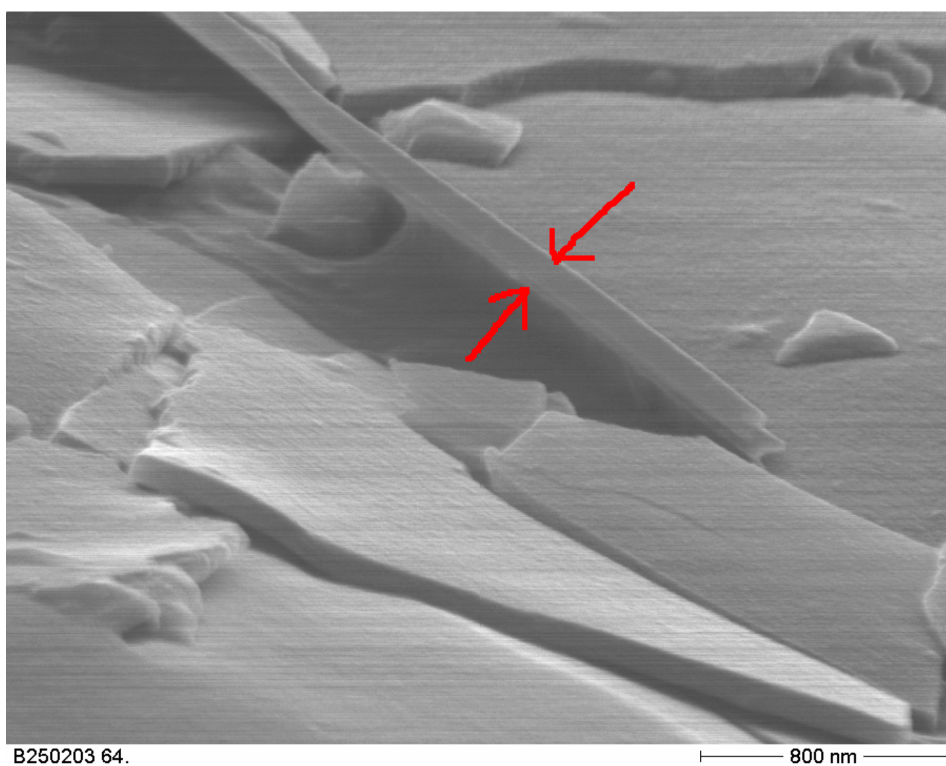

Fig. 42: Layer thickness measurement of the deposited silicon oxide layer using SEM

Layer thickness ~ 100 nm

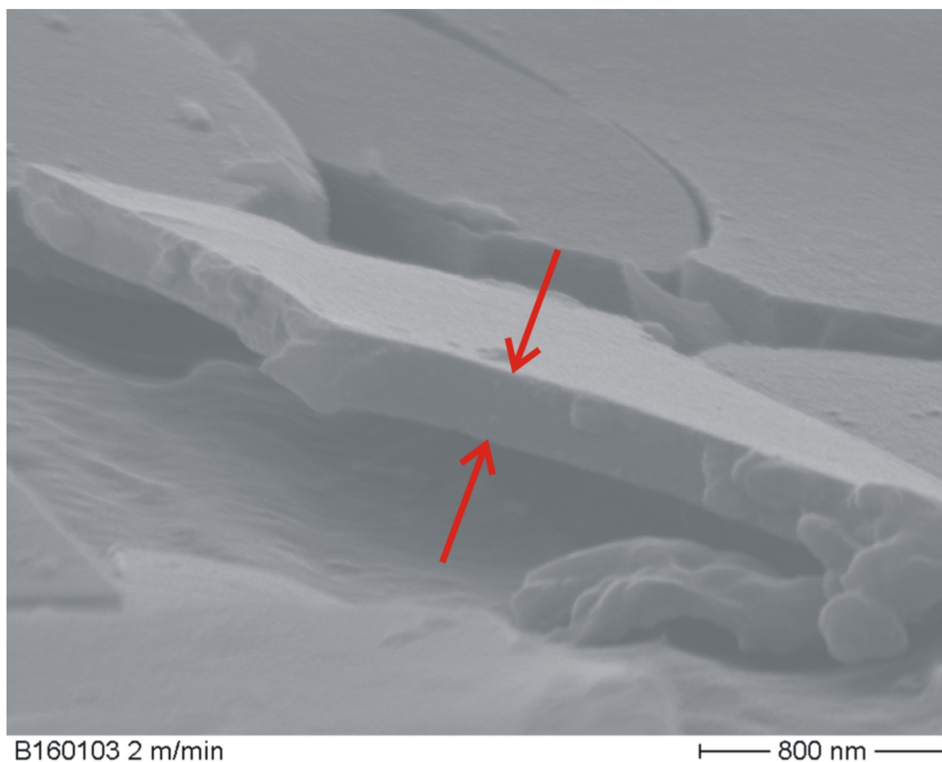

Fig. 43: Layer thickness measurement of the deposited silicon oxide layer using SEM

Layer thickness ~ 200 nm

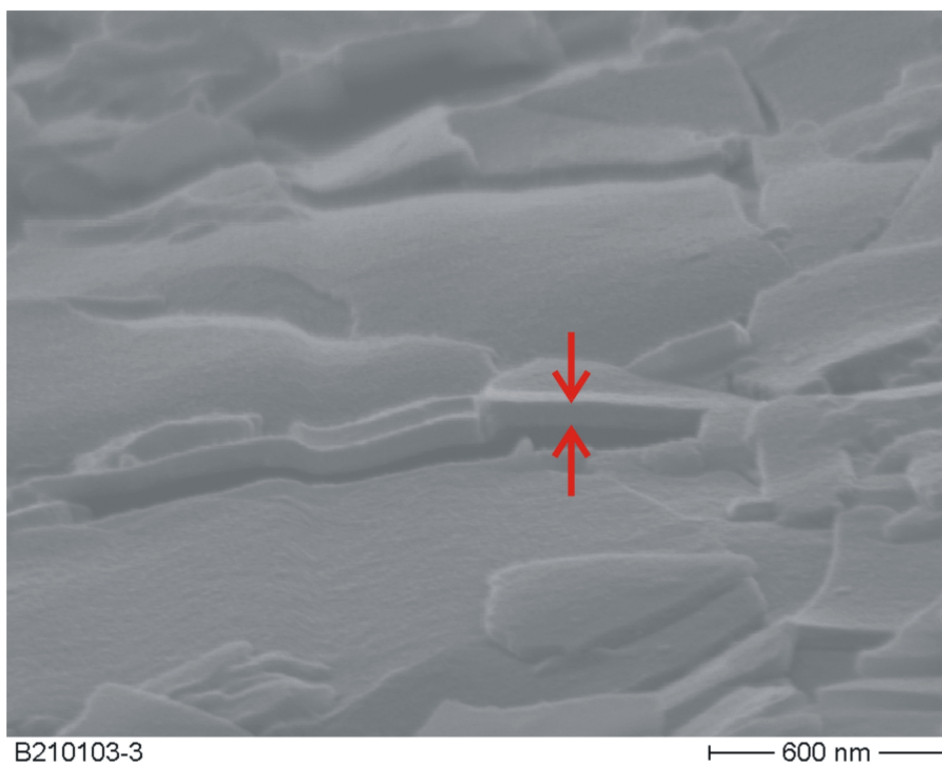

Fig. 44: Layer thickness measurement of the deposited silicon oxide layer using SEM

Layer thickness ~ 50 nm

3.5.2 X-ray photoelectron spectroscopic analysis (XPS)

The elementary ratio x, which is the ratio of Al to O or Si to O, was measured by XPS method. XPS measurements were carried out using a VG ESCA 3 Mk II electron spectrometer with a base pressure of 10^{-8} Pa. For sample sputtering an AG 2 cold cathode argon ion gun operated at 6 keV was used. Al Kα radiation (1486.6 eV) was employed for spectra excitation. Electrons were energy analyzed using a hemispherical capacitor analyzer operating at a constant pass energy of 50 eV. The energy scale of the spectrometer was calibrated with Au $4f_{7/2}$ binding energy fixed at 84.0 eV. The spectra of Si (2p), O (1s) and C (1s) electrons were measured. [74] .

The penetration depth of the XPS is usually limited to 7 nm, so that after each single analysis, the already measured layer has to be removed. The measurement of the whole thickness needs several steps until the substrate surface of the PET appears. On fig. 45 the variation of the layer composition through its depth is shown. At first the concentration of carbon is a little higher because of the carbon coming from the absorbed CO_2. After that the carbon concentration decreases to zero and only pure silicon oxide layer is analysed. Then the interlayer appears, wherein the concentration of carbon atoms increases and the concentration of silicon atoms decreases continuously. Finally, the measurement reaches the pure substrate, where the concentration of silicon is zero whereas the concentration of carbon takes a maximum. Hydrogen (coming from the absorbed water) cannot be detected via XPS. In the case of samples deposited in thickness variation, the XPS analysis was performed on several positions along the web and the chemical composition of the samples with different layer thickness was compared. The stoichiometric ratio x of the silicon oxide layers were determined as the ratio of the oxygen atomic concentration to the atomic concentration of the silicon in the layer.

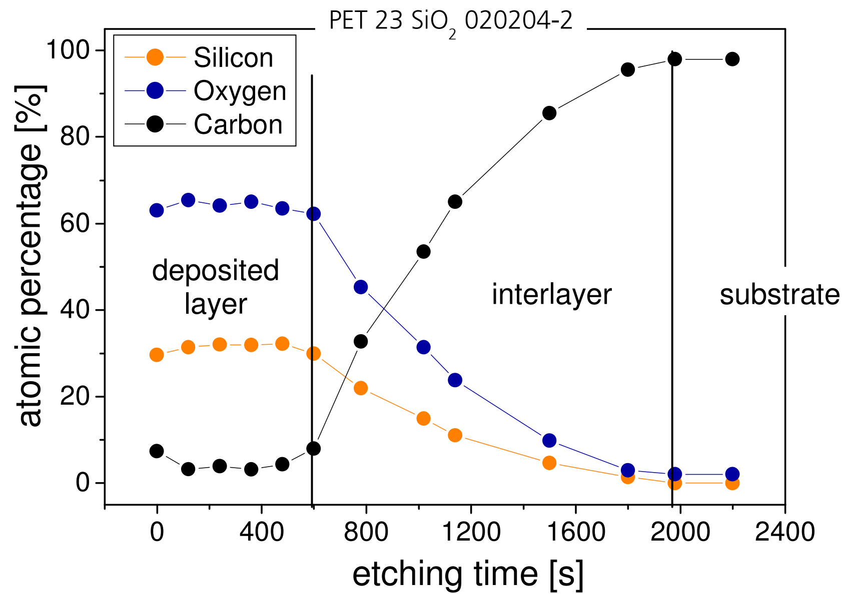

Fig. 45: Example of the atomic concentrations of the silicon, oxygen and carbon measured in the depth profile of the sample: silicon dioxide layer deposited on the PET substrate (PET 23 SiO_2 020204) [74]

3.5.3 Permeation measurements

- Oxygen transmission rate (OTR)

The transmission rates of oxygen through the samples were measured according to DIN 53 380-3. The sample is placed in the chamber so that the chamber is separated by the sample in two parts: upper room and lower room (see figure 46). The oxygen is led in the upper room at 23 °C and 50 % relative humidity. The oxygen permeats through the sample to the lower room and it is drawn by a carrier gas which contains 95 % nitrogen and 5 % hydrogen to the electro-sensor. The electrolytic sensor consists of a graphite cathode and a porous cadmium anode. The oxygen atom reacts with the cadmium atoms on the anode surface resulting in four electrons. The amount of the incoming oxygen atoms is linearly proportional to the created charge. This type of measurement is suitable for polymeric films, polymeric films coated with barrier layers and other flat packagings. The limit of this measurement is in the range 0,05 –1000 $cm^3/(m^2$ d bar).

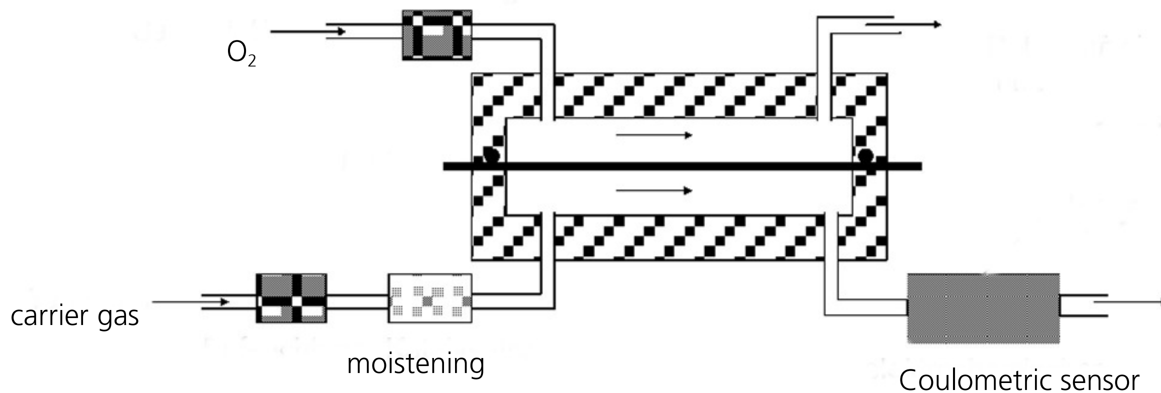

Fig. 46: Scheme of the OTR measurement

- Water vapour transmission rate (WVTR)

The water vapour transmission rate measurement system is similar to the measurement of oxygen transmission rate (see figure 47) and follows DIN 53 122-2. There is a frit with a defined humidity (water solution of sulphuric acid) that control the humidity in the upper room of the chamber. The water vapour is transmited through the sample and it is led into the electrolyse cell by a dried carrier gas. The electrolyse cell consists of two thin Pt wires that are covered with phosphor pent oxide. When the phophor pentoxide reacts with the water vapour, the products of this reaction afterwards electrolysis are oxygen and hydrogen:

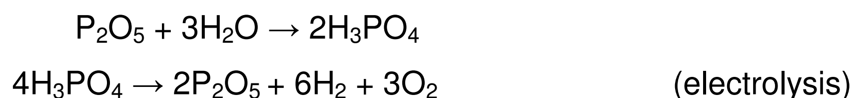

$$P_2O_5 + 3H_2O \rightarrow 2H_3PO_4$$

$$4H_3PO_4 \rightarrow 2P_2O_5 + 6H_2 + 3O_2 \qquad \text{(electrolysis)}$$

The needed charge for this reaction is linearly dependent on the incoming water vapour. This method is available for polymeric films, coated films, papers and other flat packaging materials. The measurement is limited from 0,01 g/(m² d) to approximately 5 g/(m² d).

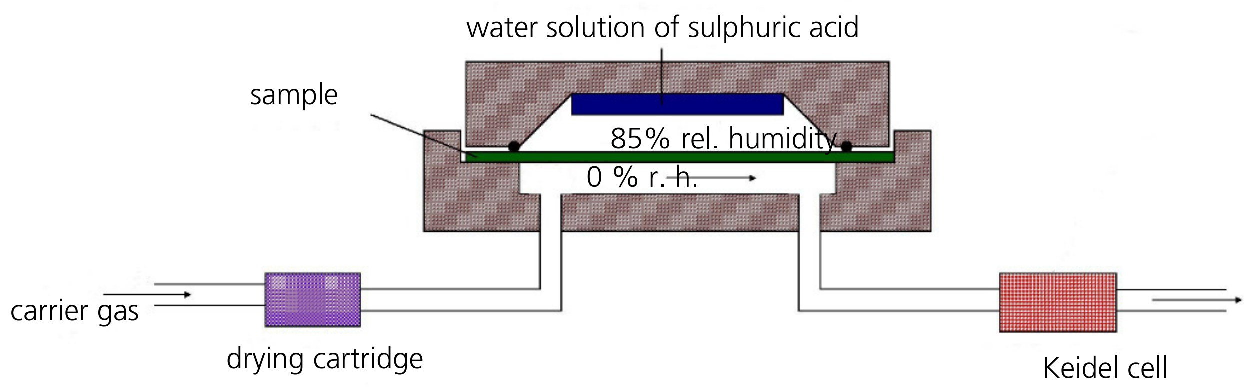

Fig. 47: Scheme of the WVTR measurement

4. Results

4.1 Basic and functional properties of deposited films

After depositions the produced samples were analysed by convenient offline methods for determination of the real layer properties such as chemical composition, layer quality (barrier properties) and layer thickness, which are later compared to the values coming from the on-line measurements by spectroscopic ellipsometry.

4.1.1 Chemical composition

The chemical composition of the deposited samples was measured by X-ray photoelectron spectroscopy (XPS). The silicon oxide layers consist predominantly of atoms of oxygen and silicon and in the case of the aluminium oxide layers of oxygen and aluminium atoms. For many samples a small amount of carbon was identified on the outer surface, which come probably from the absorption of the carbon dioxide on the sample surface. The stoichiometry of the layer was calculated from the ratio of atomic concentration of silicon to oxygen *(see chapter 3.5.2).*

The samples were analysed on several positions along the deposited web. The results show that there are only negligible differences in stoichiometry of the samples deposited during the same process and it seems the layer thickness has no critical influence on the chemical composition of the silicon oxide layers. Figs. 48 and 49 illustrate one of the measured samples, namely PET 23 SiO_2 020204.

The elementary ratios x calculated by XPS measurements are plotted in figure 50. On the x-axis can be found the elementary ratio x on account of the used deposition material and on the y-axis x from XPS analysis. The chemical composition of the layers determined by XPS is generally higher than expected from the composition of the source material. During deposition the evaporated material decomposes into Si, SiO and O_2 particles in the case of silicon oxide and into Al, AlO and O_2 in the case of aluminium oxide and mix with the rest gas in deposition chamber. The rest gas comprises mostly water vapour and gases from the outer atmosphere (*see chapter 2.2.1*). The mixing of oxygen from the residual gas into the built layer leads to a layer with a higher oxygen content than expected from the chemical composition of the

source material itself. The more oxygen and water vapour the residual gas contains the more oxygen is built into the layer.

The silicon oxide layers (PET 12 SiO 160103 and PET 23 SiO 290103) deposited from a pure silicon monoxide granulate comprise 1,3 – 1,4 times more amount of oxygen than silicon monoxide. In the case of the sample deposited from the source material with a higher part of oxygen such as the sample PET 23 SiO_x 040303 the amount of oxygen is between a factor of 1,8 – 2 times the amount of the silicon in the layer. The described effect of incorporation of additional oxygen into the layer affects the layers deposited from the source material with less oxygen amount more.

Aluminium oxide layers were deposited from a pure Al_2O_3 material. The effect of the incorporation of the water vapour into the coating material take also place in the case of the aluminium oxide layers. The measured elementary ratio x (O:Al) was 1,7 – 1,8 instead of 1,5 expected for Al_2O_3.

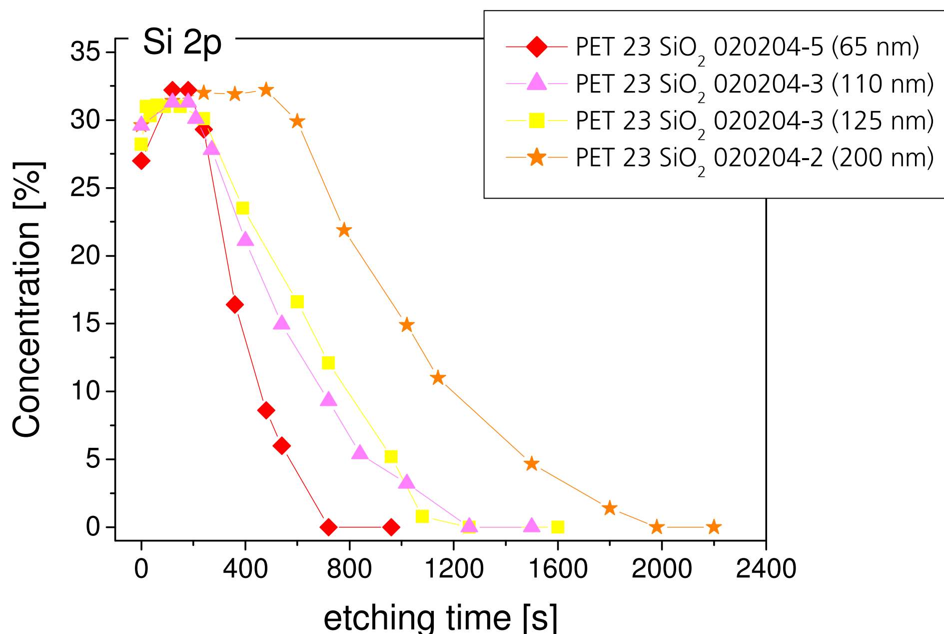

Fig. 48: Amount of the silicon in the silicon dioxide layer of the sample PET 23 SiO_2 020204 deposited on the PET substrate and analysed by XPS [74].

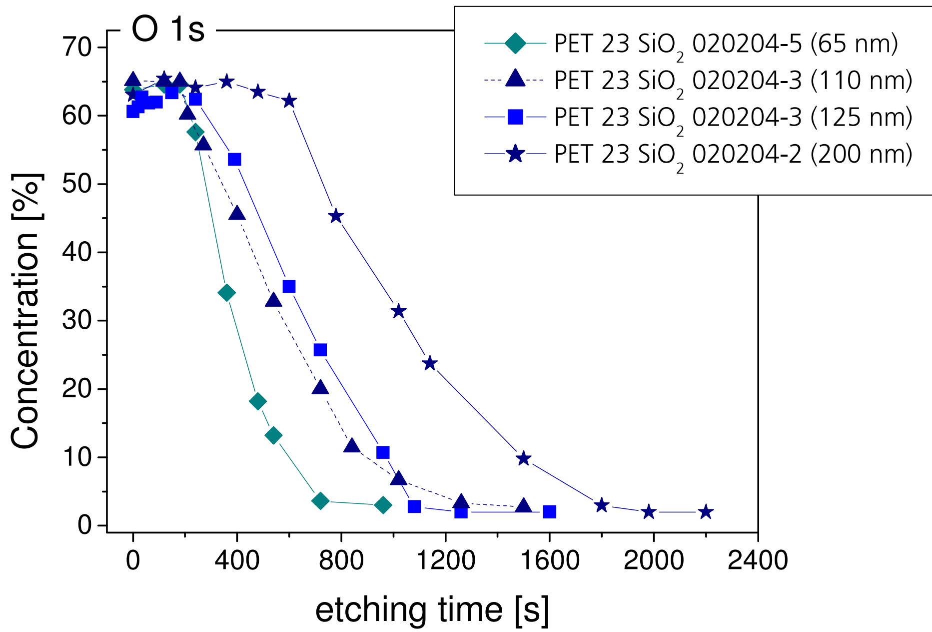

Fig. 49: Amount of the oxygen in the silicon dioxide layer of the sample PET 23 SiO_2 020204 deposited on the PET substrate and analysed by XPS [74]

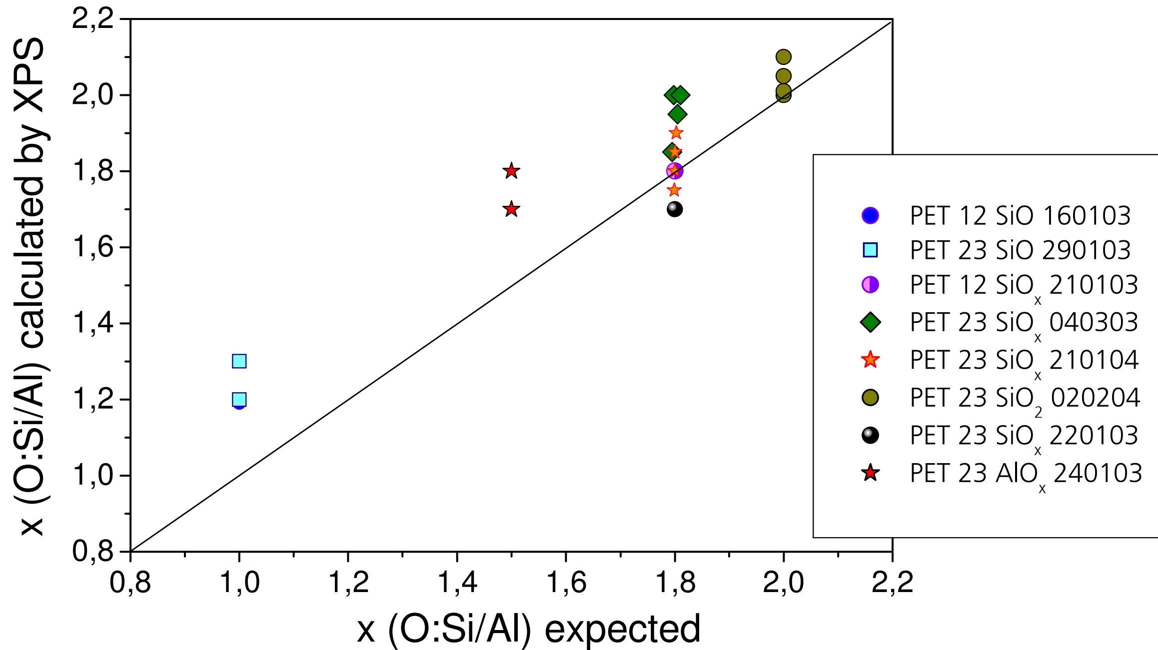

Fig. 50: Comparison of the measured stoichiometric ratio contra expected stoichiometric ratio according to the source material used for deposition.

4.1.2 Layer thickness

The layer thicknesses of the samples were measured by using scanning electron microscopy on the several different places along the web. The results are shown in tables 12 and 13.

Table 12: Average of layer thickness values of silcon oxide layers

Sample	substrate	Source material	Layer thickness [nm]
PET 23 SiO 290103-2	®Hostaphan RD 23 µm	SiO	43
PET 23 SiO 290103-3			52
PET 23 SiO 290103-1			80
PET 23 SiO 290103-3			86
PET 23 SiO 290103-4			92
PET 23 SiO 290103-4			135
PET 23 SiO 290103-5			140
PET 12 SiO 160103-5	®Hostaphan RNK 12 µm		108
PET 12 SiO 160103-2			212
PET 12 SiO_x 210103-4	®Hostaphan RNK 12 µm	SiO_x	43
PET 12 SiO_x 210103-3			47
PET 12 SiO_x 210103-2			80
PET 12 SiO_x 210103-1			180
PET 23 SiO_x 210104-2	®Hostaphan RD 23 µm		40
PET 23 SiO_x 220103-5			77
PET 23 SiO_x 210104-3			85
PET 23 SiO_x 040303			90
PET 23 SiO_x 250203			95
PET 23 SiO_x 220104			95
PET 23 SiO_x 220103-3			100
PET 23 SiO_x 220103-4			105
PET 23 SiO_x 210104-5			110
PET 23 SiO_x 220103-1			130
PET 23 SiO_2 020204-5	®Hostaphan RD 23 µm	SiO_2	65
PET 23 SiO_2 020204-3			110
PET 23 SiO_2 020204-3			125
PET 23 SiO_2 020204-2			200

Table 13: Average of layer thickness values of aluminium oxide layers

Sample	**substrate**	**material**	**layer thickness [nm]**
PET 23 AlO_x 240103-1	®Hostaphan RD 23 µm	Al_2O_3	70
PET 23 AlO_x 240103-2			45
PET 23 AlO_x 240103-3			30
PET 23 AlO_x 240103-4			30
PET 23 AlO_x 240103-5			20
PET 23 AlO_x 060503			105
PET 23 AlO_x 170603			Systematically varied

4.1.3 Barrier properties

The samples produced by deposition of silicon oxide as well as the samples with aluminium oxide show improvement of the barrier properties. In figure 51 it can be seen that the oxygen transmission rate of the samples vary within the interval 2,1 – 3,8 cm^3/m^2.day bar for the samples coated with silicon oxide. Only the oxygen transmission rate for the sample PET 23 AlO_x 060503 is a little higher→ 5,5 cm^3/m^2.day bar. In the special case, when the silicon dioxide was used as source material for deposition, the produced layers (sample PET 23 SiO_2 020204) had poor barrier properties, which can be expected due to the used source material *(see chapter 3.3.1).* The best barrier properties, which were achieved, are WVTR = 0,632 g/m^2.day in the case of sample 210104-2 and OTR = 2,2 $cm^3/(m^2$ day bar) for PET 23 SiO_x 210103-4 (see figures 51 and 52).

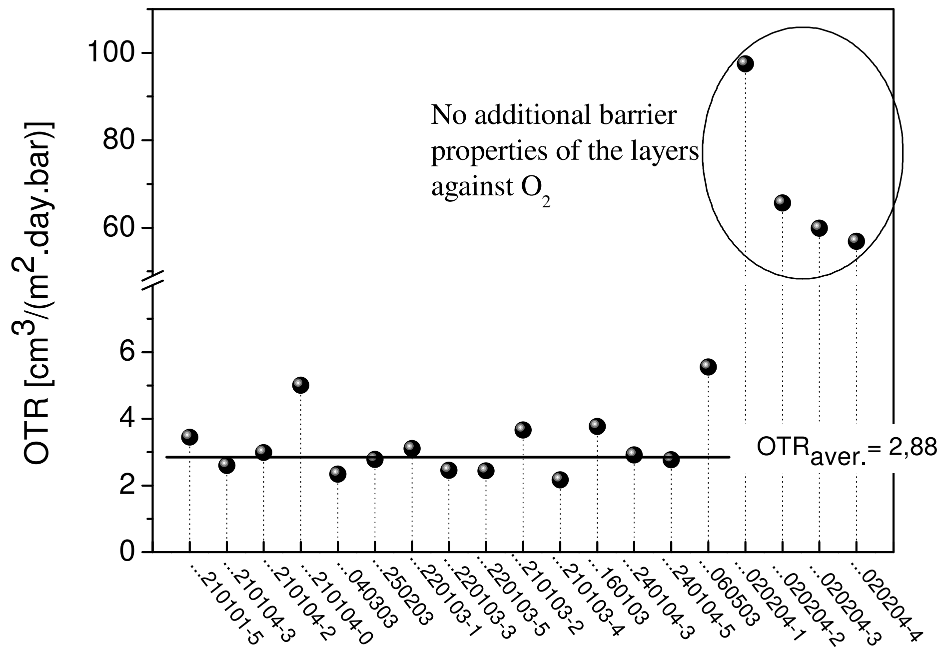

Fig. 51: Oxygen transmission rate of the produced samples at 23°C and 50 % relative humidity.

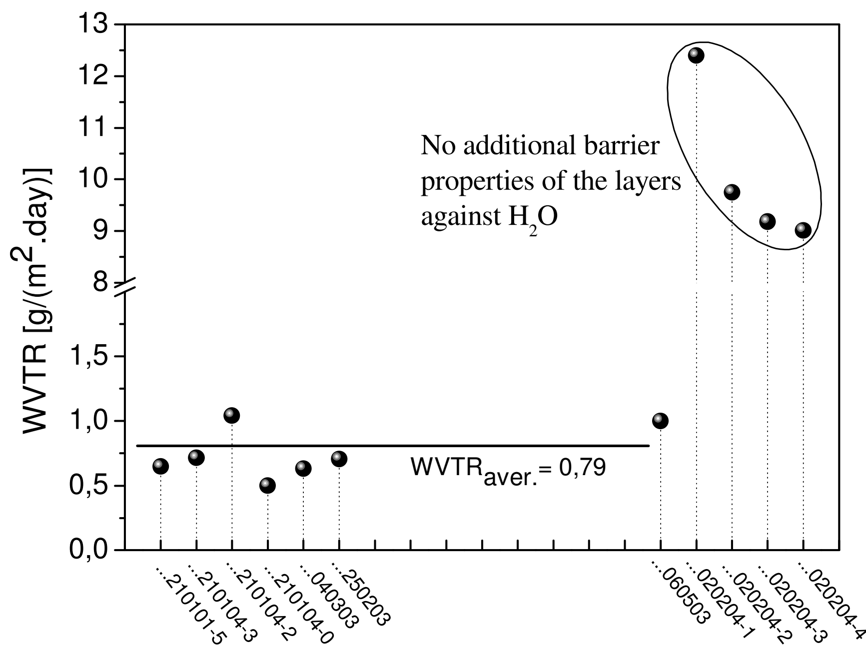

Fig. 52: Water vapour transmission rate of the produced samples at 23°C and gradient of the rel. humidity 85 → 0 %

4.1.4 Surface analysis

The optical properties of the layer are strongly affected by layer porosity. Therefore the porosity control of deposited inorganic layers was required for better understanding of the measured values coming from ellipsometric measurements. Since the porosity of the layer influences also the barrier properties, in the next the permeation rates are taken for quantification of the layer quality. However the permeation of the gases and vapours take place predominately through the defects existing in the inorganic coating. These defects typically occur on the antiblock particles as well as due to already existing impurities on the surface, which was deposited *(see chapter 2.1.4).* Therefore the barrier properties were measured simultaneously in parallel to the performed surface analysis, so that the additional effect of the higher number of the defect can be evaluated.

The analysed samples PET 23 SiO_x 250203, PET 23 SiO_x 210104, PET 23 SiO_x 220104 and PET 23 SiO_2 020204, PET 23 AlO_x 060503 have a smooth surface with a few number of the antiblock particles or other possible defect places (see figs: 53, 54). On the basis of those measurements it can be assumed that an increased permeation through the inorganic layers is caused by porosity of the layer itself.

In the case of the samples PET 23 SiO_x 040303 and PET 23 AlO_x 060503 there are many irregularities on the deposited surface, what impacted probably also the integrity of the layers and so also their barrier properties. Therefore for these samples it is not possible to directly correlate the barrier properties to their layer porosity (see figures: 55, 56).

Fig. 53: SEM picture of the surface of the sample PET 23 SiO_2 020204 (2000x)

Fig. 54: SEM picture of the surface of the sample PET 23 SiO_2 210104 (2000x)

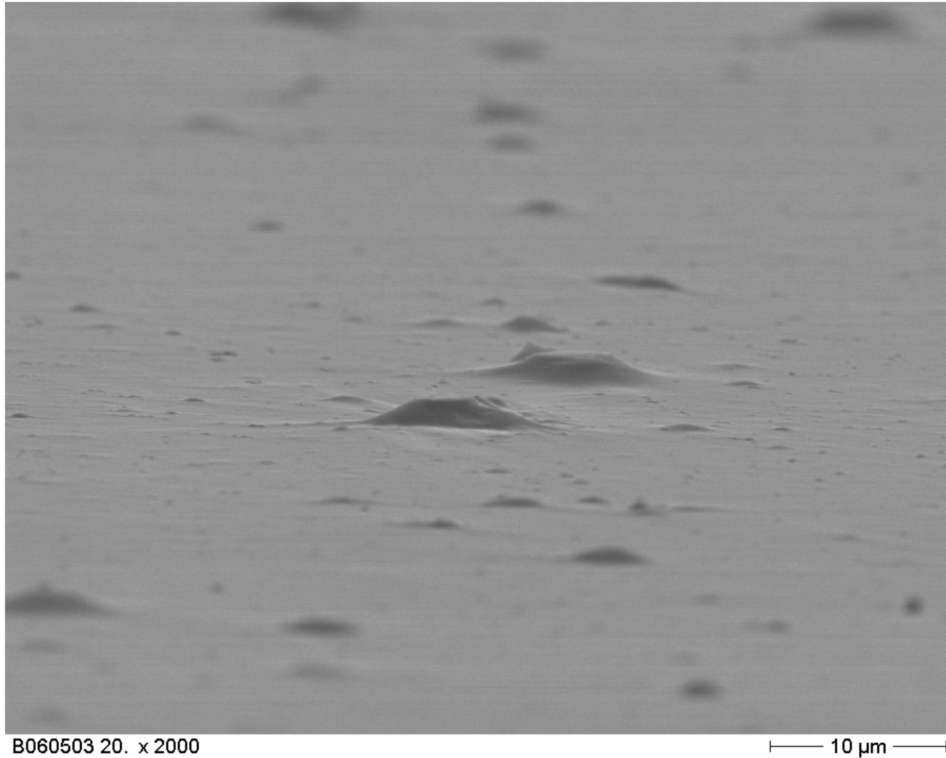

Fig. 55: SEM picture of the surface of the sample PET 23 AlO_x 060503 (2000x)

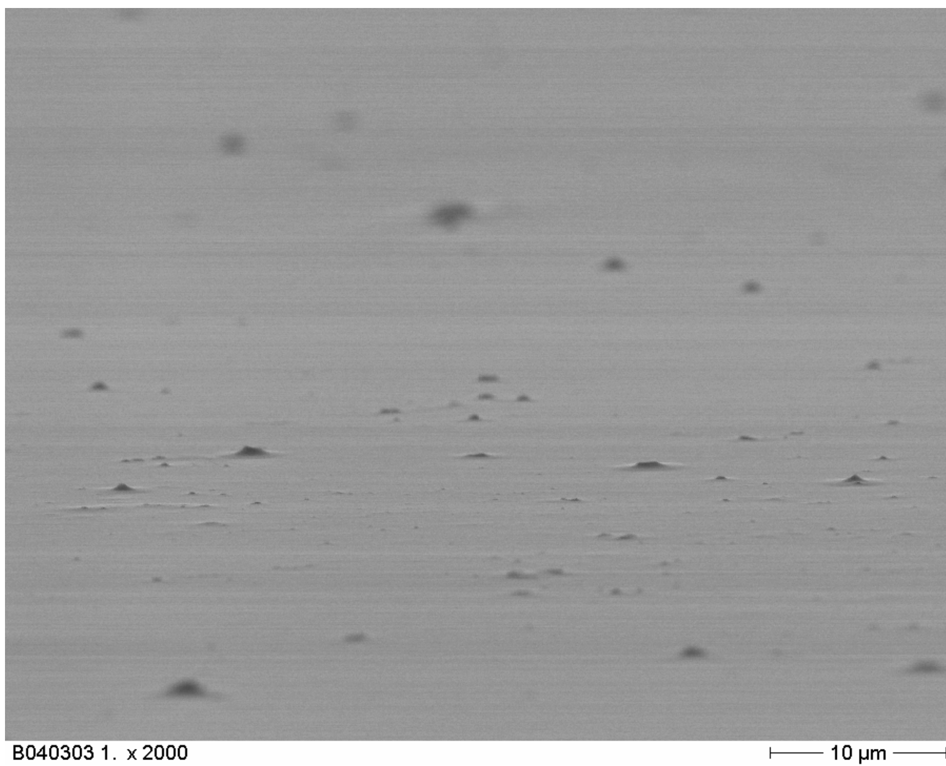

Fig. 56: SEM picture of the surface of the sample PET 23 SiO_x 040303 (2000x)

4.1.5 Relation between the barrier properties, layer thickness and the elementary ratio x

It was reported that the barrier properties of inorganic layers such as silicon oxide layers and aluminium oxide layers depend on their layer thickness as well as on their chemical composition. The chemical composition, namely elementary ratio (O:Si) is considered to be very important for good barrier properties *(see chapter 2.3.1).* This phenomenon was not observed (see fig. 57 and fig. 58) neither in the case of the layers produced by lab-coater nor by industrial coaters. It can be seen that the quality of the layer only slightly depends on the chemical composition of the layer itself. It can be said that the layers with very high amount of oxygen are frequently produced today without an impact on their barrier properties.

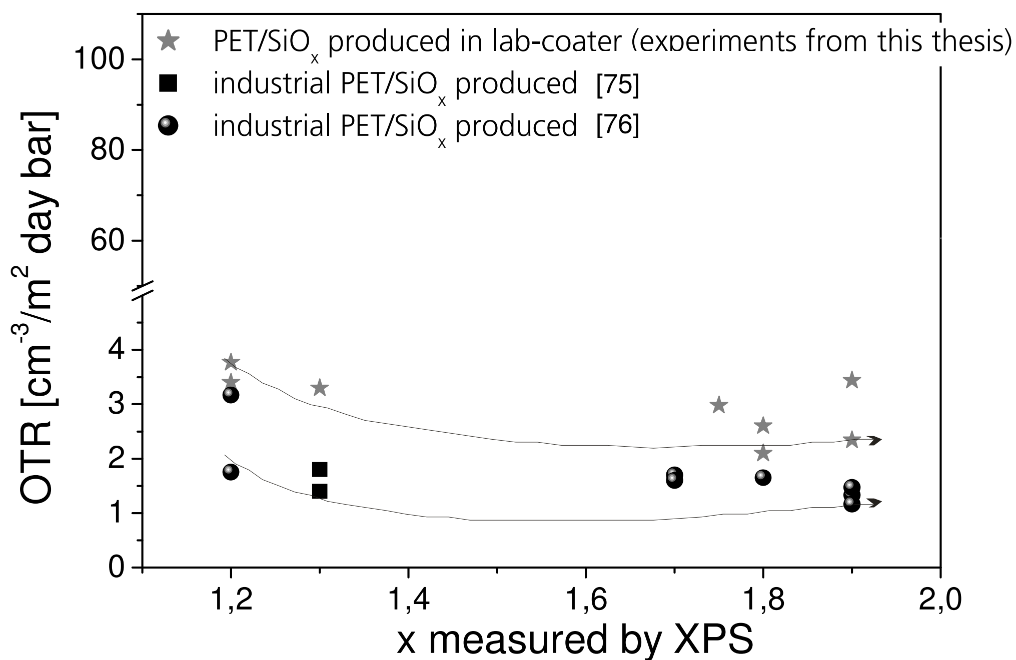

Fig. 57: OTR as a function of the elementary ratio for the samples produced in industrial coater and in lab-scale coater [75, 76]

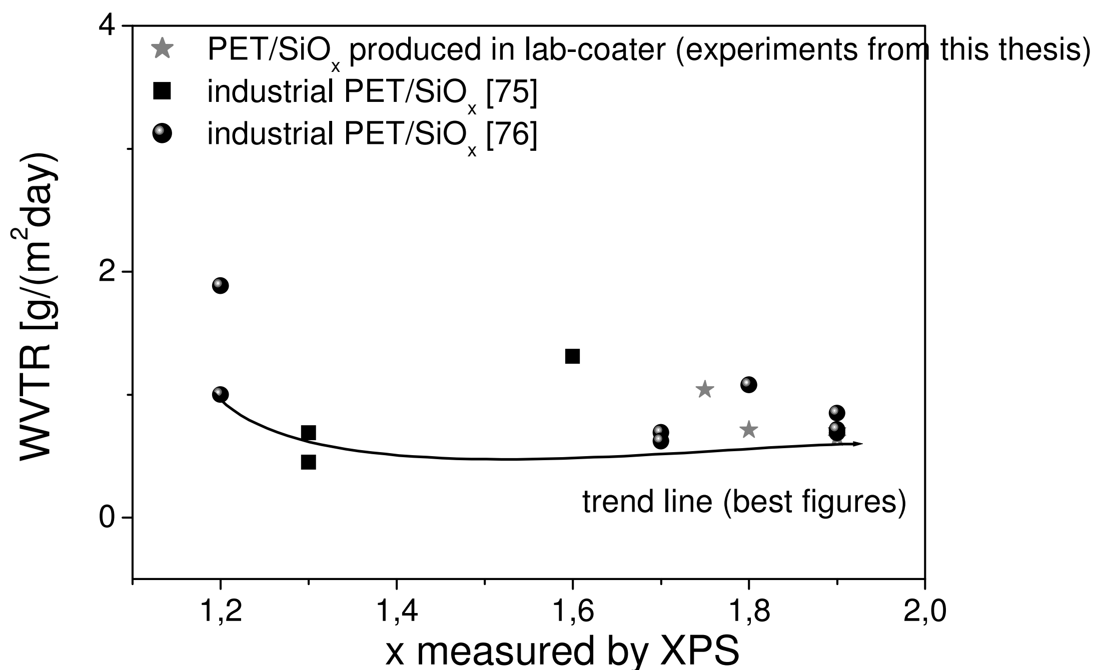

Fig. 58: WVTR as a function of the elementary ratio for the samples produced in industrial coater and in lab-scale coater [75, 76]

On the other hand it seems that the layer thickness is a critical parameter for the good barrier properties. In figs. 59, 60 it can be seen, that very thin inorganic layer – thinner than 20 nm have much worse barrier properties against oxygen and water vapour than the layers with the thickness between 20 – 100 nm. However the barrier of the layers against oxygen is sufficient in broader thickness interval up to 150 nm.

Also a difference in the quality of the produced layers, which were produced by an industrial coater and the layers produced by a lab-coater was observed. The samples produced in the lab coater have a little bit worse barrier properties against oxygen than in the case of industrial layers and nearly no differences in water vapour permeation values. The differences in quality are actually much less than it would be expected, when machine parameters are compared.

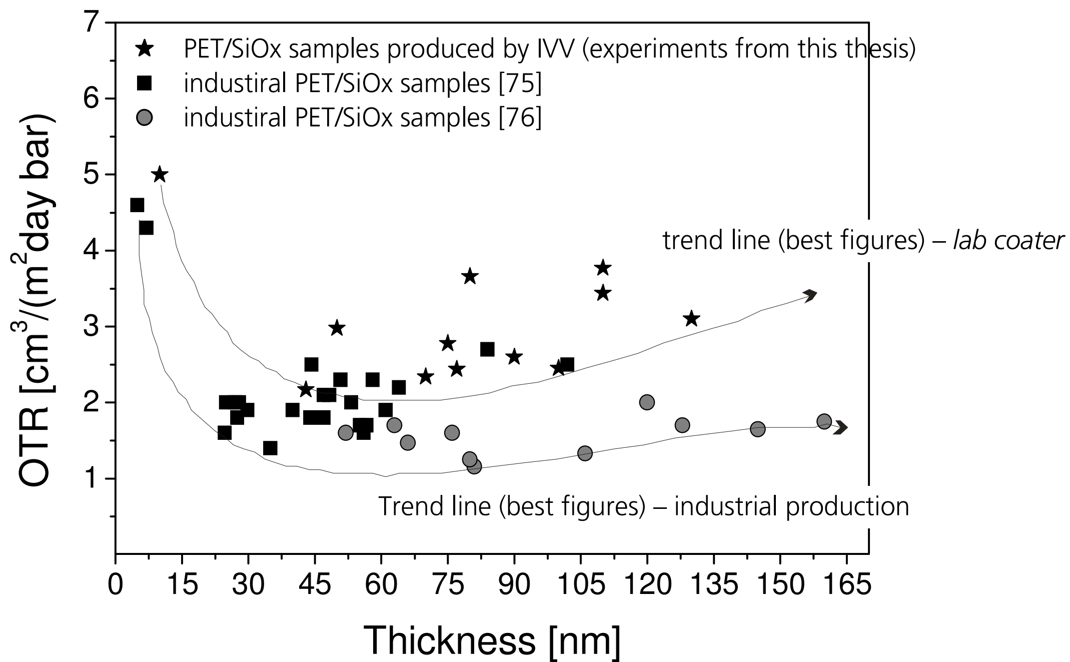

Fig. 59: OTR of the samples produced by an industrial and lab-scale coater as a function of layer thickness [75,76]

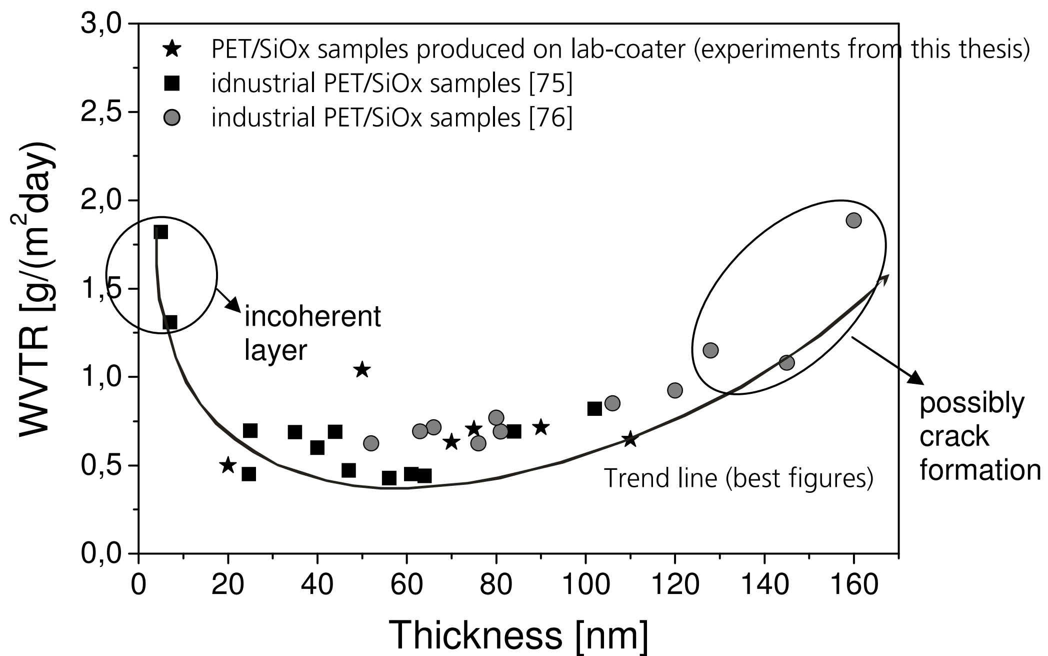

Fig. 60: WVTR of the samples produced by an industrial and lab-scale coater as a function of layer thickness [75,76]

4.2 Optical properties in comparison to chemical composition of the produced samples

The samples with different chemical composition: aluminium oxide layers and silicon oxide layers with the different amount of the incorporated oxygen were produced and online analysed. The figures 61 – 64 show typical online taken spectra, showing the optical properties of the system substrate-thin layer-vacuum as a function of the photon energy in eV. In the case of the silicon oxide layers it can be seen that in the measured spectrum there are significant differences in optical properties of the layers having the different amount of incorporated oxygen. In the case of the sample, which was deposited from the source material of silicon monoxide and therefore a layer with a low oxygen content is expected; no peaks in the measured spectral range are observed. The "effective" extinction coefficient smoothly decreases whereas the "effective" refractive index smoothly increases, however it achieves no maximum in the measured spectral range. In the case of the other silicon oxide samples, which were deposited from a source material with a higher amount of oxygen, namely SiO_x mixture (x expected to be 1,8) and pure silicon dioxide, several peaks can be seen in the spectra. However the spectra distinguish markedly. It can be said that the optical properties and consequently the measured spectra change with the oxygen content variety. The spectrum of the aluminium oxide layer is specific for this material and distinguishes also from every other spectra measured for the silicon oxide layers.

The fit-line corresponding to the calculation from the theoretical model based on the Tauc-Lorentz formula is also shown in the spectra diagrams. This line fit well the measured points in the case of the sample PET 23 SiO_x 040303 and PET 23 SiO 290103-1. The fitting of the spectrum of the sample PET 23 SiO_2 020204 seems to be less accurate in comparison to the both cases discussed above. It is known that the deposition of pure silicon dioxide can cause the building of the layer with the higher degree of the porosity (*see chapter 2.3.1*). It is expected that the measured spectra can be influenced by this parameter and therefore it is much more complicated to find the corresponding fitting line using the simplified theoretical model (*see chapter 3.2.3*)

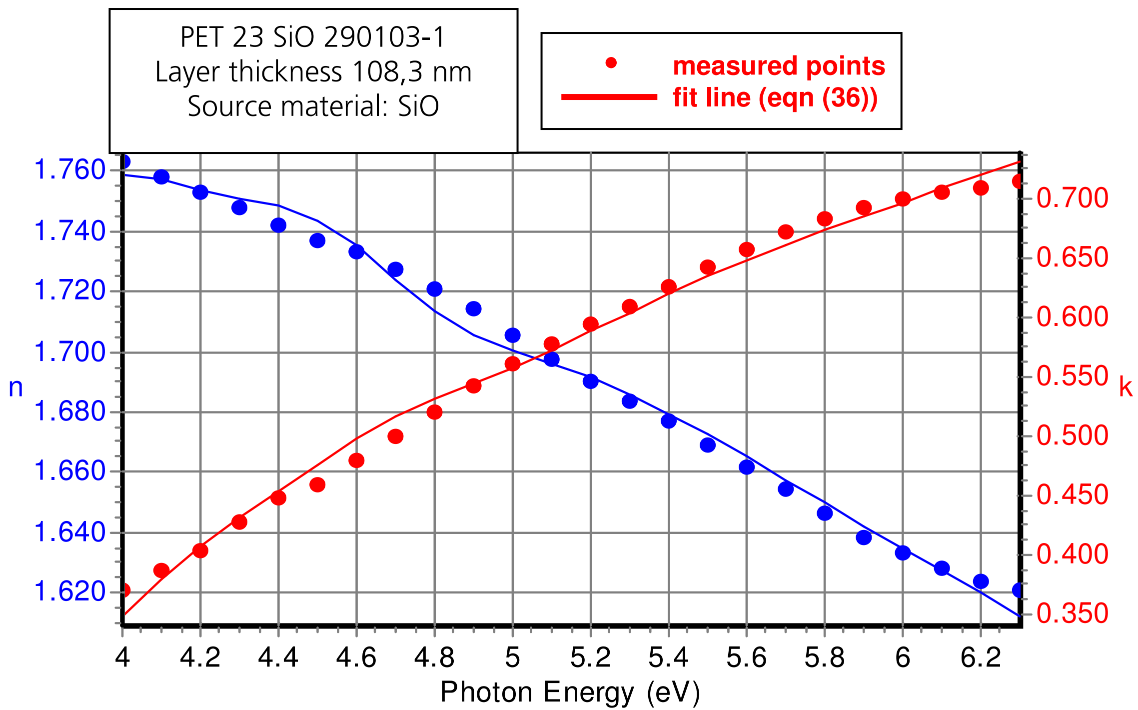

Fig. 61: One of the online taken spectra of formal refractive index n, and formal extinction coefficient, k, measured during deposition. Sample: PET 23 SiO 290103-1 the spectra include interference effects from the substrate.

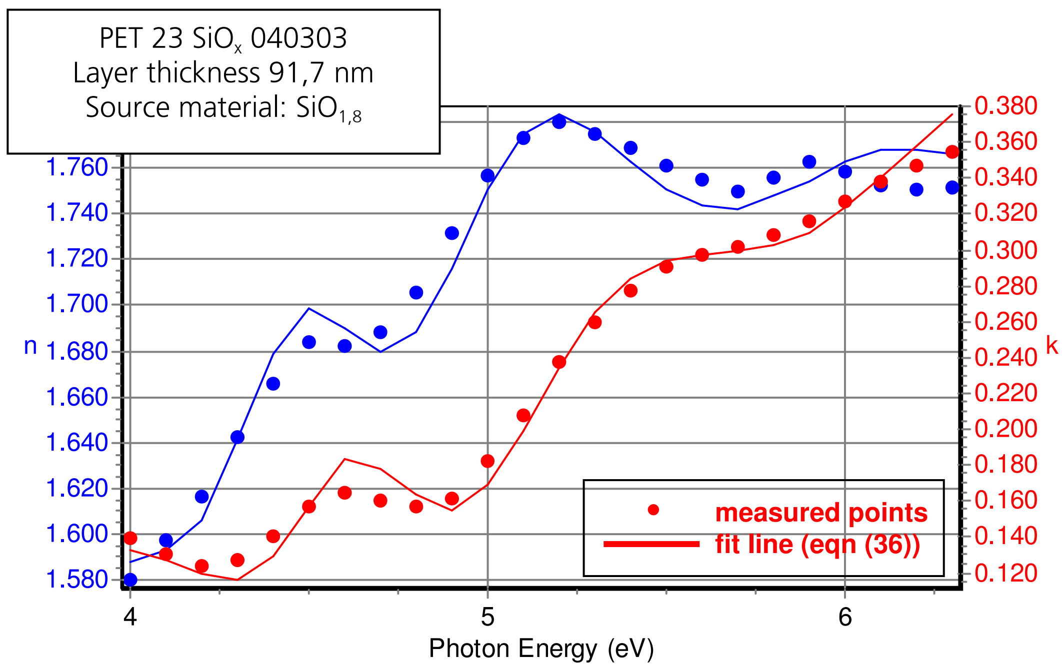

Fig. 62: One of the online taken spectra of formal refractive index n, and formal extinction coefficient, k, measured during deposition. Sample: PET 23 SiO_x 040303 (49th point = 32 m after start of deposition)

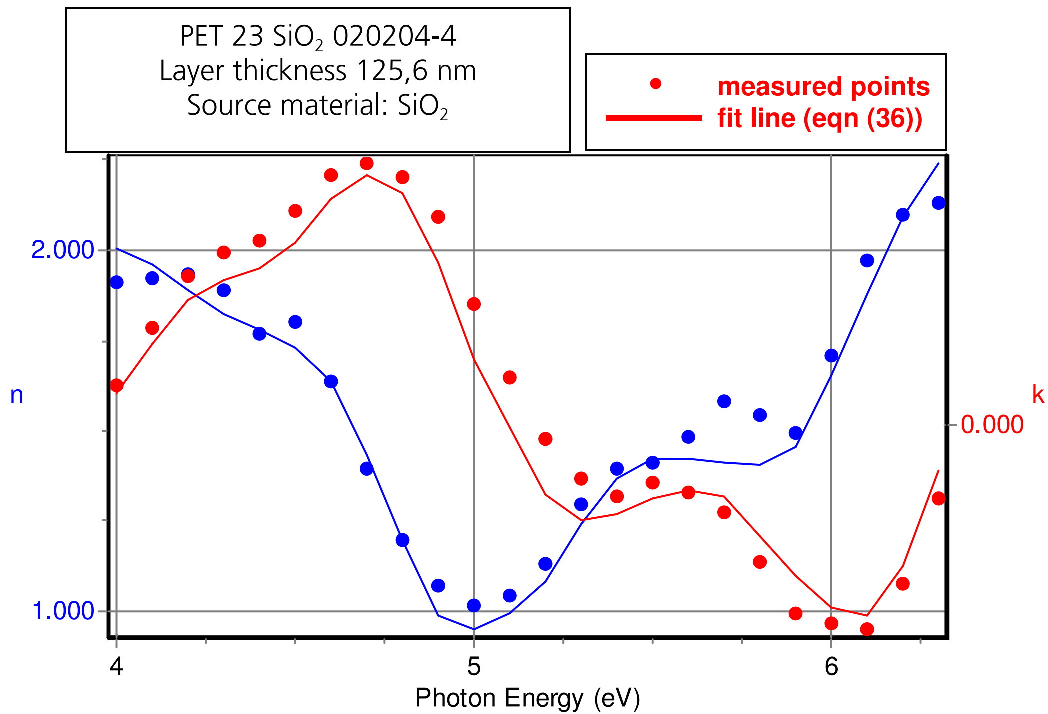

Fig. 63: One of the online taken spectra of formal refractive index n, and formal extinction coefficient, k, measured during deposition. Sample: PET 23 SiO 020204-4

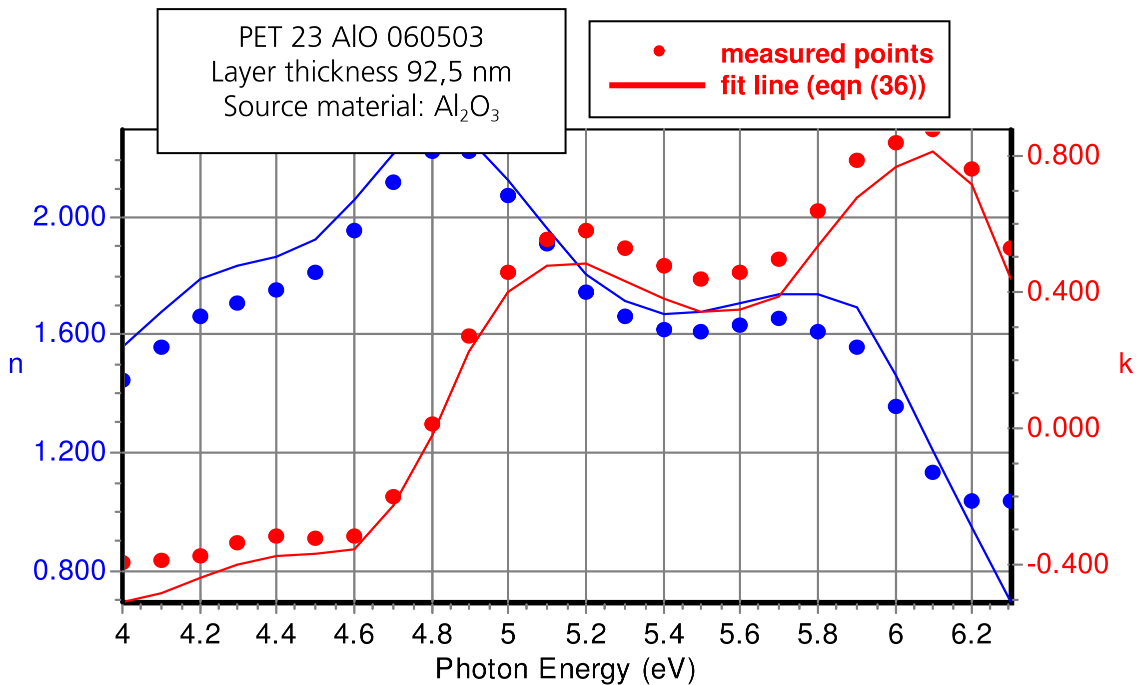

Fig. 64: One of the online taken spectra of formal refractive index n, and formal extinction coefficient, k measured during deposition. Sample: PET 23 AlO_x 060503

The optical properties of the single silicon oxide layers as well as aluminium oxide layers, how it is defined by Tauc-Lorentz parameters after fitting process are shown in figures 65 – 67. The shape of the curves is typical for every material and determines the nature of the single layer. However it is independent from the layer thickness: the layer thickness is additionally calculated from the phase change of the light in the thin layer (*see chapter 2.5.2*). It can be seen that the curves of the refractive index and extinction index vary for the different materials: silicon oxide with different elementary ratio x, silicon dioxide as well as aluminium oxide, which were deposited. The parameters, which characterise the curves are given in the table 12.

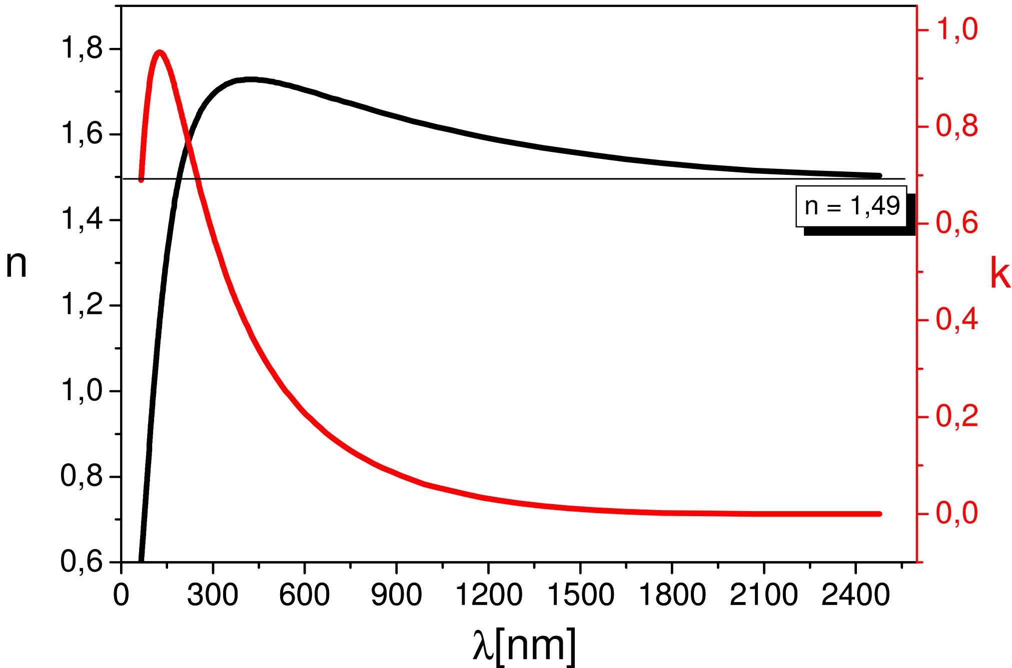

Fig. 65: The Tauc-Lorentz curve for the deposited layer calculated from the theoretical model of the spectrum measured for the sample PET 23 SiO 290103-1. Substrate effects have been eliminated.

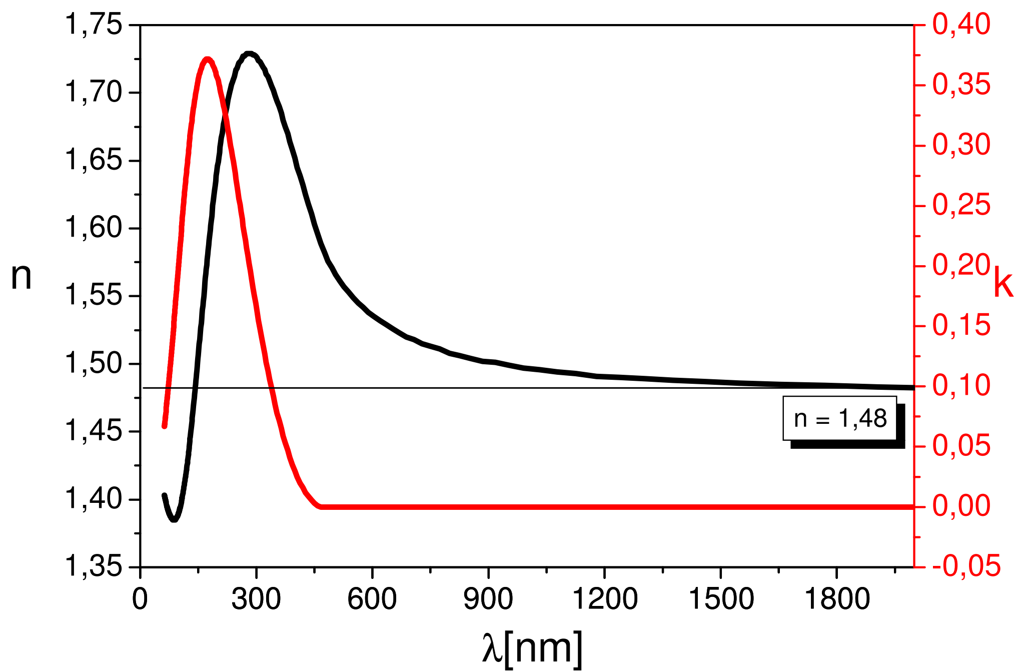

Fig. 65: The Tauc-Lorentz curve for the deposited layer calculated from the theoretical model of the spectrum measured for the sample PET 23 SiO_x 040303 in the 49th point (= 32 m after start of deposition)

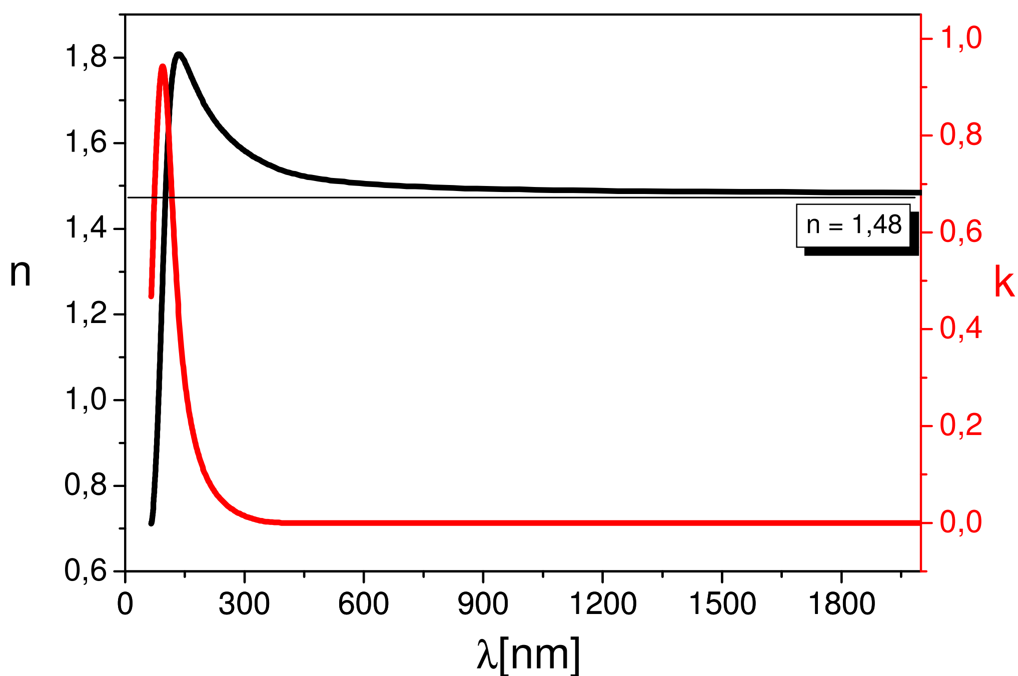

Fig. 66: The Tauc-Lorentz curve for the deposited layer calculated from the theoretical model of the spectrum measured for the sample PET 23 SiO_2 020204-4

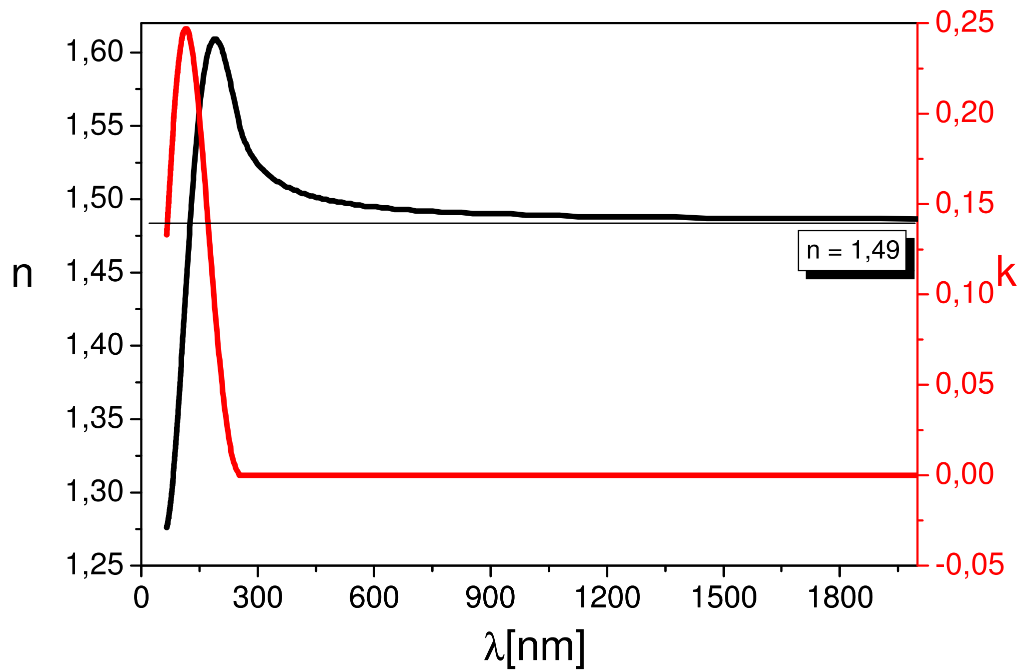

Fig. 67: The Tauc-Lorentz curve for the deposited layer calculated from the theoretical model of the spectrum measured for the sample PET 23 AlO_x 060503

4.2.2 Chemical composition of the layers and layer quality

As it was previously shown the spectra change according the nature of the deposited layers. For determination of the chemical composition of the silicon oxide layers, the penn gap and refractive index (see table 12) were compared with the published values. In virtue of the results it can be seen that the layer of the sample PET 23 SiO 290103-1 has a penn gap like silicon oxide with x ~ 1,7, and the layer of the sample PET 23 SiO_2 020204 like silicon dioxide. It can be seen that although the curves are different, the refractive index (at E→ 0 eV) is nearly the same in all cases – about 1,5. It indicates the silicon oxide layer with the x ~ 1,9

Table 12: Resulting parameters from the Tauc-Lorentz model

Fitting parameters	PET 23 SiO 290103-1	PET 23 SiO_x 040303	PET 23 SiO_2 020204-4	PET 23 AlO_x 060503
Layer thickness [nm]	108,3	91,7	125,6	94,6
E_g [eV]	1,600	2,602	3,978	5,827
ε^{∞}	0,452	2,169	1,043	1,746
A	61,056	34,712	41,237	61,826
E_0 [eV]	9,802	6,094	12,879	7,912
C	17,897	9,814	7,272	11,189
n (E→0)	1,49	1,48	1,48	1,49
χ^2	9,52	5,98	62,4	47,4

The optical properties of one of the deposited layers, namely PET 23 SiO_x 040303 along the web distance is shown below in detail. The figure 68 shows that in the start of the deposition the measured penn gap achieved the values 15 eV (~82 nm) that correlate to the very high x ratio of ~ 2,5. Later the penn gap values decreased continuously to approximately 4,6 eV (~269 nm), whereas the representative value of the silicon monoxide layer is E_0 = 5,6 eV (~220 nm).

The elementary ratio x of the sample PET 23 SiO_x 040303 was measured by XPS in several positions along the web distance. The determined values were between 1,9 – 2,0. It means that values of the penn gap, which can be expected according to these measurements is for the amorphous layer between 9 – 10 eV (138 – 124 nm). However according to the penn gap the oxygen content was frequently determined to be much less than it was measured by XPS measurements.

The refractive index values (see fig. 69) are scattered within the interval 1,4 – 1,6, with some exceptions mainly in the middle part of the deposition process, when the measurement points are lower than 1,3. According to the refractive index the elementary ratio of the silicon oxide layer is within the range of x 1,7 – 2,0.

To order to asses the layer quality and also the existence of porosity, permeation measurement has been performed. The permeation of oxygen through the sample PET 23 SiO_x 040303 was measured to be 2,34 cm^3/m^2 day bar whereas the permeation of water vapour was found to be 0,705 g/m^2 day measured at 23 °C and

50 % rel. humidity. These results demonstrate the existence of a compact barrier layer, so the influence of the porosity on the measured refractive index is expected to be minor.

It seems that the measured refractive index predicts the chemical composition of the layer better than Penn gap calculation. However it should not be forgotten that the refractive index can be strongly impacted by amount of the air in the layer (i.e. porosity of the layer) as well as its degree of crystallinity (aluminium oxide layers) *(see chapter 2.3)* and can not be used alone for the determination of the elementary ratio without additional measurements. The refractive index should only help to indicate if a porous layer is created during deposition or not, when the elementary ratio is known.

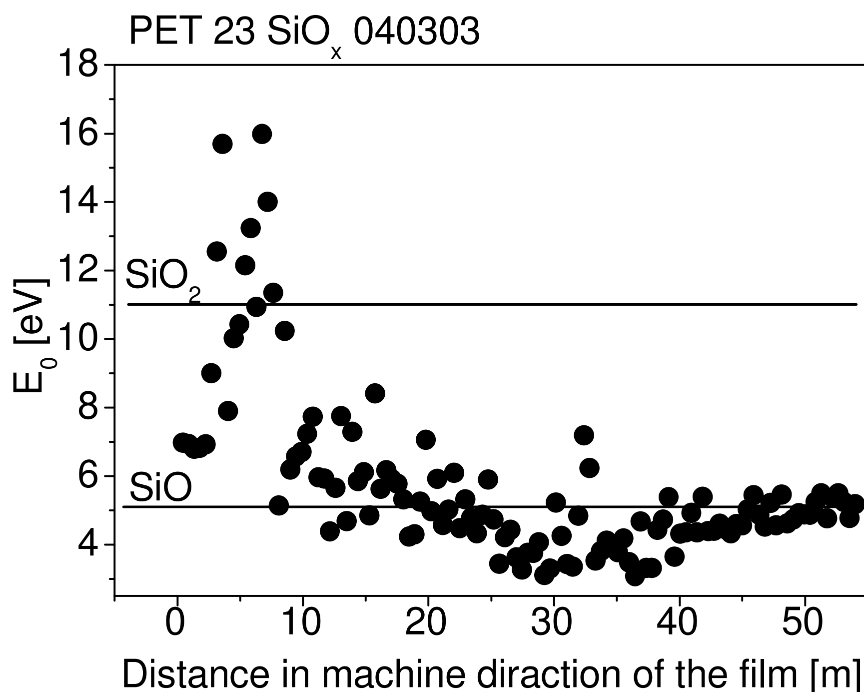

Fig. 68: Penn gap online measured on the sample PET 23 SiO_x 040303 versus expected penn gap of the basic materials SiO and SiO_2 [38].

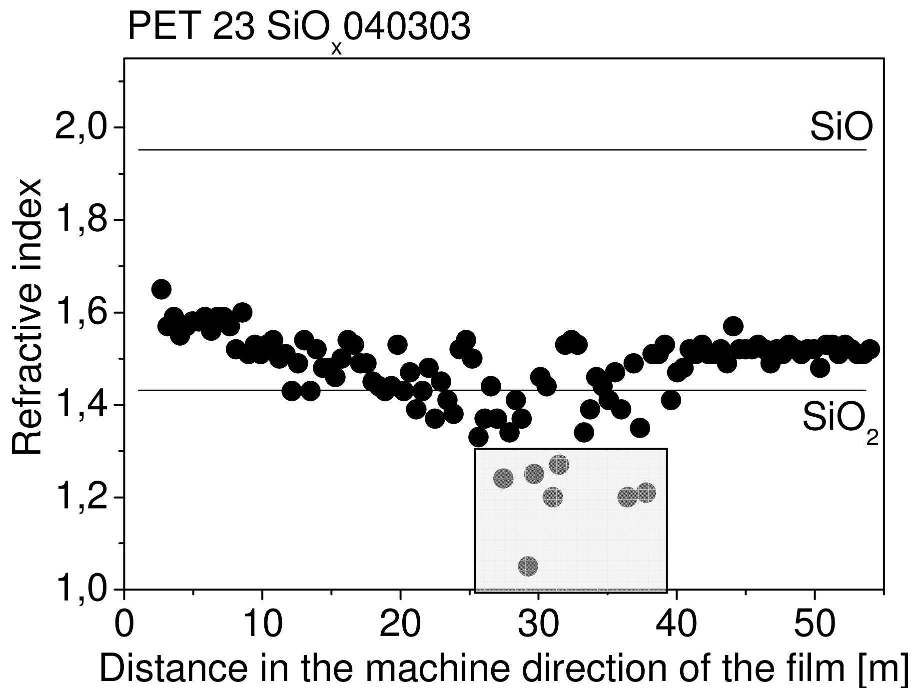

Fig. 69: Refractive index n (E → 0) measured on the sample PET 23 SiO_x 040303 by SE versus expected refractive index of the basic materials SiO and SiO_2 [38].

The figures 62 and 70 show the results after the fitting procedure of the spectra, which were taken from two different points at the beginning and at the middle of the deposition (10th and 49th point) of the sample: PET 23 SiO_x 040303, which was deposited in stationary deposition conditions: the elementary ratio x of the layer in both points is 1,9 according to the XPS measurement and layer thickness is ~ 92 nm. It can be seen that the spectra as well as the fitting line are very similar, whereas the calculated Tauc-Lorentz parameters are completely different (see figures 65 and 71 and table 13). Consequently also the properties such as stoichiometry of the layer were found to be different: the layer in the 10th measured point is indicated to be like silicon oxide with the x = 1,8, and conversely the layer in the 49th point should be like silicon monoxide (in contrary to XPS measurement). It seems that although the form of the Tauc-Lorentz curve is nearly the same in this very thin spectral range, which can be analysed, the next course of the curve may be completely different. Therefore it is also impossible to obtain a reliable information about the layer properties.

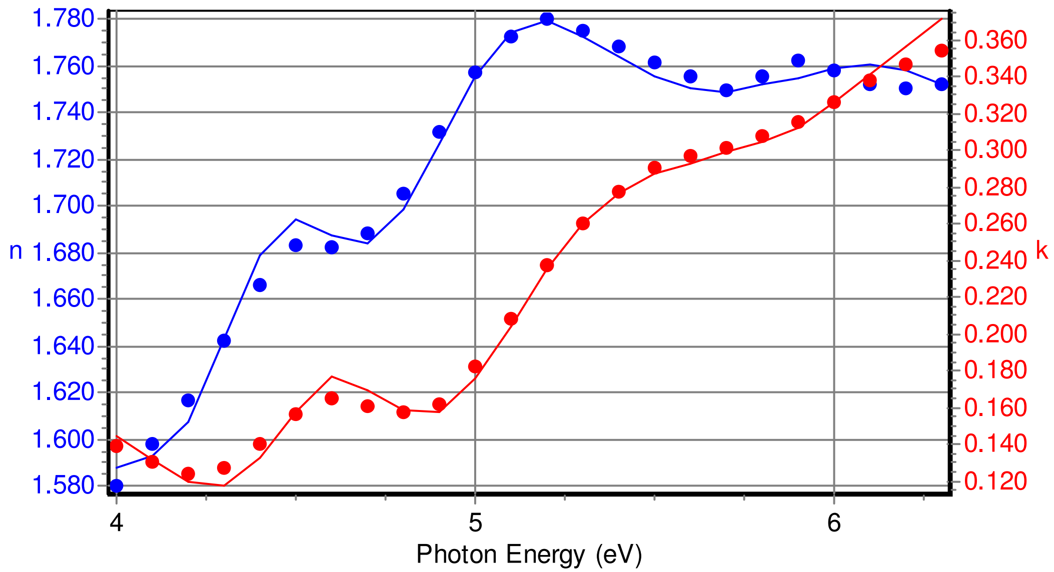

Fig. 70: One of the online taken spectra measured during deposition.
Sample: PET 23 SiO_x 040303 (10th point = 8 m after start of deposition)

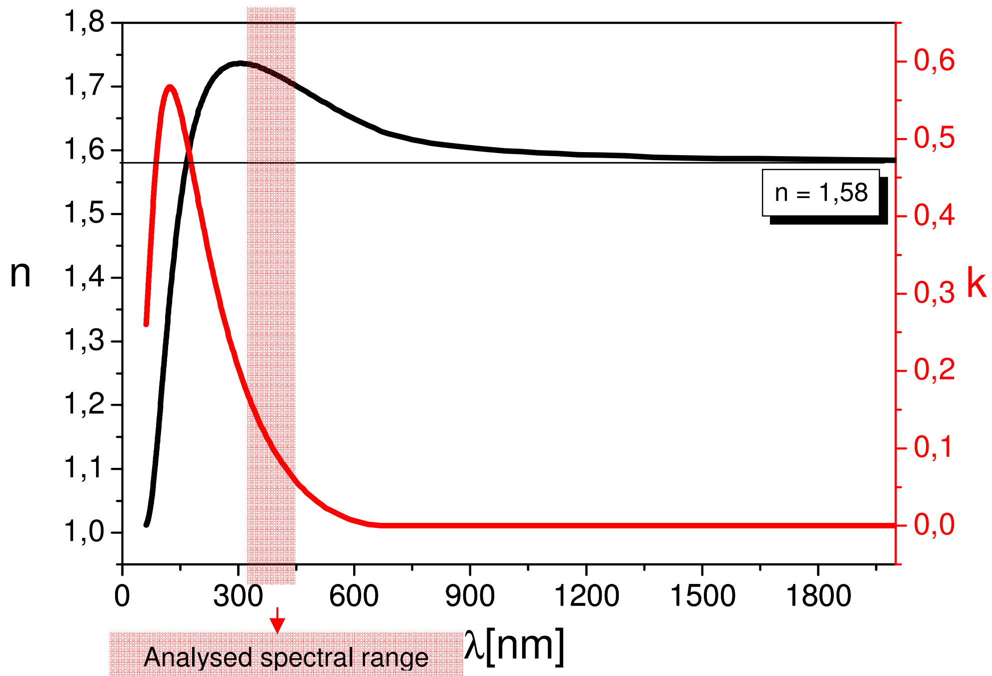

Fig. 71: The Tauc-Lorentz curve calculated from the theoretical model of the spectrum measured on the the sample PET 23 SiO_x 040303 in the 10th point (= 8 m after start of deposition)

Table 13: Fitting parameters of two different points of the sample PET 23 SiO_x 040303

Fitting parameters	**PET 23 SiO_x 040303 – 10th point**	**PET 23 SiO_x 040303 – 49th point**
Eg [eV]	1,769	2,602
ε^{∞}	1,330	2,169
A	37,802	34,712
E_0 [eV]	10,027	6,094
C	16,368	9,814
n (E→0)	1,58	1,48
χ^2	2,69	5,98

The overview of the online measured E_0 values in comparison to the elementary ratio measured by XPS is illustrated in the figure 72. The space between the lines represents the range of the proper values according to the published values [38]. It can be seen that measured penn gap E_0 is not in good correlation with the x values achieved by XPS analysis. The ellipsometer measurements frequently indicated that the layer was close to silicon monoxide with x up to 1,3 in spite of the much higher oxygen content found in the layer by convenient off-line methods.

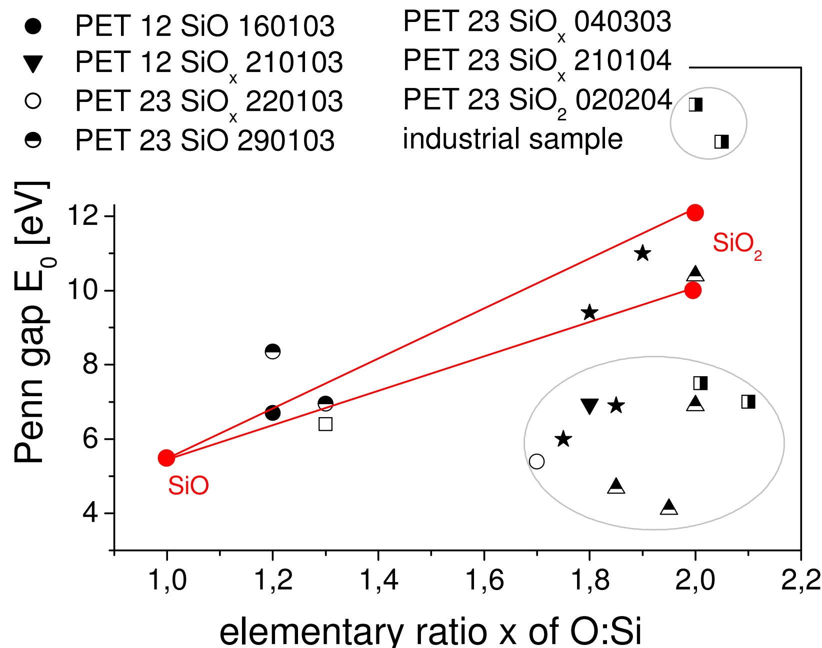

Fig. 72: Penn gap as a function of elementary ratio x measured by XPS (The space between the given lines represents the range of the values to be expected according to the published values [38]).

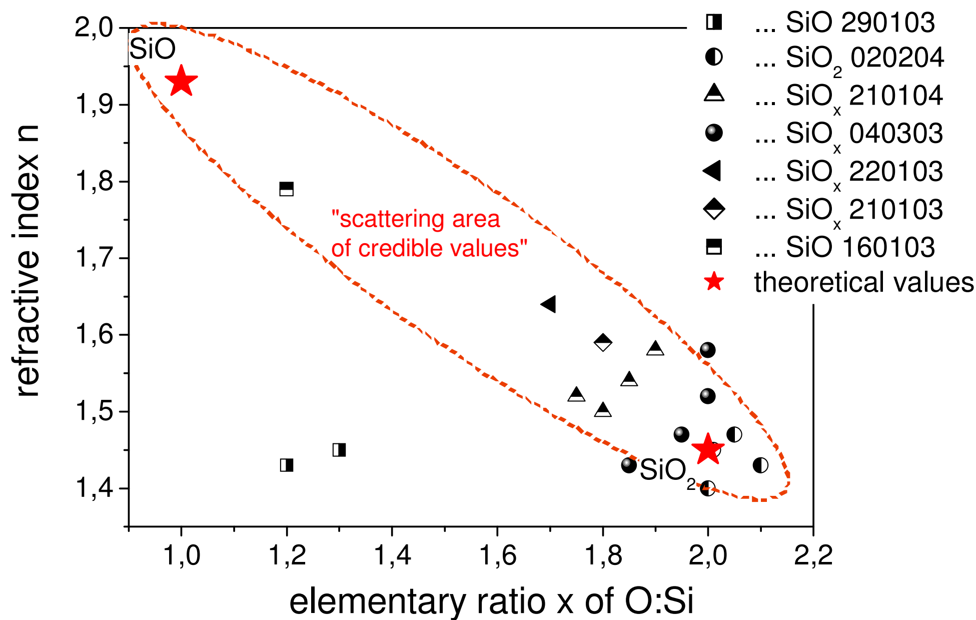

Fig. 73: Refractive index as a function of the elementary ratio x measured by XPS (The marked area represents the range of the values to be expected according to the published values [38]).

Several facts impact the ellipsometric measurements. The most relevant one is the transparency of the polymeric substrate (*see chapter 2.5.2*). Because of the polyethylene terephtalate transparency only very thin range of the spectrum can be used for ellipsometric measurement and it is situated so that only the slope of the curve $\varepsilon_2 = f(\lambda)$ (see fig. 71) is analysed. Therefore it is very difficult to find the "proper direction" of the curve from such s small obtained part of the spectra, which in addition to this is located out of the peak maximum. Those facts hardly complicate the determination of the proper values in the fitting process. Ellipsometry uses a fitting method. There are more unknown parameters in the theoretical model than can be directly calculated from experimentally measured values (*see chapter 2.5.2*). The fitting procedure is based on a comparison between the experimental measurement and the calculations of a given theoretical model (theoretical sample structure), where the aim of fitting is to minimize χ^2 ($\chi^2 = 1/N^*[\Sigma(\chi_{Exp} - \chi_{Th})^2/\sigma^2]$. By automatic on-line modulation it may occur, that the difference in the χ^2 parameter between a "false" and a "correct" fit would be very small. When a fit with correct

results achieves a higher χ^2 parameter than “false” fit, the software identifies the “false” fit to be best solution.

4.3. Online monitoring of the layer thickness

The samples PET 23 µm SiO_x 040303, PET 23 µm SiO_x 250203 and PET 23 µm AlO_x 060503 were deposited in deposition process, in which the web speed as well as the e-beam power were kept constant. The figures 74 – 76 show the layer thickness data along the web length measured by SEM as well as by ellipsometric measurement. Both methods indicate the decreasing layer thickness along the web distance caused by consummation of the deposition material in target as well as thickness fluctuation along the web. This phenomenon is due to the deposition process itself. The material is deposited from a circular rotating target that is periodically heated and evaporated. In the case of the silicon oxide material which is a mixture of from silicon dioxide and silicon, the repeated evaporation causes the creation of a crater on the target, so that the atoms path to the substrate surface is different at every position. Accordingly the resulting layer has different thickness at different position; however the layer thickness is periodically repeated along the web.

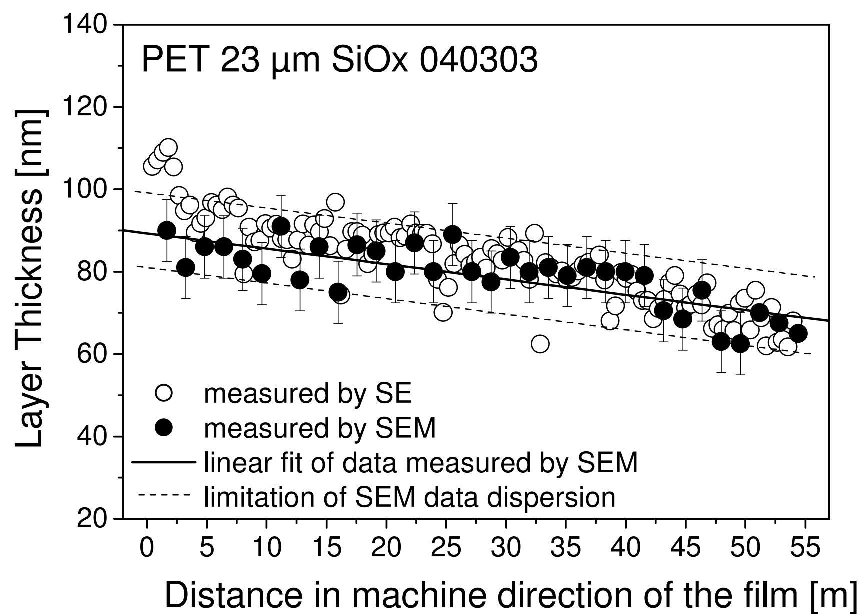

Fig. 74: Layer thickness measurement by SE versus layer thickness measurement by

SEM for the sample PET 23 SiO_x 040303 (*for sample preparation see chapter 3.3*)

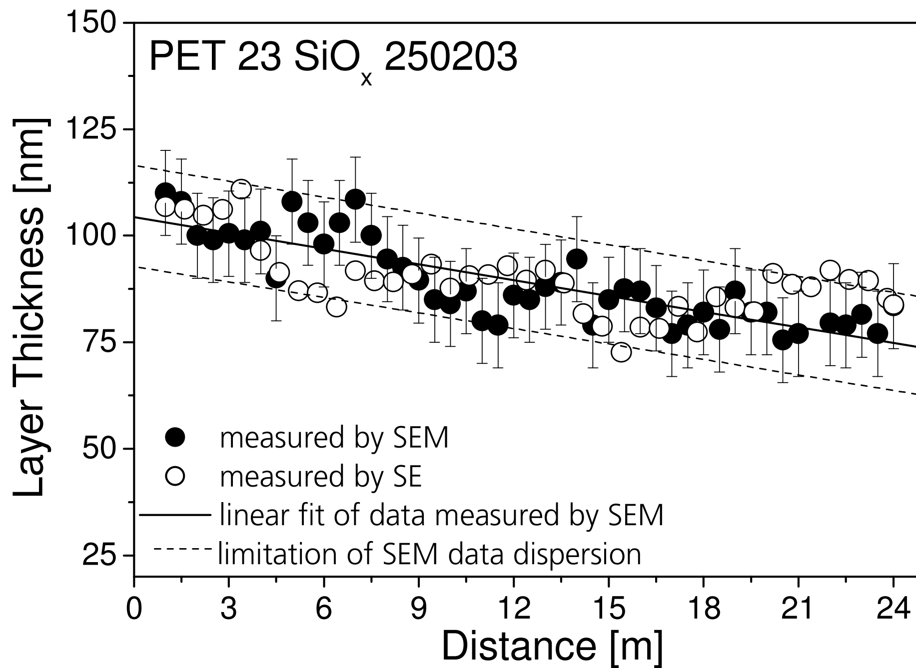

Fig. 75: Layer thickness measurement by SE versus layer thickness measurement by SEM for the sample PET 23 SiO_x 250203 (*for sample preparation see chapter 3.3*)

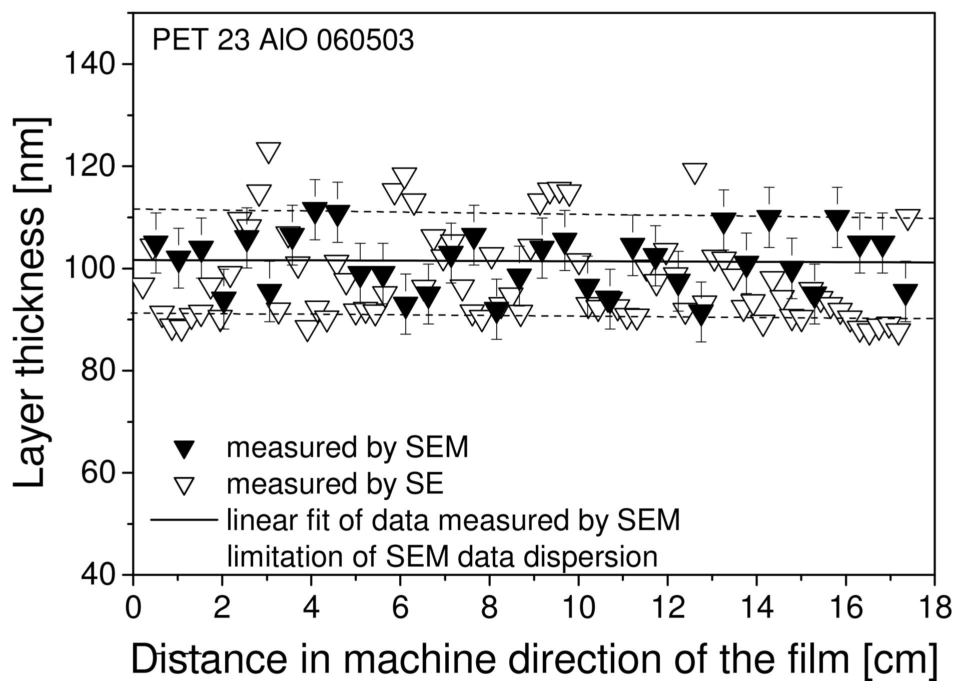

Fig. 76: Layer thickness measurement by SE versus layer thickness measurement by SEM for the sample PET 23 AlO_x 060503 (*for sample preparation see chapter 3.3*)

The samples PET 12 SiO_x 210103, PET 12 SiO 160103, PET 23 SiO_x 220103, PET 23 AlO_x 240103 and PET 12 SiO 290103, PET 23 SiO_x 210104 and PET 23 SiO_2 020204 were prepared by varying the layer thickness. It can be observed in figures 76, 77, 78 how the layer thickness step by step follows the web speed changes during the deposition process. This was determined by SEM as well as by SE analysis.

The sample PET 23 SiO_x 220104 was prepared so that only one big step of the layer thickness was observed (see fig. 79). Again the SE analysis correlates well with the SEM measurement and with the deposition process. In the beginning of the measurement a very thin silicon oxide layer was observed by spectroscopic ellipsometry. It is possible that little amount of material reached the substrate even through the shutter over the source material during the preheating phase. However this effect was not possible to check by SEM. The scanning electron microscopy can not determine the layer thickness lower than 20 nm.

The sample PET 23 AlO_x 170603 was prepared in a simulated instable process, where the e-beam power was varied *(see chapter 3.3.3).* The layer thickness measured by SEM as well as by spectroscopic ellipsometry followed the process changes and showed two maxima along the web, however the course of the layer thickness is much more cursive than when the layer thickness is regulated by changing of the web speed (see fig. 80).

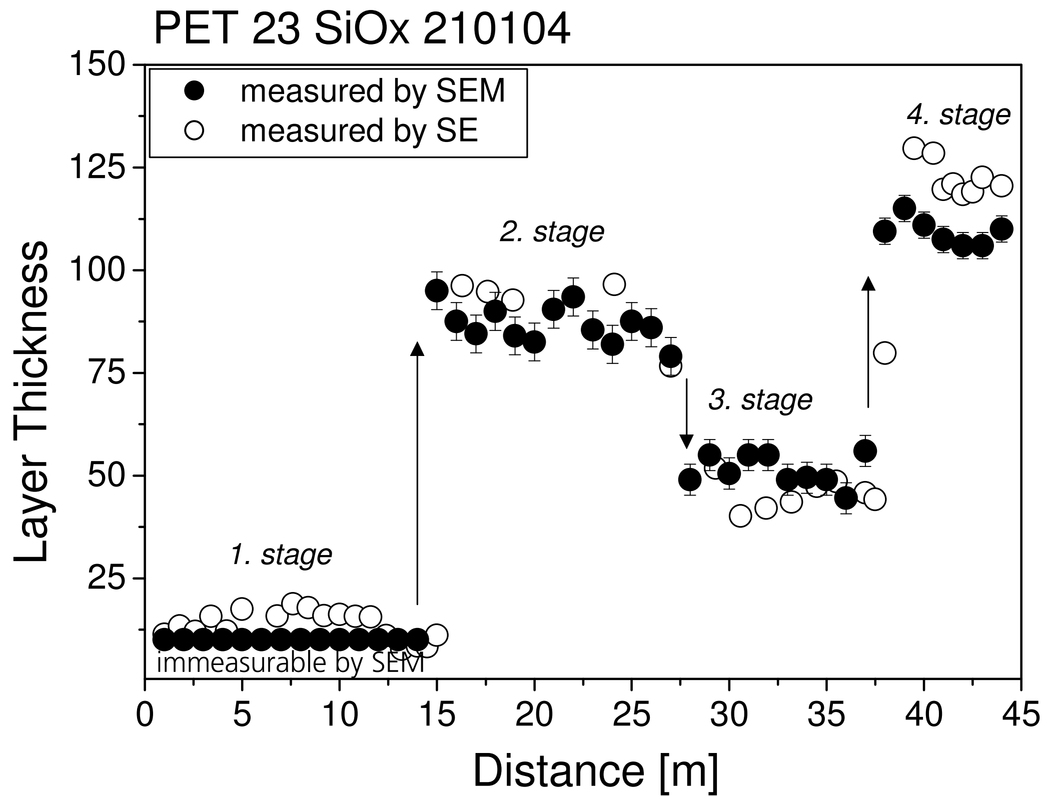

Fig. 77: Layer thickness measurement by SE contra layer thickness measurement by SEM on the sample PET 23 SiO_x 210104 (*for sample preparation see chapter 3.3*)

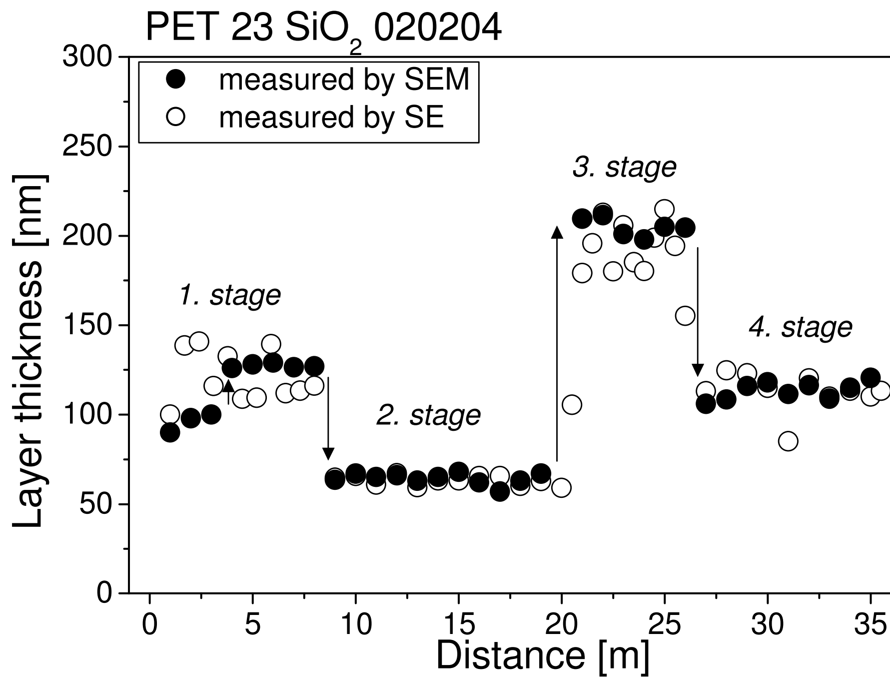

Fig. 78: Layer thickness measurement by SE contra layer thickness measurement by SEM on the sample PET 23 SiO_x (*for sample preparation see chapter 3.3*)

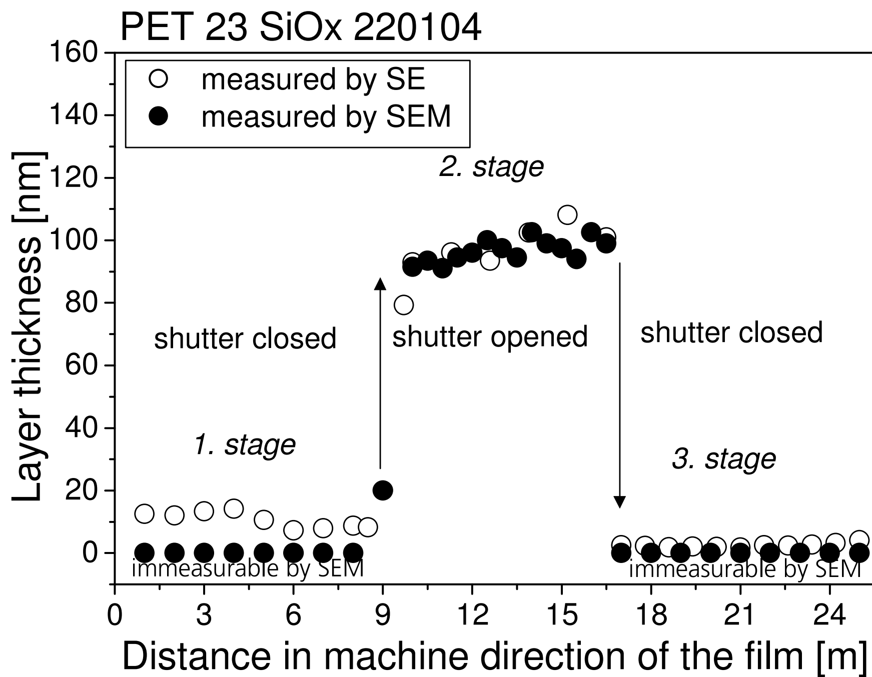

Fig. 79: Layer thickness measurement SE contra layer thickness measurement by SEM on the sample PET 23 SiO_x 220104 (*for sample preparation see chapter 3.3*)

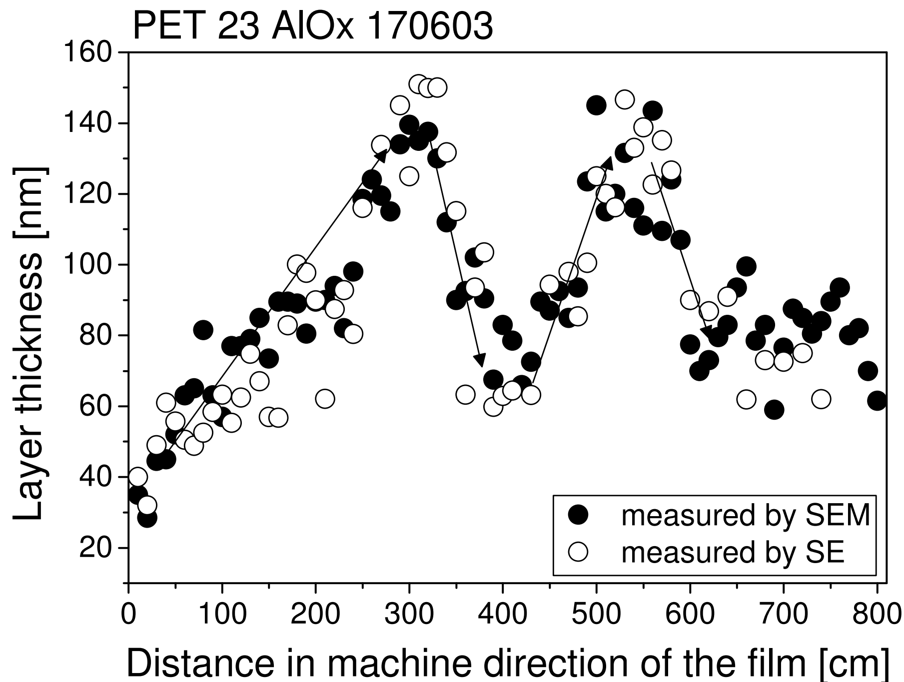

Fig. 80: Layer thickness measurement by spectroscopic ellipsometry (SE) contra layer thickness measurement by scanning electron microscopy (SEM) on the sample PET 23 AlO 170603

4.3.1 Statistical evaluation of the results: layer thickness measured by SEM and SE

The layer thickness of the deposited layers was measured by two different measurement techniques: by scanning electron microscopy and by spectroscopic elllipsometry. The statistical evaluation of both measurement methods were performed by mean of descriptive statistics and the hypothesis testing for the evaluation of the differences between the corresponding data sets. It is assumed that the measured layer thickness values (sampled variables of statistical population) are independent from each other. However in the case of the PET 23 SiO_x 040303 and PET 23 SiO_x 250203 samples a linear correlation between the measured values is predicted since the layer thickness decrease during the deposition process as previously discussed.

The descriptive summaries such as mean, median, mode, standard deviation of mean and median as well as range were calculated and are given in table 14. The

both average parameters: mean and median were evaluated because of the pure physical sense of the first one and higher credibility of the second one. Generally the calculated mean and median of measured samples (and stages for every sample) show no significant differences between the ellipsometric measurement and scanning electron microscopy measurement. Only the means of the samples PET 23 SiO_x 210104 – 4th stage, and sample PET 23 SiO_2 020204 1st and 3rd stage show bigger differences between the means (as well as in medians) obtained from SEM and SE techniques: about 10 nm. The standard deviations of the means and medians for majority of the measurement trials do not scatter significantly; it is between 1 – 2 nm. However for some of the SE measurements data sets the standard deviations were found to be bigger in comparison to the standard deviations obtained from SEM measurements. This concerns especially the sample PET 23 SiO_2 020204 1st and 3rd stages, where the standard deviation of mean is higher than 4 nm and standard deviation of median more than 6 nm. The ranges of those samples are also relatively higher than the ranges of the other samples. The comparison of the statistical parameters indicates a higher scattering in the ellipsometric measurements in comparison to the scanning electron microscopy measurements, especially for the samples of silicon dioxide layers, which are more porous (optically inhomogeneous).

The samples PET 23 SiO_x 040303 and PET 23 SiO_x 250203 have a decreasing trend of layer thickness along the web. Therefore in order to compare the SE and SEM measurements of these samples quantitatively, the linear regression parameters were calculated and are given in the table 15. The slope (b) and intercept point (a) of the calculated line from SE as well as SEM measurement variables for both samples show no significant differences. The standard deviation is high; in the case of the sample PET 23 SiO_x 040303 approximately 5 nm and in the case of sample PET 23 SiO_x 250203 it is around 6,7 nm. That and also lower correlation coefficient R* indicates that values are highly scattered. For the hypothesis whether the data sets of the SE and SEM measurements come from the same population non-parametric Mann-Whitney test was preferably applied. The t-test was not used because the t-test gives the information whether the means of the populations are different (or not). In this case the data sets had a decreasing tendency in thickness. So it was decided

not to use the test for the differences of the means for getting the answer to the question whether the data sets are different (or not) (see table 17).

The existence of a possible correlation between the values measured by SE and SEM was also investigated by means of Pearson (normality desired) and Spearman tests (non-parametric) for the samples of PET 23 SiO_x 040303 and PET 23 SiO_x 250203. In order to apply Pearson and Spearman tests on a same sample the number of the measured values from both measurement techniques should be the same and paired. The neighbouring values from SE measurement were arithmetically averaged so that corresponding pairs of SEM and SE values were obtained. By checking the r_p and r_s parameters, it was found out that there is a significant correlation between the two measurement methods (see table 16). The Spearman correlation coefficient was calculated also for the sample PET 23 AlO_x 060503, however in this case no correlation was found between the values.

Table 14: Descriptive statistics

Sample	**stage**	**Meas. method**	**n**	**Mean** $\bar{x} \pm s_{\bar{x}}$	**Median** $\tilde{x} \pm s_{\tilde{x}}$	**Mode** $\hat{x}$	R
PET 23 SiO_x 210104	1	SEM	0	-	-	-	-
		SE	18	13,6 ± 0,8	14,5 ± 1,3	16,2	11,0
PET 23 SiO_x 210104	2	SEM	13	86,7 ± 1,3	86,0 ± 1,2	84,5	16,0
		SE	5	91,4 ± 0,9	94,8 ± 5,7	95,0	18,0
PET 23 SiO_x 210104	3	SEM	10	51,3 ± 1,7	50,0 ± 1,7	47,5	11,5
		SE	8	45,5 ± 2,1	45,0 ± 1,9	44,1	11,7
PET 23 SiO_x 210104	4	SEM	7	109,3 ± 1,2	109,5 ± 1,4	109,9	9,0
		SE	8	122,4 ± 1,5	120,8 ± 2,7	117,4	11,3
PET 23 SiO_x 220104	2	SEM	14	96,6 ± 1	96,8 ± 1,4	96,9	11,5
		SE	6	99,0 ± 3,5	98,5 ± 2,7	97,5	15,2
PET 23 SiO_x 020204	1	SEM	5	127,3 ± 0,5	126,3 ± 0,9	124,2	3,0
		SE	8	118,4 ± 4,0	111,9 ± 6,7	98,9	30,7
PET 23 SiO_x 020204	2	SEM	12	64,3 ± 0,9	65 ± 1,15	66,4	11
		SE	12	63,1 ± 0,8	65,6 ± 1,7	70,6	8,6
PET 23 SiO_x 020204	3	SEM	6	204,9 ± 2,1	204,8 ± 3,9	204,4	11,5
		SE	10	194,7 ± 4,3	194,9 ± 7,3	195,5	35,7
PET 23 SiO_x 020204	4	SEM	9	113,4 ± 1,6	115 ± 2,3	118,1	14,5
		SE	10	115,3 ± 1,7	113,4 ± 2,9	109,5	14,7
PET 23 AlO_x 060503	-	SEM	34	101,4 ± 1,5	102,3 ± 1,7	103,9	20
		SE	80	98,0 ± 1,2	94,8 ± 1,3	88,4	35,5

Table 15: Linear regression y = a + bx for the SEM and SE measurement of the samples PET 23 SiO_x 040303, PET 23 SiO_x 250203

Sample	Meas. method	n	a	b	SD [nm]	R*
PET 23 SiO_x 040303	SEM	34	89,2	-0,40	4,9	-0,77
	SE	115	97,0	-0,51	4,7	-0,86
PET 23 SiO_x 250203	SEM	46	104,4	-1,05	5,5	-0,84
	SE	40	98,7	-0,83	6,8	-0,61

Table 16: Correlation coefficients between the SEM and SE measurement for the samples PET 23 SiO_x 040303, PET 23 SiO_x 250203 and PET 23 AlO_x 060503

Sample	Correlation according to	Correlation coefficient	Result
PET 23 SiO_x 040303	Pearson	r_p = 0,638	yes
	Spearman	r_s = 0,873	yes
PET 23 SiO_x 250203	Pearson	Not normally distributed	Not normally distributed
	Spearman	r_s =0,80	yes
PET 23 SiO_x 060503	Pearson	Not normally distributed	Not normally distributed
	Spearman	r_s =0,43	no

Yes = according to Pearson (or Spearman) (α = 0,05) the correlation between two groups is statistically significant; **No** = according to Pearson (or Spearman) (α = 0,05) there is no correlation between two groups

Before performing any statistical test for conformity (t-test and Mann-Whitney test), the normality test of Shapiro and Wilk, which is suitable for testing of the small-sized data set, was carried out for the measured variable sets of SE and SEM measurements of all samples. For the samples, of which their normal distributions were confirmed by the Shapiro-Wilk test, both t-test and Mann-Whitney tests were applied in order to evaluate the differences in the values measured by SE and SEM measurements. If the data were not normally distributed, then for those samples only Mann-Whitney test was used.

The hypothesis, which claims that the SEM measurement data set and SE measurement values set do not differ significantly, was confirmed in the case of the

samples: PET 23 SiO_x 210104 stage 2, PET 23 SiO_x 220104, PET 23 SiO_x 020204 all stages, PET 23 SiO_x 040403 and PET 23 SiO_x 250203. This hypothesis was not confirmed in the case of the sample PET 23 SiO_x 210104 3rd and 4th stages and PET 23 AlO_x 060503.

Table 17: test for normality and tests for conformity of all samples

Sample	**Stage**	**Meas. method**	**test for normality**	**T-test**			**Mann-Whitney test**		
				t	**p**	**Result**	**W**	**p**	**Result**
PET 23 SiO_x 210104	2	SEM	ND	-	-	-	64	0,124	ident
		SE	Non-ND						
PET 23 SiO_x 210104	3	SEM	ND	2,13	0,051	ident	*46*	*0,005*	non-ident
		SE	ND						
PET 23 SiO_x 210104	4	SEM	ND	6,78	0,000	non-ident	28	0,000	non-ident
		SE	ND						
PET 23 SiO_x 220104	2	SEM	ND	0,9	0,403	ident	70,5	0,591	ident
		SE	ND						
PET 23 SiO_x 020204	1	SEM	ND	2,2	0,064	ident	45	0,164	ident
		SE	ND						
PET 23 SiO_x 020204	2	SEM	ND	1,04	0,312	ident	168	0,312	ident
		SE	ND						
PET 23 SiO_x 020204	3	SEM	ND	2,17	0,051	ident	64	0,175	ident
		SE	ND						
PET 23 SiO_x 020204	4	SEM	ND	0,77	0,453	ident	83	0,624	ident
		SE	ND						
PET 23 AlO_x 060503	-	SEM	ND	-	-	-	2443	0,003	non-ident
		SE	Non-ND						
PET 23 SiO_x 040303	-	SEM	ND	-	-	-	2224	0,074	ident
		SE	ND						
PET 23 SiO_x 250203	-	SEM	Non-ND	-	-	-	1925	0,513	ident
		SE	Non-ND						

Test for normality: **ND** = according to Shapiro-Wilk test the sample is normal distributed on the probability level $\alpha = 0,05$; **non-ND** = according to Shapiro-Wilk test there is evidence that the data do not follow a normal distribution at $\alpha = 0,05$

Tests for conformity: ***T-test*: ident** = There is no evidence for a difference in the population means at $\alpha = 0,05$; **non-ident** = There is evidence for a difference in the population means at $\alpha = 0,05$; ***Mann-Whitney test:* ident** = The data support the hypothesis that the two samples come from identical populations ($\alpha = 0,05$); **non-ident** = The data do not support the hypothesis that the two samples come from identical populations ($\alpha = 0,05$)

4.3.2 Summarisation of all the measured samples

An overview of the layer thickness means of the silicon oxide samples, which were measured by SE and SEM are shown in fig. 81. It can be seen that the measured layer thickness values lie either near or direct on the line (y = 0 + 1.x), which demonstrate the ideal equivalence of both measurements methods. The calculated linear regression line (y = a + b.x) show real equivalence of both measurements techniques. The slope (b) is 0,90 instead 1, which is expected in the ideal case, the intercept point (a) of the calculated line is 10,2 nm. The standard deviation is 10,7 nm, and shows how the points scatter around the calculated line. The regression coefficient R* is very high 0,97 and ilustrate that there is a very good linear correlation between the values.

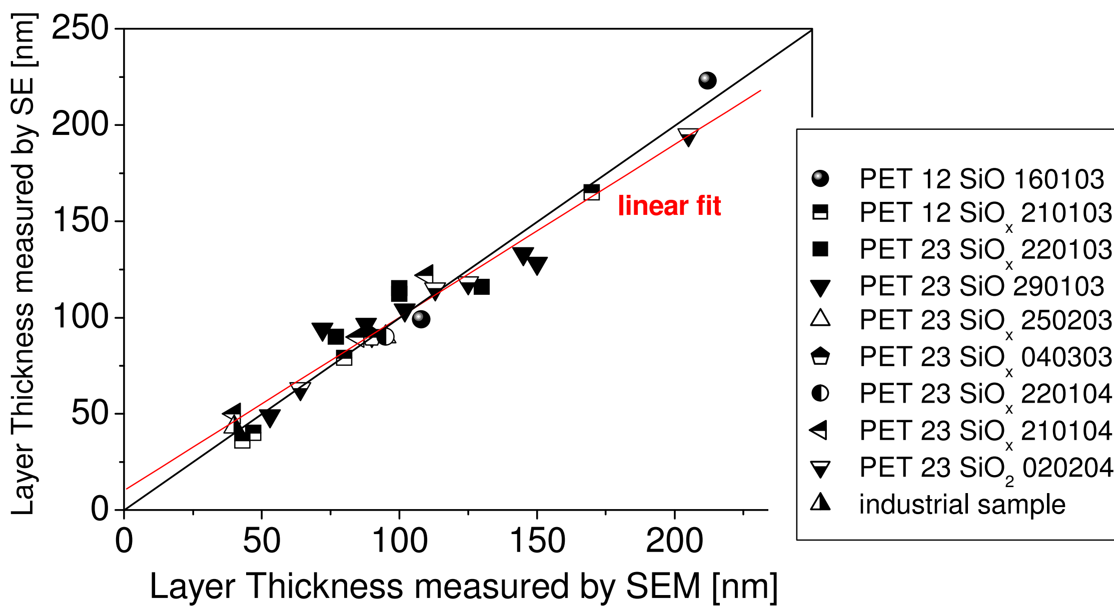

Fig. 81: Comparison of the averaged thickness values of silicon oxide layers measured by SEM and SE.

The figure 82 shows the comparison between the SE and SEM measurements in the case of aluminium oxide layers. The shown data are either arithmetical means of the layer thickness values of the deposited samples or in the case of the sample PET 23 AlOx 170603 the values are the maxima and minima of this layer thickness variation (see fig. 80). It can be seen that the linear fit match very well to the ideal line y = 0

+1.x. The slope (b) of the line was in this case 1,03 and the intercept point (a) was -0,18. The standard deviation was 9,7 nm in comparison to the standard deviation of the silicon oxide layers it can be said that the uniformity of the measurements do not depend on the layer material. The regression coefficient R* is also in this case very high: 0,98 and show that the values linearly correlate very strongly with each other.

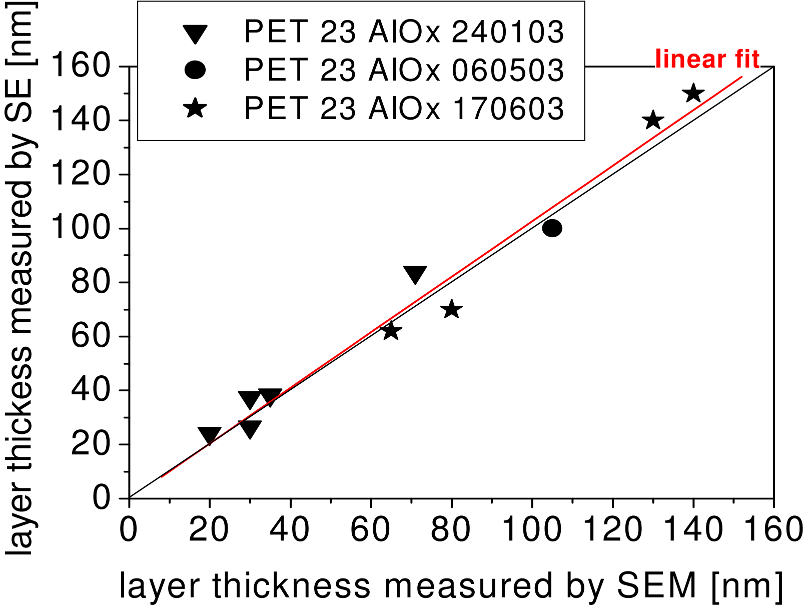

Fig.82: Comparison of the averaged thickness values of aluminium oxide layers measured by SEM and SE.

5 Conclusions

Stability of the measurement setup and sampling rate

- It was demonstrated that the ellipsometer give stable signal for all photon energies of the selected spectra under vacuum as well as in air. Some interruptions were observed during pumping down or venting of the deposition chamber. This was most probably caused by the vibrations the chamber parts during these actions.

- The ellipsometer gives a consistent spectra, which were measured for the blank substrate, independently of the web speed up to 5 m/min. It can be predicted that vibrations coming from the winding do not influence the ellipsometric measurement.

- It was also shown that the acquisition time is less than 5 seconds, so that the sampling is realised every ~ 0,5 m, when the web speed is 5 m/min and every ~ 0,1 m when the web speed is 1 m/min.

Ellipsometric measurement of the optical properties and derived properties (e.g. stoichiometry)

- The problems in numerical treatment of the recorded spectra lead to scattering results in penn gap E_0 and refractive index n (when $E \rightarrow 0$) and therefore do not allow the assessment of the layer properties like its stoichiometry or porosity.

- In line monitoring of the expected derived properties such as stoichiometry, porosity of the deposited layer is impossible at the moment. Presently in this field the additional investigations follow within the EU-funded project: FLEXONICS.

Ellipsometric measurement of the layer thickness

- The layer thickness measurements were satisfactory for silicon oxide layers having different stoichiometry, when elementary ratio x is within 1,3 – 2,2. The measured layer thicknesses were between 40 nm and 200 nm.

  - The limitations of ellipsometer were found in analysis of the silicon dioxide layers. In some cases the ellipsometer determined significantly higher layer thickness than it was measured by scanning electron microscopy. This effect comes probably from the higher porosity of these layers.

- The layer thickness measurements were satisfactory also for the aluminium oxide layers having thicknesses between 20 and 150 nm.

Further results

Additional results, which come from this research work were the detailed comparison of the final properties of the deposited films produced by lab-coater of Fraunhofer IVV and the semi-production machines existing at the partner companies.

- According to the layer thickness measurements it was discovered that thickness of the layer deposited by the lab-coater is slightly unstable and during deposition decreases simultaneously with the sinking material volume.

- The barrier properties of the inorganic layers produced by the lab-coater are comparable with those produced by the semi-production machines. However the oxygen transmission rates of produced samples were slightly higher, whereas the water vapour transmission rates are nearly the same to the values of the samples produced on the semi-production machines.

6 Summary

The inorganic layer improves the barrier properties of the polymeric substrates against gases and vapours such as oxygen, moisture or different organic compounds and protects by this way the packaged food stuffs against the environmental impact. The most used material for creating the coatings are aluminium (Al), which makes opaque films and transparent silicon oxide and aluminium oxide.

The deposited layers have to be monitored for their thickness and quality during the deposition process in order to guarantee the barrier properties of these layers. However a full quality control equipment for the online testing of the layer thickness, stoichiometry and quality of the transparent inorganic layers such as silicon oxide and aluminium oxide layers is not available, presently. There is the possibility of monitoring the deposition process either by off-line sampling after deposition or by on-line measurement of the light transparency. Unfortunately the light transparency measurement delivers a quantity, which includes the information of the layer thickness and the chemical composition (stoichiometry) simultaneously. It means that it is directly not possible to determine, which variable – layer thickness or stoichiometry – was changed.

The aim of this research work was to evaluate the novel control equipment (modified UV-VIS phase modulated spectroscopic ellipsometer) during the deposition, which was installed at lab e-beam coater at Fraunhofer IVV and to give information about the efficiently concept of the measurement.

The lab e-beam coater was modified for the installation of the ellipsometer. The parts of the ellipsometer were installed on top of the deposition chamber, so that the analysis take place on the smooth roller. In this position the deposited layer comes in direct contact with the analysing light beam and by this design the vibration of the winding substrate, which could influence the ellipsometric measurements, were strongly reduced.

After installation the functionality of the ellipsometer was tested and it can be said that the ellipsometer delivers the stable signal in all 32 analysed energy channels under vacuum as well as under atmosphere. Signal interruptions were observed during pumping down likewise during venting the deposition chamber, probably due to the vibration of the chamber components. This phenomenon is not critical for online control during deposition, which evidently takes place under vacuum.

The time needed for the acquisition (it means the time needed to obtain the spectra) was in the case of automatic acquisition mode around 16 seconds and in the case of fixed acquisition mode approximately 4 seconds. Obviously the ellipsometric measurement delivers information frequently about the deposited layer, which should not be obtainable by standard sampling.

For the exhaustive testing of the ellipsometric measurements reliability the more samples of transparent inorganic coating on polyethylene therephtalate were produced in different quality, layer thickness and chemical composition and tested on-line by ellipsometer as well as by standard off-line methods. The layer thickness measured by ellipsometry matched very well the layer thickness values, which are measured by scanning electron microscopy. It is very positive that besides very well correlation of ellipsometric measurements and SEM measurements of layer thickness the layer thickness determined by spectroscopic ellipsometry in on-line course is not only reliable, and also independent from the stoichiometry of the produced layer contrary to the online light transparency measurement.

The on-line ellipsometric analysis of the chemical composition – stoichiometry of the deposited layer is not yet satisfied. The observed Penn gap (E_0) determined by the ellipsometric analysis was found to be much lower than it was expected according to the x-ray photoelectron spectroscopy measurement results of many samples. Additionally the measured Penn gap was often strongly scattered.

It seems that the spectral range, which can be used for the ellipsometric analysis is too narrow to obtain reliable results by the fitting procedure. This is due to the

transparency of the polymeric substrate. The ethylene terephthalate is transparent up to 3,5 eV (350 nm).

In addition to that currently used model, which comprises of the substrate and simple layer, is too simplified. It would be more useful to incorporate the additional effects of the interlayer structure or layer surface roughness. On the other hand a full theoretical model including all possible effects would overcomplicate the mathematical calculation and prolong the time needed for the modulation making it unsuitable for a real online measurement.

All these open questions need several years of experience and testing to solve them. However it was the first time when such a technology had ever been used successfully for online control in the roll to roll coating machines.

Secondary, the result of this research work is a detailed mapping of the deposition process of the lab-coater at Fraunhofer IVV.

It was found out that thickness of the layer deposited by the lab-coater is slightly unstable and decreases simultaneously during deposition with the sinking material volume. The fluctuation of the layer thickness along the web is wave shaped such that it follows the character of the surface of source material for deposition. Frequently re-evaporation of the source material in the target causes a typical structure, which is liable for the layer thickness variation. Surprisingly this phenomenon does not effect the chemical composition – stoichiometry critically as it was determined by XPS measurements on the several places along the web.

The barrier properties of the inorganic layers produced by the lab-coater are comparable with those produced on the semi-production machines. It was unexpected, especially when the great parameter differences between lab-coater and semi-production coating machines is taken into account. The oxygen transmission rates of produced sample were slightly higher, whereas the water vapour transmission rates are nearly the same to the samples produced on the semi-production machines.

7 Literature

[1] Mattox, D. M.: Vacuum coating technology. William Andrew Publishing New York, 2003

[2] Kellö, V.; Tkáč, A.: Fyzikálna chémia. Alfa Bratislava, 1969

[3] Stannett, V.: The transport of gases in synthetic polymeric membranes – an historic perspective. J. Membryne Sci. 3, 1978, p. 97 – 115

[4] Hala, E.; Reiser A.: Fysikalní Chémie 1. Nakladatelství Československé Akadémie Věd Praha, 1971

[5] Barrer, R. M.: Diffusion in and through solids. University Press Cambridge, 1941

[6] Comyn, J.: Polymer Permeability. Chapman and Hall London, 1994

[7] Hanika, M.: Zur permeation durch aluminiumbedampfte Polypropylen- und Polyethylenterephtalatfolien, Dissertation, Fakultät für Maschinenwesen. Lehrstuhl für Feststoff- und Grenzflächenverfahrenstechnik, TU München, 2003

[8] Cohen, M.H.; Turnbull, D.: Molecular transport in liquids and gases. J. Chem. Phys. 31 (5), 1959, S. 4155 – 4165

[9] Niemelä, S.; Leppänen, J.; Sundholm, F.: Structural effects on free volume distribution in glassy polysulfones: molecular modelling of gas permeability. Polymer 37 (18), 1996, S. 1 - 12

[10] Hanika, M; Langowski, H.-C; Peukert W.: Simulation and Verification of Defect-Dominated Permeation Mechanisms in Multiple Structures of Inorganic and Polymeric Barrier Layers. 46th Ann. Techn. Conf. Proc., 2001, p. 592 – 599

[11] Roberts, A.P.; Henry, B.M.; Sutton, A.P.; Grovenor, C.R.M.; Briggs, G.A.D.; Miyamoto, T.; Kano, M.; Tsukahara, Y.; Yanaka, M.: Gas permeation in silicon-oxide/polymer (SiO_x/PET) barrier films: role of the oxide lattice, nano-defects and macro-defects. J. Membr. Sci. 208, 2002, p. 75 – 88

[12] Noller, K.; Vasko, K.: Flexible polymer barrier films for the encapsulation of solar cells, Photovoltaic conference Paris, 2004

[13] Henry, B.M.; Erlat, A. G.; Grovenor, C.R.M.; Deng, C.-S.; Briggs, G.A.D.; Miyamoto, T.; Noguchi, N.; Niijima, T.; Tsukahara Y. Growth and Characterization of Transparent Metal Oxide and Oxynitride Gas Barrier Films on Polymer Substrates. 44th Ann. Techn. Conf. Proc. 2001 p. 448 – 454

[14] Grüniger, A.; Rohr, Ph. R.: Influence of defects in SiO_x thin films on their barrier properties. Thin Solid Films 459 (2004) 308

[15] Roberts, A.P.; Henry, B.M.; Sutton, A.P.; Grovenor, C.R.M.; Briggs, G.A.D.; Miyamoto, T.; Kano, A.; Tsukahara, Y.; Yanaka, M.: Gas permeation in silicon-oxide/polymer (SiO_x/PET) barrier films: role of the oxide lattice, nano-defects and macro-defects. J. Membr. Sci. 208, 2002, p. 75 – 88

[16] Benmalek, MDunlop, H.M.: Inorganic coatings on polymers. Surface and Coatings Technology 76 – 77, 1995, p. 821 – 826

[17] Czeremuszkin, G.; Latreche, M.; Wertheimer, M.R.; Sobrinho da Silva, A.S.: Detection and chracterisation of defects in transparent barrier coatings. Plasmas Polym. 6, 2001, p. 107 – 111

[18] Felts, J.T.: Thickness Effects on Thin Film Gas Barriers: Silicon based coatings. 34th Ann. Techn. Conf. Proc., 1991, p. 99 – 104

[19] Phillips, R.W.; Markantes, T.; LeGallee, C.: Evaporated Dielectric Colorless Films on PET and oPP Exhibiting High Barriers Toward Moisture and Oxygen: 36th Ann. Tech. Conf. Proc.,1993, p. 293 – 301

[20] Hanika, M.; Langowski; H.-C; Moosheimer, U.: Layer defects and the synergic effect between inorganic and organic barrier layers. 45th Ann. Tech. Conf. Proc., 2002, p. 519 – 524

[21] Hanika, M.: Zur permeation durch aluminiumbedampfte Polypropylen- und Polyethylenterephtalatfolien, Dissertation. Fakultät für Maschinenwesen, Lehrstuhl für Feststoff- und Grenzflächenverfahrenstechnik, TU München, 2003

[22] Langowski, H.-C: Profiforum Neue Oberflöchen für Kunstoffe Regensburg, 2003

[23] Langowski, H.-C.: Flexible Materialien mit ultrahohen Barriereeigenschaften. Vakuum in Forschung und Praxis 14, 2002, p. 297 – 302,

[24] W. Lohwasser: Large Scale Electron Beam Web Coating Not Only for Packaging. 43rd Annual Technical Conference Proceedings, 2000, p. 362 – 367

[25] Kukla, R.; Ludwig, R.; Meinel, J.: Overview on modern vacuum web coating technology. Surf. Coating. Tech. 86 – 87, 1996, p. 753 – 761

[26] Frey, H.; Kienel, G.: Dünnschichttechnologie. VDI Verlag GmbH Düsseldorf, 1987

[27] Leterrier, Y.: Durability of nanosized oxygen-barrier coatings on polymers. Progress in Materials Science 48, 2003, p. 1 – 55

[28] Hill, R. J.: Physical vapour deposition. Airco Inc. Berkeley, 1976

[29] Reichelt, K.: Nucleation and growth of thin films. Vacuum 38, 1988, p. 1083 – 1099

[30] Hartwig, E. K.: High-vacuum roll coating. Leybold Heraeus Hanau, 1982

[31] Benmalek, M.; Dunlop, H.M.: Inorganic coatings on polymers. Surface and Coatings Technology 76 – 77, 1995, p. 821 – 8261

[32] Deak, G.I.; Jackson, S.C.: Mylar Polyester Films with Inorganic Glass Coatings. 36th Annual Technical Conference Proceedings, 1993, p. 318 – 323

[33] Schiller, N.; Morgner, H.; Neumann, N.; Krug, M.; Straach S.: Oxide Coating on Plastic Film. 41st Ann. Tech. Conf. Proc., 1998, p. 370 – 373

[34] Yanaka, M.; Henry, B. M.; Roberts, A. P.; Grovenor, C.R.M.; Briggs, G. A. D.; Sutton, A. P.; Miyamoto, T.; Tsukahara, Y.; Takeda, N.; Chater, R. J.: How cracks in SiO_x-coated polyester films affect gas permeation. Thin solid films 397, 2001, p. 176 – 185

[35] J.T. Felts: Thickness Effects on Thin Film Gas Barriers: Silicon-Based Coatings. 34th Ann. Tech. Conf. Proc. 1991, p. 99 – 104

[36] Philipp, H. R.: Optical properties of non-crystalline Si, SiO, SiO_x and SiO_2. J. Phys. Chem. Solids 32 (1971) 1935

[37] Bulkin, P. V.; Stewart, P. L.; Lacquet, B. M.: Electron cyclotron resonance plasma enhanced chemical vapour deposition and optical properties of SiO_x thin films. J. of Non-Cryst. Solids 226, 1998, p. 58 – 66

[38] Rinnert, H.; Vergant, M.; Marchal, G.: Structure and optical properties of amorphous SiO_x thin films prepared by co-evaporation of Si and SiO. Material Scien. Engin. B 69 – 70, 2000, p. 484 – 488

[39] Schiller, S.; Neumann, M.; Morgner, H.; Schiller, N.: Reactive Aluminum Oxide Coating of Plastic Films-Possibilities and Limitations for High Deposition Rates. 38th Annual Technical Conference, 1995, p. 18 – 26

[40] Schiller, N.; Reschke, J.; Goedicke, K.; Neumann, M.: Deposition of Alumina Layers on Plastic Films Using Conventional Boat Evaporators. 39th Annual Technical Conference, 1996, p. 404 – 412

[41] Henry, B.M.; Erlat, A.G.; Grovenor, C.R.M.; Briggs, G.A.D.; Tsukahara, Y.; Niijima, T.: Microstructural and Gas Barrier Properties of Transparent Aluminium Oxide and Indium Tin Oxide Films. 43rd Annual Technical Conference Proceedings, 2000, p. 373 – 378

[42] Schiller, S.; Neumann, M.; Morgner H.; Schiller, N.: Plasma-Activated High-Rate Deposition of Oxides on Plastic Films. 37th Annual Technical Conference Proceedings, 1994, p. 203 – 210

[43] Palik, E. D.: Handbook of optical constants of solids III. Academic press San Diego, USA, 1998

[44] Wang, J.; Yu, Y.-H.; Lee, S. C.; Chung, Y.-W.: Tribological and optical properties of crystalline and amorphous alumina thin films grown by low-temperature reactive magnetron sputter-deposition. Surf. .Coating. Tech. 146 – 147, 2001, p. 189 – 194

[45] Treece, R.E.; Eisgruber, I.; Hollingsworth, R.; Engel, J.; Bhat, P.: Applying Combinatorial Chemistry Methodology to Optimizing the Growth of Indium Tin Oxide on Polymeric Substrates. 43rd Annual Technical Conference Proceedings, 2000, p. 171 – 176

[46] Gottmann, J.; Husmann, A.; Klotzbücher, T.; Kreutz, E. W.: Optical properties of alumina and zirconia thin films grown by pulsed laser deposition. Surf. .Coating. Tech. 100 – 101, 1998, p. 415 – 419

[47] Chrástová, V.; Borsig, E.: Makromolekulová chémia. Edičné stredisko STU Bratislava, 1996

[48] The History of Polyester http://inventors.about.com/library/inventors/blpolyester.htm

[49] www.dupont.com/corp/overview/history/

[50] Brydson, J. A.: Plastics materials. Iliffe Books Ltd. Oxford, 1991

[51] Mitsubishi Datasheet – Hostaphan® RD and Hostaphan® RD 26HC

[52] Gioti, M.; Laskarakis, A.; Logothetidis, S.: IR–FUV ellipsometry studies on the optical, electronic and vibrational properties of polymeric membranes. Thin Solid Films 455 – 456, 2004, p. 283 – 287

[53] Laskarakis, A.; Gravalidis, C.; Logothetidis, S.: FTIR and Vis–FUV real time spectroscopic ellipsometry studies of polymer surface modifications during ion beam bombardment. Nucl. Instr. Meth. Phys. Res. B 216, 2004, p. 131 – 136

[54] Woollam, J. A.; Bungay, C.; Hilfiker, J.; Tiwald, T.: VUV and IR spectroellipsometric studies of polymer surfaces. Instr. Meth. Phys. Res. B 208 (2003) 35

[55] Fraunhofer IVV– Internal results for the EU- project Hiproloco (ENK5-2000-00325)

[56] Lukeš, : Elipsometrie – Optická metoda studia tenkých vrstev a povrchových látek. Univerzita J. E. Purkyně Brno, 1971

[57] Azzam, R. M. A.; Bashara, N. M.: Ellipsometry and polarized light. Elsevier Amsterdam, 2003

[58] Václavík, P.: Technická optika. České vysoké učení technické Praha, 1996

[59] Logothetidis, S.: Handbook of Thin Film Materials, Volume 2: Characterization and Spectroscopy of Thin Films. Academic Press, 2002

[60] Tauc, J: Absorption edge and internal electric fields in amorphous semiconductors. Mat. Resear. Bulletin 5, 1970, p. 721 – 729

[61] Nosal, W.H.; Thompson, D.W.; Yan, L.; Sarkar, S.; Subramanian A.; Woollam J.A.: Infrared optical properties and AFM of spin-cast chitosan films chemically modified with 1,2 Epoxy-3-phenoxy-propane. Colloids and Surfaces B: Biointerfaces 46, 2005, p. 26 – 31

[62] Akaoglu, B.; Atilgan, I.; Katircioglu, B.: Thickness and optical constant distributions of PECVD a-SiC*x*:H thin films along electrode radial direction. Thin Solid Films 437, 2003, p. 257 – 265

[63] Mistrik, J.; Yamaguchi, T.; Franta, D.; Ohlidal, I.; Hu, G. J.; Dai, N.: Optical properties of rough $LaNiO_3$ thin films studied by spectroscopic ellipsometry and reflectometry. App. Surf. Sci. 244, 2005, p. 431 – 434

[64] Jellison, G .E.; Merkulov, V. I.; Puretzky, A. A.; Geohegan, D. B.; Eres, G.; Lowndes D. H.; Caughman, J. B.: Characterization of thin-film amorphous semiconductors using spectroscopic ellipsometry. Thin Solid Films 377 – 378, 2000, p. 68 – 73

[65] Kavak, H.; Eker, S.; Mamedov, A: Harmonic oscillator model and determination of optical parameters. J. Quant. Spectr. Radiat. Transf. 86, 2004, p. 223 – 229

[66] Freund, J. E.; Walpole, R. E.: Mathematical statistic. Prentice Hall International London, 1980

[67] Sachs, L.: Angewandte Statistik. Springer-Verlag Berlin, 1997

[68] Linczenyi, A.; Štrpka, A.: Inžinierska štatistika, Slovenská vysoká škola technická Bratislava, 1973

[69] Shapiro, S. S.; Wilk, M. B.: An analysis of variance test for normality (complete samples). Biometrika 52, 1965, p. 591 – 611

[70] Pearson, A. V.; Hartley, H. O.: Biometrica Tables for Statisticians Vol 2. Cambridge University Press, England, 1972

[71] Datenblatt von Leybold Optics: „LAB Family“

[72] User guide to the e-beam coater: Leybold A260 E/B1

[73] Mitsubishi: Datasheet Hostaphan® RNK

[74] Report from ESCA Laboratory of the J. Heyrovsky Institute of Physical Chemistry, Academy of Sciences of the Czech Republic (July 5th 2003)

[75] Measured samples were produced on the semi-production e-beam coater at Applied Films GmbH & Co. KG, Alzenau

[76] Measured samples were produced on the pilot e-beam coater at Alcan Packaging Services AG, Neuhausen